EFFICIENCY AND RELIABILITY ENHANCEMENT OF MULTIPHASE SYNCHRONOUS MOTOR DRIVES

A Dissertation

by

AMIR NEGAHDARI

Submitted to the Office of Graduate and Professional Studies of
Texas A&M University
in partial fulfillment of the requirements for the degree of

DOCTOR OF PHILOSOPHY

Chair of Committee,	Hamid A. Toliyat
Committee Members,	Chanan Singh
	Shankar P. Bhattacharyya
	Shima Hajimirza
Head of Department,	Miroslav Begovic

December 2018

Major Subject: Electrical Engineering

ABSTRACT

Multiphase electric machines are attractive in comparison with three-phase ones due to advantages such as fault-tolerant nature, smaller rating per phase and lower torque ripple. More specifically, the machines with multiple three-phase windings are particularly convenient, because they are suitable for standard off-the-shelf three-phase dc/ac converter modules. For instance, they are becoming a serious option for applications such as electric vehicles and wind turbines. On the other hand, in these applications, operation at low power is often required for long time intervals; hence, improving the efficiency under such conditions is highly desired and could save a significant amount of energy in the long term. This dissertation proposes a method to enhance the efficiency of electric drives based on multiple three-phase windings at light load. The number of active legs is selected depending on the required torque at each instant. To ensure that the overall efficiency is effectively optimized, not only the converter losses, but also the stator copper losses, are taken into account. Experimental results verify the theoretical outcomes.

Surface-mounted permanent-magnet synchronous motors (SPMSMs) require a position measurement to ensure a high-performance control. To avoid the cost and maintenance associated to position sensors, sensorless methods are often preferred. The approaches based on high-frequency signal injection are currently a well-established solution to obtain an accurate position estimation in SPMSMs. These techniques can be roughly divided into two groups: those based on sinusoidal or on square-wave high-

frequency signals. The main drawback of the former is the limitation on the response speed, due to the presence of several low-pass filters (LPFs). On the other hand, the latter methods are sensitive to deadtime effects, and high-frequency closed-loop current control is required to overcome it. This dissertation proposes to improve the sensorless strategies based on sinusoidal high-frequency injection by simplifying the scheme employed to extract the information about the position error. Namely, two LPFs and several multiplications are removed. Such simplification does not only reduce the computational complexity, but also permits to obtain a faster response to the changes in the angle/speed, and hence, a faster closed-loop control. Experimental results based on a SPMSM prove the enhanced functionality of the proposed method with respect to the previous ones based on high-frequency sinusoidal signal injection.

DEDICATION

To my parents

ACKNOWLEDGEMENTS

I consider myself lucky to get the opportunity of working with my supervisor Prof. Hamid A. Toliyat. I thank him for his continuous support and engagement, his valuable time, his commitment to excellence in research, his patience and his sense of humor in the course of past few years.

I am grateful to my committee members Prof. Chanan Singh, Prof. Shankar Bhattacharyya and Dr. Shima Hajimirza. I learnt a lot from attending their courses and advising during the course of study at Texas A&M University.

I would also like to thank ECE department staff – Mrs. Tammy Carda, Melissa Sheldon, Crystal Rodriguez and Katharine Bryan who have always been very pleasant and helpful.

I express my deep gratitude to my colleagues at EMPE lab and EPPE group at ECEN department for their help in conducting experiments, building test setups and technical discussions. I also thank all my other labmates, Drs. Khaled Al Jaafari, Abdulkadir Bostanci, Vivek Sundaram, Yateendra Deshpande, Siavash Pakdelian, Jae-Bum Park, Matthew Johnson, Hussain Hussain, Bahar Anvari, Matthew Gardner, Morteza Moosavi, Ajay Kumar Morya, Farid Naghavi and Niloofar Torabi who help me feeling comfortable in the lab.

I am thankful of being lucky to cooperate with Dr. Alejandro Gomez Yepes of Applied Power Electronics Research Group, University of Vigo, Spain on this project. I

really appreciate his patience and continuous advices during almost two years that was spent on this research project.

Last but not the least, I would like to thank my parents for their love, patience, selfless support and encouragement over the years. This work would have not been possible without their support.

CONTRIBUTORS AND FUNDING SOURCES

Contributors

This work was supervised by a thesis committee consisting of Professor Hamid A. Toliyat [advisor] and Professors Chanan Singh and Shankar Bhattacharyya of the Department of Electrical and Computer Engineering and Dr. Shima Hajimirza of the Department of Mechanical Engineering.

All work for the thesis was completed by the student, in collaboration with Dr. Alejandro Gomez Yepes.

Funding Sources

This work was made possible by the available facilities at EMPE lab.

I would like to thank Hyosung Corporation for donating the permanent magnet synchronous motor and Texas Instruments for providing the microcontroller kits.

NOMENCLATURE

P_{cond}	Conduction loss
tr	Transistor
d	Diode
V_{ce0}	Switch collector emitter voltage
V_{d0}	Diode forward voltage drop
r_{ce}	Collector emitter on state resistance
r_{d}	Diode on state resistance
m	Modulation index
$\cos\phi$	Power factor
I	rms phase current
P_{sw}	Switching loss
f_{sw}	Switching frequency
E_{on}	Switch turn on loss
E_{off}	Switch turn off loss
E_{rr}	Diode reverse recovery loss
T_j	Junction temperature
T_{ref}	Reference temperature
T_c	Temperature coefficient
k_i	Current ratio order
k_v	Voltage ratio order

I_{in}	Device input current
I_{ref}	Device reference current
V_{out}	Device voltage
V_{ref}	Device reference voltage
r_s	Stator winding series resistance
v_{dh}	d-axis high frequency voltage
v_{qh}	q-axis high frequency voltage
r_{dh}	d-axis high frequency resistance
r_{qh}	q-axis high frequency resistance
L_{dh}	d-axis high frequency inductance
L_{qh}	q-axis high frequency inductance
i_{dh}	d-axis high frequency current
i_{qh}	q-axis high frequency current
$\tilde{\theta}$	Rotor angle estimation error
θ_r	Actual rotor angle
$\hat{\theta}_r$	Estimated rotor angle
Z_{dh}	d-axis high frequency impedance
Z_{qh}	q-axis high frequency impedance
Z_{avg}	*d*- and *q*-axis high-frequency impedance average
Z_{diff}	*d*- and *q*-axis high-frequency impedance difference
V_{inj}	Amplitude of the high-frequency injected voltage
v_{dh}	Injected high-frequency voltage in the estimated *d* axis

v_{qh}	Injected high-frequency voltage in the estimated q axis
r_{diff}	Differences between the d- and q-axis components of the high-frequency resistance
L_{diff}	Differences between the d- and q-axis components of the high-frequency inductance
LPF	Low pass filter
BPF	Band pass filter
$i_{\tilde{\theta}_r}$	Input to the rotor position estimator

TABLE OF CONTENTS

Page

ABSTRACT……...ii

DEDICATION……...iv

ACKNOWLEDGEMENTS……..……..v

CONTRIBUTORS AND FUNDING SOURCES……vii

NOMENCLATURE……viii

TABLE OF CONTENTS…….....xi

LIST OF FIGURES……..……..xiii

LIST OF TABLES……...…….…….xvii

1. INTRODUCTION……...……...1

1.1. Multiphase vs three-phase machines ……1
1.2. Multiphase Machines Applications.....…….2
1.2.1. Electric Vehicles and Railway Traction……...2
1.2.2. Wind Power Generation Systems…….3
1.2.3. All Electric Ships……..3
1.2.4. More Electric Aircraft……...4
1.3. Multiphase Machines Based on Multiple Three-phase Winding Sets ……..4
1.4. Loss Components in Multiphase Systems …….……...5
1.4.1. Converter Losses……..5
1.4.1.1. Modular Multilevel Converters…….6
1.4.1.2. Discontinuous Pulse Width Modulation……6
1.4.1.3. Hybrid Switch based Soft Switching Inverter……...8
1.4.1.4. Direct Self Control (DSC) With Minimum Switching Operations Instead of Field Oriented Control (FOC)……..9
1.4.1.5. Wide Band Gap Power Devices……9
1.4.2. Copper Losses…….....……...11
1.4.3. Miscellaneous Losses……12
1.5. Position Sensorless Drive Schemes for Multiphase Machines……...……...12
1.5.1. Back Electromotive Force (back-EMF) Estimation…...……13
1.5.2. Rotor Saliency……...……..14

1.5.3. High-Frequency Injection……...…….16
1.5.4. Combinational Schemes……...……...…17
1.6. Research Objectives……...……19
1.7. Thesis Outline……...……19

2. EFFICIENCY ENHANCEMENT OF MULTIPHASE ELECTRIC DRIVES AT LIGHT-LOAD OPERATION CONSIDERING BOTH CONVERTER AND STATOR COPPER LOSSES…….....…….……21

2.1. Background……...……...23
2.2. Converter Efficiency Enhancement..……...……....25
2.3. Proposed Strategy for Enhancement of Overall Efficiency……...…..……....30
2.4. Experimental Setup..……...…….41
2.5. Drive Schemes……...……..46

3. IMPROVED SENSORLESS DRIVE FOR SYNCHRONOUS MOTORS BASED ON HIGH-FREQUENCY SINUSOIDAL SIGNAL INJECTION WITH SIMPLIFIED EXTRACTION OF POSITION-ERROR INFORMATION…….63

3.1. High-frequency Impedance Characteristic of the Surface-Mount Permanent Magnet Synchronous Motor (SPMSM)……...…….....…63
3.2. Proposed Improved Sensorless Scheme…….…...……...……..72
3.3. Experimental Results……...……....74

4. SUMMARY AND FUTURE WORK……...……..…….83

REFERENCES…….89

LIST OF FIGURES

Page

Fig. 1.1 Multiphase machine application in electric vehicle, [74]……..……...2

Fig. 1.2 Multiphase machine application in wind farms, [75]...…….3

Fig. 1.3 Multiphase machine application in all electric ships, [76]…….3

Fig. 1.4 Multiphase machine application in more electric aircrafts, [77]……4

Fig. 1.5 Generalized schematic of an electric drive based on multiple three phase windings with isolated neutrals…….…….....5

Fig. 1.6 Modular multilevel converters used for converter loss reduction [27]……...6

Fig. 1.7 Efficiency comparison of SPWM, SVPWM and DPWM vs a) modulation index, b) switching frequency, and c) gate resistance [24].……...…7

Fig. 1.8 Hybrid switch based soft switching inverter [29]……...…8

Fig. 1.9 DSC schematic [28]…….……...…9

Fig. 1.10 Efficiency comparison of different semiconductor switches [30]……..….10

Fig. 2.1 Generalized schematic of an electric drive based on multiple three-phase windings with isolated neutrals……..23

Fig. 2.2 Efficiency comparison, considering only the converter losses, of utilization of different number of converter legs and the SECE with operation at (a) full range of load, and (b) light load (zoomed)……...……...28

Fig. 2.3 Efficiency comparison, considering only the stator copper losses, of utilization of different number of converter legs with operation at (a) full range of load, and (b) light load (zoomed)…….……31

Fig. 2.4 Efficiency comparison, considering both the converter and copper losses, of utilization of different number of converter legs and the SEOE with operation at (a) full range of load, and (b) light load (zoomed)…..……33

Fig. 2.5 Comparison of the SECE and SEOE in terms of overall efficiency and threshold output-power values…...…….36

Fig. 2.6 Comparison of the SEOE for machines with different stator resistances…….39

Fig. 2.7 Analytical comparison of SEOE for converters with different switching frequencies…….40

Fig. 2.8 Experimental setup……41

Fig 2.9 FEA model of the synchronous motor stator and rotor showing double layer short pitched windings, adapted……..……...42

Fig. 2.10 Original motor winding configuration, a) actual external taps, b) schematic of the taps along the winding, and c) coils connection……..…...….43

Fig. 2.11 Three to six-phase reconfiguration. a) distributed layout (green arrows refer to old connections and red arrows refer to new connections.) and b) Spatial representation of the phase vectors…….44

Fig. 2.12 Phase back EMFs for a) 1st three-phase and b) 2nd three-phase set…….45

Fig. 2.13 Equivalent circuit of the synchronous motors in *d* and *q* axes……47

Fig. 2.14 Overall FOC block diagram of the system……..48

Fig. 2.15 Speed control loop of the FOC……52

Fig. 2.16 Harmonic rejection scheme block diagram…….53

Fig. 2.17 Block diagram of active resistance scheme…….54

Fig. 2.18 Current step response, a) broad range and b) zoomed version……56

Fig. 2.19 Speed step response (shown in yellow)……...58

Fig. 2.20 Efficiency measurement of the actual prototype considering (a) only converter losses, (b) only copper losses, and (c) overall losses……..58

Fig. 2.21 Experimental comparison of the overall efficiency with the SEOE at (a) different stator resistances, and (b) different switching frequencies……...60

Fig. 2.22 Phase currents, speed and torque waveforms during the mode transition from (a) 6 to 3 phases, and from (b) 3 to 6 phases. The scale of the speed and torque is 400 rpm/div and 2 Nm/div, respectively……61

Fig. 3.1 Measurement and the actual reference frame for high frequency impedance measurement……67

Fig. 3.2 High-frequency impedance characteristic of the SPMSM versus mechanical rotor angle at a) different magnitude of the injected voltages of 500 Hz frequency, b) different frequency of the injected voltages of 40 V magnitude…….....69

Fig. 3.3 High-frequency impedance characteristic of the SPMSM versus mechanical rotor angle at 20 V, 500 Hz high frequency sinusoidal voltage injection in the *x* axis……...…70

Fig. 3.4 Calculation of the error signal……...72

Fig. 3.5 Digital implementation of the BPF (shown in the red box) in conjunction With the error signal calculation……...……72

Fig. 3.6 Simplified method of $i_{\tilde{\theta}_r}$calculation……..73

Fig. 3.7 Block diagram for estimating the rotor angle and the speed……..74

Fig. 3.8 Experimental prototype…….....75

Fig. 3.9 Winding connections of the original 24-phase SPMSM……....76

Fig. 3.10 Six-phase BEMF waveforms of the motor shown in one full period……...77

Fig. 3.11 Estimated and measured electrical rotor angle versus time at a) 75 rpm, and b) 100 rpm. The scale is 4.2 rad/div……..……79

Fig. 3.12 Speed transient behavior when dropping the speed from 75 to 0 rpm ……..80

Fig. 3.13 $i_{\tilde{\theta}_r}$in steady-state for conventional and proposed scheme. The scale is 0.25 A/div...…….....80

Fig. 3.14 Harmonic spectrum of $\sin\tilde{\theta}_r$, normalized with respect to the fundamental, for a) conventional scheme and b) proposed scheme…… ……..81

Fig. 4.1 Back-EMF and current vectors in first and second planes of the six phase SMPMSM……85

LIST OF TABLES

Page

Table 2.1 Characteristics of the 24-phase PMSM…….25

Table 2.2 Characteristics of the semiconductor devices……....26

Table 2.3 Synchronous motor parameters……..42

Table 3.1 Experimental setup characteristics…….77

1. INTRODUCTION

1.1. Multiphase vs three-phase machines

Multiphase electric machines have gained considerable attention recently because of:

1- Fault tolerant capability:

This is especially important in safety critical applications such as general aerospace or military naval applications, more electric aircraft actuators, linear permanent magnet machines for oil pumping applications and permanent magnet traction motor used in ultrahigh-speed elevators [1, 2].

2- Less torque ripple:

Multiphase motors are usually less susceptible to time harmonics therefore producing less pulsating torques both at low and high frequencies [3].

3- Power and current splitting among higher number of phases:

This feature allows to derive higher currents and power compared to the conventional three phase motors making it suitable for higher power applications.

4- Increasing the average torque by harmonic injection:

Extra harmonic currents can be injected in the secondary planes to help increasing the torque.

5- Use of additional degrees of freedom for parameter identification:

Depending on the number of phases, several sub planes might exist in the control frame of the machine which can be used for identification purposes.

6- Multimotor multiphase variable speed drives with single inverter supply:

There are many applications in which several motors are required to be driven simultaneously. A single multiphase inverter suffices to run the entire system with only one control scheme.

7. Use of additional degrees of freedom for sensorless drives:

Higher number of phases leads to more flexibility in implementing various control schemes as combination of several subspaces can be employed.

1.2. Multiphase Machines Applications

Multiphase machines are being increasingly used in different applications in which the above mentioned advantages of machines can be employed to better serve the application specific requirements.

1.2.1. Electric Vehicles and Railway Traction

Several papers [4 - 11]**,** emphasize the incorporation of multiphase electric motors in electric and hybrid electric vehicles, Fig. 1.1. Also, some industrial products have been released based on multiphase machines. As stated in [12], PML has built its electric vehicle based on a 24 phase, 1800 rpm, high efficiency brushless permanent magnet motor.

Fig. 1.1: Multiphase machine application in electric vehicles, reprinted from [74].

1.2.2. Wind Power Generation Systems

References [13 - 19] mention 6-, 9-, 12- and 18-phase motors specifically used in wind turbine generators. Higher number of phases can be specially helpful in wind turbines as they are able to handle higher powers, Fig. 1.2.

Fig. 1.2: Multiphase machine application in wind farms, reprinted from [75].

1.2.3. All Electric Ships

Multiphase motors can be used in electric ship propulsion systems as part of the electric drive system [20], Fig. 1.3.

Fig. 1.3: Multiphase machine application in all electric ships, reprinted from [76].

1.2.4. More Electric Aircraft

Higher torque density characteristics of the multiphase motors makes them good candidates for more electric aircraft application in which lightness and compactness is of high importance [21], Fig. 1.4.

Fig. 1.4: Multiphase machine application in more electric aircrafts, reprinted from [77].

1.3. Multiphase Machines Based on Multiple Three-phase Winding Sets

Multiphase machines based on multiple three-phase windings with isolated neutrals are specially of interest due to their suitability for available standard off-the-shelf three-phase dc/ac converters in the market [22, 23]. Furthermore, the isolation of the neutral points restricts circulating currents that would otherwise increase the losses [24]. For those multiple three-phase systems with non-isolated neutrals, the neutral points of three-phase sets can be connected to the midpoint of the dc link which also reduces the circulating current.

The generalized schematic for a multiphase drive based on multiple three-phase stator windings with isolated neutrals is shown in Fig. 1.5, where γ equals 2 or 1 for

symmetrical or asymmetrical winding arrangements, respectively [25], and *n* stands for the total number of phases.

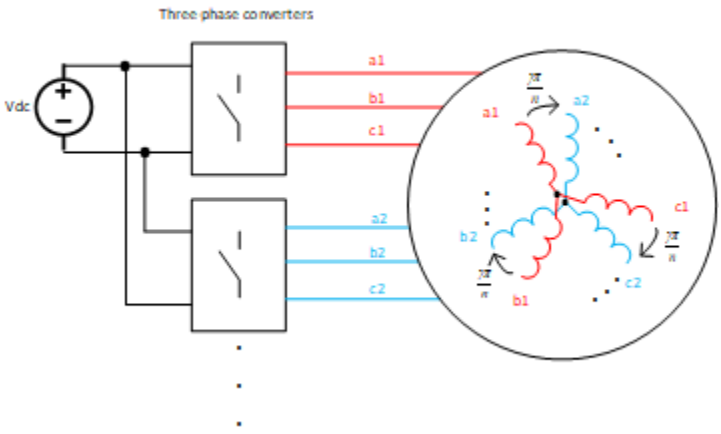

Fig. 1.5: Generalized schematic of an electric drive based on multiple three phase windings with isolated neutrals.

The converter consists of *n*/3 three-phase modules connected to a single dc bus. Each of these modules supplies a three-phase winding set of the machine. The dc source shown in Fig. 1.5 may represent in a simplified manner, e.g., the batteries in an electric vehicle or the dc side of a three-phase grid-connected converter in a wind turbine system.

1.4. Loss Components in Multiphase Systems

1.4.1. Converter Losses

Converter losses are part of the major loss components associated with electric drives [26 - 28]. Efficiency of converters, even though already relatively high, has been always a challenge to be improved further by establishing various approaches.

1.4.1.1. Modular Multilevel Converters

Modular multilevel converters can be adopted as shown in Fig. 1.6 [27] instead of conventional two-level ones, at the expense of a more complicated control (for adequate balancing) [26]. They possess cascaded submodules with bidirectional H-bridge converters. The battery cells will be of lower voltage and therefore low voltage MOSFETS can reduce the switching and conduction losses.

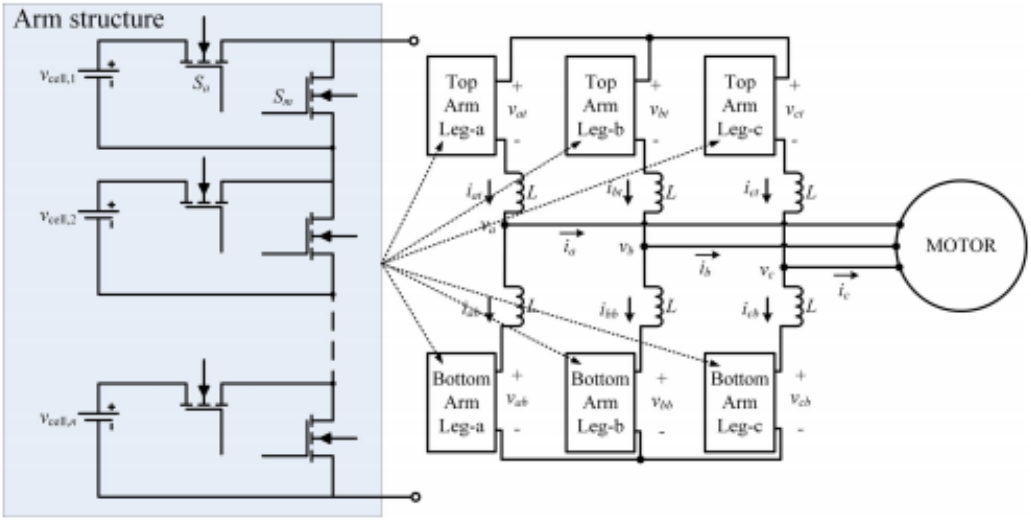

Fig. 1.6: Modular multilevel converters used for converter loss reduction, reprinted from [27].

1.4.1.2. Discontinuous Pulse Width Modulation

Another alternative to improve the converter losses would be discontinuous pulse width modulation in which the lesser losses are seen compared to the space vector and sinusoidal pulse width modulation as shown in Fig. 1.7, [26].

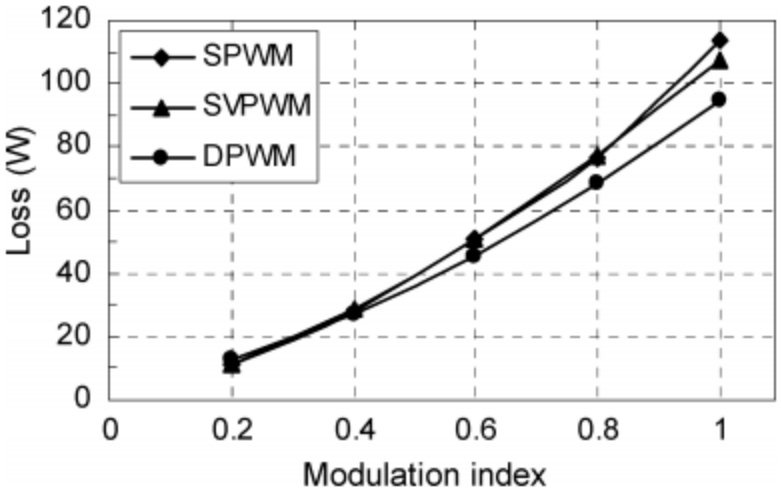

(a)

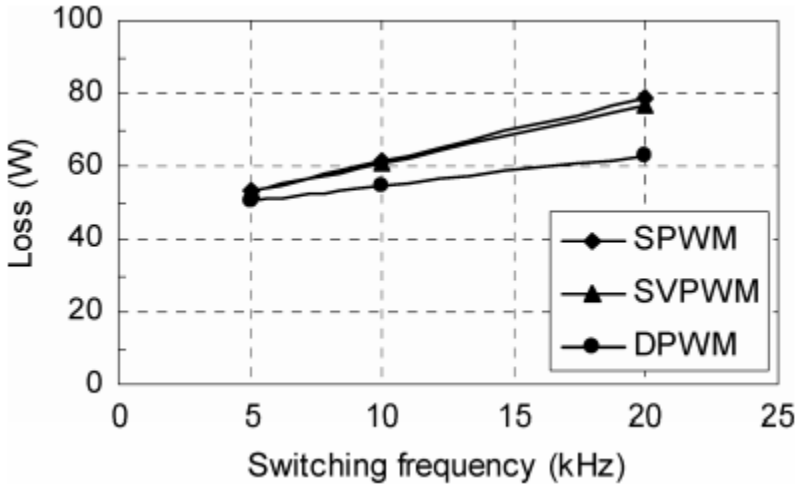

(b)

Fig. 1.7: Efficiency comparison of SPWM, SVPWM and DPWM vs a) modulation index, b) switching frequency, and c) gate resistance, reprinted from [24].

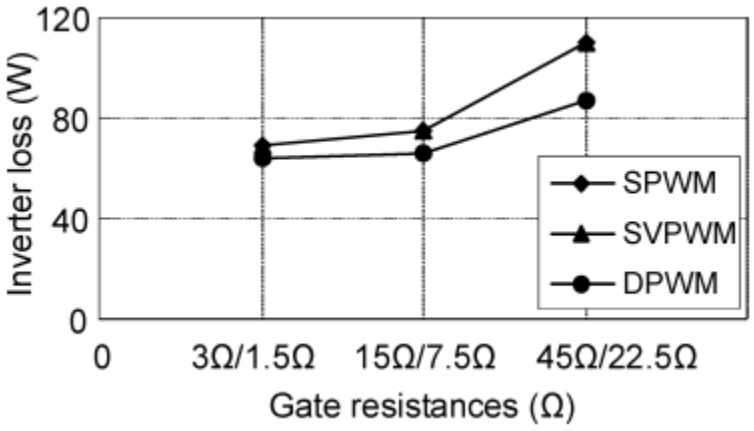

(c)

Fig. 1.7: Continued.

1.4.1.3. Hybrid Switch based Soft Switching Inverter

The current is shared among the IGBT and MOSFET, as shown in Fig. 1.8, at light load in this topology therefore reducing the losses. Moreover, intentional delays are used to avoid overcurrents on the MOSFET [29].

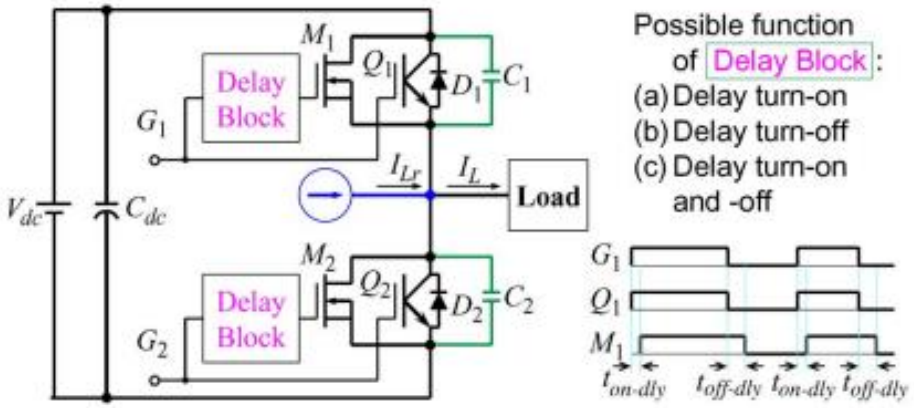

Fig. 1.8: Hybrid switch based soft switching inverter, reprinted from [29].

1.4.1.4. Direct Self Control (DSC) With Minimum Switching Operations Instead of Field Oriented Control (FOC)

By default, FOC is used in most of the motor drive systems. DSC as an intelligent alternative can reduce losses. It includes flux and torque regulators with hysteresis controllers. It performs the main commutation every π/3 radians and the secondary commutation like a simple PWM as shown in Fig. 1.9, [28].

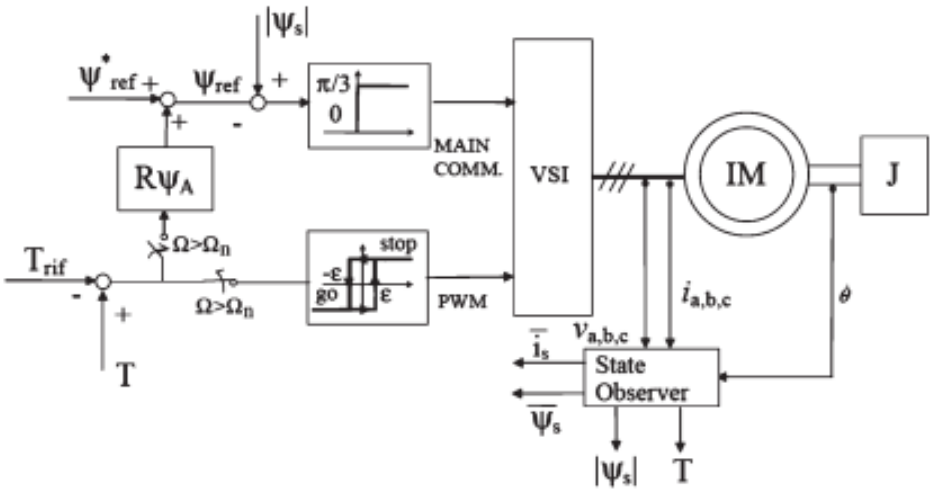

Fig. 1.9: DSC schematic, reprinted from [28].

1.4.1.5. Wide Band Gap Power Devices

Wide band gap power devices have recently gained a lot of attention due to their higher efficiency, higher achievable switching frequency, maximum permissible junction temperature and power density as shown in Fig. 1.10, [30].

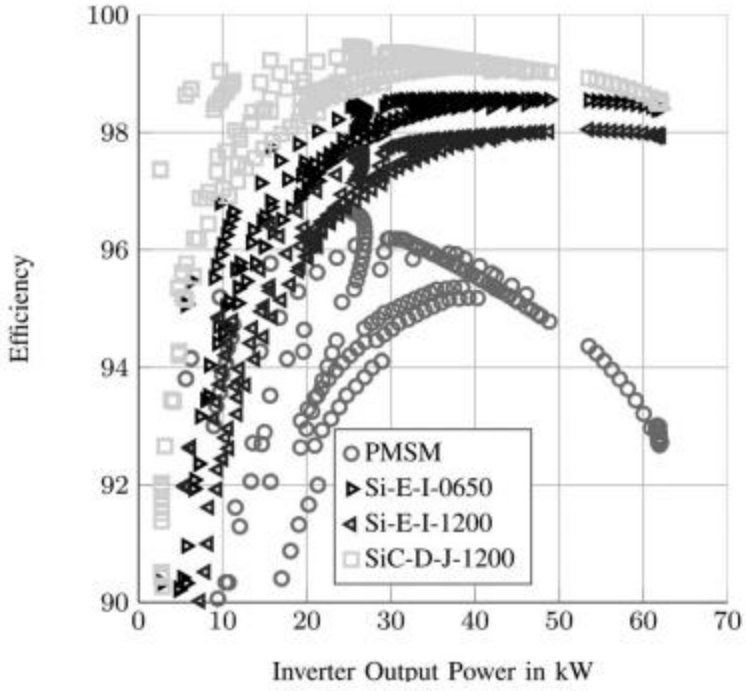

Fig. 1.10: Efficiency comparison of different semiconductor switches, reprinted from [30].

The losses in ac/dc converters are divided into the following two major parts [31 - 33].

1) Conduction Losses:

   The on-state resistances of semiconductor switches and of anti-parallel diodes cause ohmic losses while they conduct. These losses are given by the following equations [32 - 33]:

$$P_{cond,tr} = \frac{1}{2}\left(V_{ce0}\frac{I}{\pi} + r_{ce}\frac{I^2}{4}\right) + m\cos\phi\left(V_{ce0}\frac{I}{8} + \frac{r_{ce}I^2}{3\pi}\right) \quad (1)$$

$$P_{cond,d} = \frac{1}{2}\left(V_{d0}\frac{I}{\pi} + r_{d}\frac{I^2}{4}\right) - m\cos\phi\left(V_{d0}\frac{I}{8} + \frac{r_{d}I^2}{3\pi}\right) \quad (2)$$

where P_{cond}, tr, d, V_{ce0}, V_{d0}, r_{ce}, r_{d}, m, $\cos\phi$ and I denote conduction losses, transistor, diode, switch collector-emitter voltage, diode forward voltage drop, collector-emitter on-

state resistance, diode on-state resistance, modulation index, power factor and rms phase current, respectively.

2) Switching Losses:

The losses associated with non-ideal switching exist on both the diodes and the switches, and they are given by [32 - 33]:

$$P_{sw,tr} = f_{sw}(E_{on} + E_{off})\left(\frac{I_{in}}{I_{ref}}\right)^{k_{i,tr}}\left(\frac{V_{out}}{V_{ref}}\right)^{k_{v,tr}}\left(1 + T_{c,tr}(T_j - T_{ref}\right) \tag{3}$$

$$P_{sw,d} = f_{sw}(E_{rr})\left(\frac{I_{in}}{I_{ref}}\right)^{k_{i,d}}\left(\frac{V_{out}}{V_{ref}}\right)^{k_{v,d}}\left(1 + T_{c,d}(T_j - T_{ref}\right) \tag{4}$$

where P_{sw}, f_{sw}, E_{on}, E_{off}, E_{rr}, T_j, T_{ref}, T_c, k_i, k_v, I_{in}, I_{ref}, V_{out} and V_{ref} represent switching losses, switching frequency, switch turn-on losses, switch turn-off losses, diode reverse-recovery losses, junction temperature, reference temperature, temperature coefficient, current ratio order, voltage ratio order, device input current, device reference current, device voltage and device reference voltage, respectively.

1.4.2. Copper Losses

Copper losses are another dominant losses in motor drive systems. The stator winding series resistances even though small can create ohmic losses due to the high currents flowing through the windings. In multiphase systems, the copper losses are generally greater than three-phase systems. The copper loss is described by (5):

$$P_{L,copper} = nr_s I^2 \tag{5}$$

where $P_{L,\,copper}$, n, r_s and I stand for stator copper losses, number of stator phases, stator winding series resistance and phase currents, respectively.

1.4.3. Miscellaneous Losses

There always exist some other losses especially on the electric machine side which are quiet smaller than the copper and converter losses but still might be considered for better accuracy. These losses are often hard to measure in experiments but can be estimated by some proposed methods. Core, stray and windage losses can be mentioned as instances of these losses. They often do not change substantially when changing the number of stator phases as long as the torque and speed of the motor is fixed which means constant flux distribution in the air gap is maintained.

1.5. Position Sensorless Drive Schemes for Multiphase Machines

Permanent-magnet synchronous motors are currently used as a major component of electric machine industry due to their higher efficiency, lower size and higher torque density [34 - 35]. Closed-loop control is crucially required in driving permanent-magnet motors, as otherwise they cannot be operated at the desired conditions [36 - 37]. Multiple data have to be provided in any closed-loop motor drive system as feedbacks so that proper control is implemented.

Position information is one of these required data, which is usually generated by encoders as position sensors. Encoders are relatively costly devices that require maintenance, therefore reducing the reliability of the overall drive [38]. Consequently, significant research has been performed to extract instead the rotor angle information from signatures such as modulating signals and stator currents [39 - 54].

The position sensorless schemes can be generally divided into the flowing categories:

1.5.1. Back Electromotive Force (back-EMF) Estimation

Different types of position sensorless schemes were proposed for three-phase synchronous motor drives. Some methods are based on back-electromotive force (EMF) estimation [39 - 43], which suffer inaccuracy at low speeds due to low back-EMF magnitude.

As a literature work, [39] proposes a position sensorless method for high speed permanent magnet machines. The motor's equations are modelled in discrete time to estimate the back-EMF. An observer based back-EMF estimation at high speed based on digital implementation of the motor model was established. Voltage delays due to cross coupling effects is compensated and the sensorless performance was verified in an 8 pole surface mount permanent magnet synchronous motor.

A position sensorless method based on the sliding mode observer is proposed in [40]. Phase locked loop (PLL) and synchronous frequency filters are used to remove the harmonic contents of the back-EMF. The proposed method is tested in the drive of an interior permanent magnet synchronous motor to verify the functionality of the scheme and is also compared to not using the sensorless in terms of loading condition and efficiency.

An sliding mode observer with a quadrature phase locked loop is proposed in [41] to perform a sensorless drive on an interior permanent magnet synchronous motor. Position estimation errors due to inverter non-linearities and flux spatial harmonics are analyzed and schemes based on adaptive compensation are proposed to reduce the errors. An experimental prototype was built to implement the sensorless algorithm.

A sensorless drive of a brushless direct current motor (BLDC) based on the virtual third harmonic phase back-EMF to improve the performance is proposed in [42]. The commutation error is analyzed and a sensorless method based on high precision commutation detection is proposed. The method incorporates both phase locked loop and synchronous frequency filters. The performance of the sensorless method was verified both under load and no load conditions.

A sensorless method for open winding permanent magnet synchronous machine with circulating current suppression is proposed in [43]. The common dc bus and phase shift based zero sequence steerable space vector pulse width modulation model of the machine is developed. The sensorless method based on equivalent zero sequence circuit model and circulating current suppression is proposed. The proposed scheme was verified on an outer rotor PMSM to verify the functionality.

1.5.2. Rotor Saliency

Another approach relies on the fact that the salient geometry of the rotor causes the *d* and *q* axes inductances of the machine in rotating reference frame to carry information of the rotor angle [44 - 49]; however, this method is only applicable to the motors with salient rotor structure.

As a literature work, [45] proposes a saliency based sensorless control for interior permanent magnet motors for electric vehicle applications. First, a design approach with sensorless purposes is described. Design parameters and restrictions are defined to satisfy the maximum torque and efficiency conditions. The sensorless control was

implemented on an actual prototype and the above defined parameters were measured to ensure the applicability of the proposed scheme.

An improved saliency-based position sensorless drive of an interior permanent magnet synchronous machine with a single dc-link current sensor is proposed in [46]. The conventional current reconstruction error was analyzed and a new method is proposed to minimize it.

A sensorless salient pole brushless direct current motor direct torque control drive system is proposed in [47]. A rotor position estimator with back-EMF self adaptation was developed to measure the stator phase currents and rotor position. Simulations and experiments are performed to verify the functionality of the rotor position estimator at steady state and dynamics conditions.

Reference [48] proposes a novel secondary saliency tracking algorithm to implement the sensorless control for machines such as concentrated winding surface mount permanent magnet synchronous motor. The secondary saliency tracking method with band pass filter design and initial position estimation is explained. An experimental setup is used to verify the functionality of the proposed scheme.

Reference [49] analyzes the effects of the geometry design parameters of an interior permanent magnet synchronous motor with concentrated winding on the saliency-based sensorless drive. Two schemes based on the contour of inductance and the inductance harmonics are proposed. Design models based on the chamfer, closed slot and the notch is then developed. The final achieved model is tested on an experimental setup.

1.5.3. High-Frequency Injection

The schemes based on high-frequency injection estimate the position by using the difference in high-frequency impedance between the *d* and *q* axes [50 - 54].

A novel high frequency signal injection method of sensorless drive for doubly fed induction machines is proposed in [50]. Rotor position is extracted from the high frequency currents injected through the rotor winding considering the high frequency disturbance from the stator side and using a phase locked loop. Steady state, transient and tracking responses are captured in an experimental prototype.

An asymmetric space vector modulation scheme for sensorless drive application of a permanent magnet synchronous motor based on high frequency square wave injection in low switching frequency applications is proposed in [51]. Errors caused by low switching frequency harmonics and inverter deadtime effects are analyzed. The currents and position estimation performance is verified in an interior permanent magnet synchronous motor.

A position estimation method based on derivative calculations of current and zero voltage vector injection is proposed in [52] to improve the acoustic noise and torque ripples caused by the high frequency square wave voltage injection. The applicability of the proposed scheme has been tested in an interior permanent

A low-frequency pulse voltage injection scheme is proposed in [53] to remove the audible noise pollution. An enhanced vector tracking observer for rotor position estimation is developed and its stability was analyzed. An interior permanent magnet synchronous motor was used to implemented the proposed scheme.

Reference [54] evaluates the square-wave injection voltage at different frequencies for the design of an interior permanent-magnet machine sensorless drive. Reduced flux density, increased d-axis flux saturation and secondary saliency harmonics at high frequency are also considered. Different inductances, saliency current signal and saliency secondary harmonics are measured against the injected frequency in an interior permanent magnet synchronous motor.

1.5.4. Combinational Schemes

Some methods also combine the aforementioned strategies to bring together the advantages of each. For example, a common option is to alternatively employ back-EMF estimation at high speeds and high-frequency signal injection at low speeds [55 - 56].

A sensorless control scheme for synchronous reluctance motor drives based on the direct-flux vector control method is proposed in [55]. A sensorless active flux observer based on the high frequency signal injection and demodulation, absence of cross saturation error, effect of high frequency injection on the observed flux, tuning of the tracking loop and criteria for minimum excitation limit selection is also proposed. The responses of the speed closed loop control, transition between the two sensorless models, flux weakening and cross saturation error are measured in an experimental setup.

A full speed sensorless drive for permanent magnet synchronous motors is proposed in [56]. The drive uses high frequency square wave voltage injection for zero and low speeds and back-EMF estimation for medium speeds. The magnet polarity is

used to detect the rotor position at standstill. A transition algorithm is designed to switch between the saliency based and back-EMF based approaches.

Among the methods using high frequency signal injection to create magnetic saliency, sinusoidal [57] and square-wave voltages [58 - 59] have been injected.

A sensorless scheme for surface mount permanent magnet synchronous motors is proposed in [57]. It creates a high frequency magnetic saliency by injecting high frequency voltages and measuring the high frequency currents. The scheme works best if the difference of the high frequency impedances along the *d* and *q* axes are significant.

The adverse effects of the inverter nonlinearities on the injected high frequency square voltage is analyzed in [58]. The deadtime and current ripple distortion effects on the high frequency induced currents is investigated in detail to propose a method for removing these effects. The proposed method is implemented in an interior permanent magnet motor to verify the applicability of the sensorless scheme.

A position sensorless scheme based on high frequency square wave voltage injection to remove extra low pass filters used in sinusoidal voltage injection based schemes is proposed in [59]. The bandwidth of both current and speed loop is increased with the proposed scheme to enhance the dynamics of the system. With the injected frequency closer to the switching frequency, the fundamental frequency is well separated of the injected frequency. Therefore, low pass filters are not required to extract the fundamental component of the current.

1.6. Research Objectives

The objective of this research has been the efficiency and reliability enhancement of six phase synchronous motors. A real time phase swapping scheme is proposed to adaptively update the number of the active inverter legs depending on the demanded electric load to maximize the efficiency of the drive system by both considering stator copper and converter losses simultaneously. This scheme is mainly proposed for motors based on multiple three phase winding sets and the three phase inverter modules associated with each set are turned on/off. To enhance the reliability, a position sensorless scheme with simplified rotor position estimation error based on high frequency sinusoidal voltage injection is proposed. The proposed scheme reduces the number of low pass filters in [57] used in the algorithm to enhance the dynamics of the system. Both of the above mentioned schemes were implemented on experimental setups to verify their functionalities.

1.7. Thesis Outline

This dissertation is organized as follows:

Chapter one reviews the literature works performed in the similar areas. It starts with efficiency enhancement schemes considering only converter losses. Afterwards, several sensorless schemes are reviewed and their advantages and disadvantages are compared to each other. At the end of this chapter, the main reasons and objectives of this research is covered.

Chapter two analyzes different types of losses in a multiphase system. It is continued with simulating efficiencies of different multiphase cases considering only

converter losses, only stator copper losses and both of them. A new scheme is proposed to optimize the efficiency of the multiphase drive systems during the low load condition. Several drive techniques used in implementation of the proposed scheme are described later. Finally, the experimental setup used to verify the functionality of the proposed scheme is explained and the efficiency curves verify the functionality of the proposed scheme.

Chapter three starts with review of main sensorless schemes that have been proposed so far. They are compared in terms of dynamics, speed range coverage and torque ripple. The synchronous motor model at high frequency reference frame is considered and high frequency sinusoidal voltages are injected. The high frequency induced currents are derived. A rotor position estimator is developed to extract the rotor angle information based on the measured high frequency currents. An experimental setup is developed to implement the sensorless scheme. Finally, experimental results verify the accuracy of the rotor position estimation. Furthermore, the input to the rotor position estimator and the estimated angle of the proposed scheme is compared to that of the conventional scheme.

2. EFFICIENCY ENHANCEMENT OF MULTIPHASE ELECTRIC DRIVES AT LIGHT-LOAD OPERATION CONSIDERING BOTH CONVERTER AND STATOR COPPER LOSSES*

In electric vehicles for urban use, the drives work on a very variable regime and often operate for long periods of time with light load [27]. Similarly, in wind generation farms, the generators frequently function at low capacity depending on the wind speed; hence, the efficiency of wind turbines at light load is also considered important [25], [60 – 61]. In general, when the working regime is far from nominal, the machine-side converter efficiency is usually comparatively low [27]. Therefore, developing new methods for further efficiency enhancement of ac/dc converters, with special focus on light loads, is of paramount importance. Furthermore, such additional amelioration could be combined with previous approaches to yield an even better total efficiency.

In [13] and [62], a converter structure based on several three-phase back-to-back converters is considered for a wind turbine, with the grid-side inverters being in parallel. It is proposed to adaptively enable or disable the entire back-to-back converter modules. In this manner, advantage is taken of the fact that the losses of semiconductor devices, with respect to the output power, drop when they operate close to their rated condition [5], [13], [25], [63]. However, such structure is relatively bulky and expensive [64]; note that it has several three-phase grid-side inverters with individual dc links, additional

* Reprinted with permission from "Efficiency Enhancement of Multiphase Electric Drives at Light-Load Operation Considering Both Converter and Stator Copper Losses" by A. Negahdari, A.G. Yepes, J. D. Gandoy and H. A. Toliyat, 2018. IEEE Transactions on Power Electronics, Copyright [2018] by IEEE.

switches (to effectively interrupt the current through the converters) on both the machine and grid sides, and interfacing inductors in the grid side. The improvement in efficiency was estimated when these multiple grid-side converters are also enabled/disabled adaptively; but it is unclear if, in absence of grid-side inverters or with a single three-phase grid-side inverter, the enabling/disabling approach is still convenient when only applied to the machine-side converter. In addition, the stator copper losses of the machine were not taken into account, in spite of the fact that they are expected to increase with the phase current [65]. Moreover, the improvement in efficiency was only estimated, not experimentally measured.

This dissertation proposes a method to improve the efficiency of multiphase electric drives for machines with multiple three-phase windings. The proposed technique is based on modifying the number of active legs during the machine operation depending on the reference torque, while ensuring that the demanded power is always provided. Consequently, the efficiency is enhanced mainly at light load. Besides the converter losses, the effect of the stator copper losses on the overall efficiency is also studied and taken into account in the strategy. Experimental results are provided to verify the conclusions of the theoretical study.

The rest of this chapter is organized as follows. Section 2.1 describes the general structure of the analyzed system and reviews the main losses in ac/dc converters. Section 2.2 analyzes the condition in which only the converter losses are considered for improving the efficiency. Section 2.3 describes the proposed method to enhance the overall system efficiency. Section 2.4 presents the experimental results.

2.1. Background

A. Multiphase drives based on multiple three-phase windings:

The generalized schematic for a multiphase drive based on multiple three-phase stator windings with isolated neutrals is shown in Fig. 2.1, where γ equals 2 or 1 for symmetrical or asymmetrical winding arrangements, respectively [25], and n stands for the total number of phases.

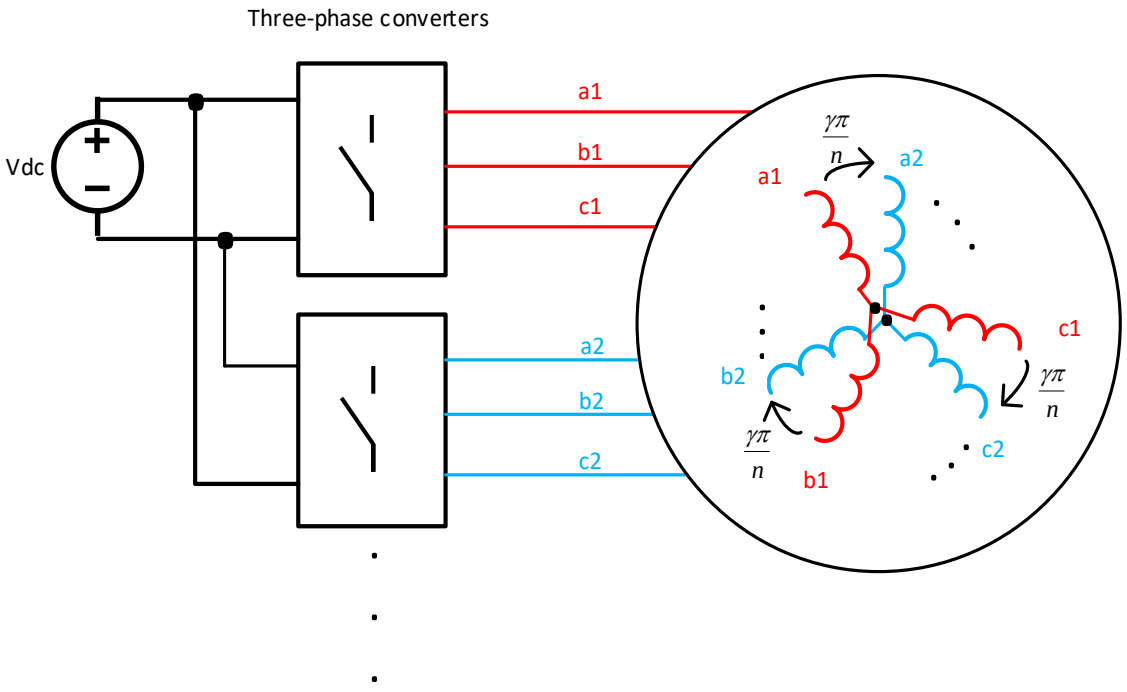

Fig. 2.1: Generalized schematic of an electric drive based on multiple three-phase windings with isolated neutrals.

The converter consists of $n/3$ three-phase modules connected to a single dc bus. Each of these modules supplies a three-phase winding set of the machine. The dc source shown in Fig. 2.1 may represent in a simplified manner, e.g., the batteries in an electric

vehicle or the dc side of a three-phase grid-connected converter in a wind turbine system.

B. Major converter loss components

The losses in ac/dc converters are divided into the following two parts.

1) *Conduction losses*: The on-state resistances of semiconductor switches and of anti-parallel diodes cause ohmic losses while they conduct. These losses are given by the following equations:

$$P_{cond,tr} = \frac{1}{2}\left(V_{ce0}\frac{I}{\pi} + r_{ce}\frac{I^2}{4}\right) + m\cos\phi\left(V_{ce0}\frac{I}{8} + \frac{r_{ce}I^2}{3\pi}\right) \tag{2.1}$$

$$P_{cond,d} = \frac{1}{2}\left(V_{d0}\frac{I}{\pi} + r_{d}\frac{I^2}{4}\right) - m\cos\phi\left(V_{d0}\frac{I}{8} + \frac{r_{d}I^2}{3\pi}\right) \tag{2.2}$$

where P_{cond}, tr, d, V_{ce0}, V_{d0}, r_{ce}, r_d, m, $\cos\phi$ and I denote conduction losses, transistor, diode, switch collector-emitter voltage, diode forward voltage drop, collector-emitter on-state resistance, diode on-state resistance, modulation index, power factor and rms phase current, respectively.

2) *Switching losses*: The losses associated with non-ideal switching exist on both the diodes and the switches, and they are given by

$$P_{sw,tr} = f_{sw}(E_{on} + E_{off})\left(\frac{I_{in}}{I_{ref}}\right)^{k_{i,tr}}\left(\frac{V_{out}}{V_{ref}}\right)^{k_{v,tr}}\left(1 + T_{c,tr}(T_j - T_{ref}\right) \tag{2.3}$$

$$P_{sw,d} = f_{sw}(E_{rr})\left(\frac{I_{in}}{I_{ref}}\right)^{k_{i,d}}\left(\frac{V_{out}}{V_{ref}}\right)^{k_{v,d}}\left(1 + T_{c,d}(T_j - T_{ref}\right) \tag{2.4}$$

where P_{sw}, f_{sw}, E_{on}, E_{off}, E_{rr}, T_j, T_{ref}, T_c, k_i, k_v, I_{in}, I_{ref}, V_{out} and V_{ref} represent switching losses, switching frequency, switch turn-on losses, switch turn-off losses, diode reverse-

recovery losses, junction temperature, reference temperature, temperature coefficient, current ratio order, voltage ratio order, device input current, device reference current, device voltage and device reference voltage, respectively.

2.2. Converter Efficiency Enhancement

In the following, the multiphase ac/dc converter efficiency is analyzed when one or more of the multiple three-phase winding sets are deactivated (by turning off the corresponding converter switches) as the load decreases, so that the current per phase is maximized (for such load) but the switch current rating is not surpassed. Henceforth, this approach is called strategy for enhancement of the converter efficiency (SECE).

Table 2.1

Characteristics of the 24-Phase PMSM

Parameter	**Value**
Rated Power	20 kW
Rated Speed	1800 rpm
Rated Torque	106.1 Nm
Number of Poles	4
Rated Voltage	120 V (rms)
Rated Current	12 A
Stator Resistance	0.2 Ω
Stator self-inductance	800 μH

Without loss of generality, a practical case is chosen for the study, for the sake of convenience and illustration. A 24-phase (eight three-phase winding sets) surface-

mounted permanent-magnet synchronous machine (PMSM), with the characteristics shown in Table 2.1, is adopted. By choosing a 24-phase machine, the resulting plots will also allow to analyze later the cases of machines with lower phase numbers, such as six. The PMSM is assumed to operate at rated speed. The main parameters of the converter diodes and switches [insulated gate bipolar transistors (IGBTs)] are given in Table 2.2. The Semikron SKM50GB half-bridge modules with SEMIx302GB12E4s IGBT switches are used. The switching frequency is initially set to 5 kHz. The impact of other parameter choices is discussed later on.

Table 2.2

Characteristics of the Semiconductor Devices

Variable	**Value**
V_{ce0}	0.9 V
V_{d0}	1.1 V
r_{ce}	0.044 Ω
r_d	0.018 Ω
T_{ref}	25 ^{0}C
$K_{i,tr}$	1
$K_{v,tr}$	1.35
$K_{i,d}$	0.6
$K_{v,d}$	0.6
$T_{c,d}$	0.003 1/K

The efficiency of the 24-phase converter supplying the stator terminals is evaluated at different operation modes in Fig. 2.2, for various load (torque is normalized with respect

to the rated torque) conditions. Such modes result from enabling or disabling three-phase winding sets. There are eight modes; namely, with one, two, three, and up to eight simultaneously active three-phase winding sets. For simplicity, just six of these modes are depicted in Fig. 2.2; the 15-phase and 21-phase curves would be placed in between. It should also be mentioned that for Fig. 2.2 the efficiency is calculated from the dc bus to the stator input power, so that only the effect of the converter losses is reflected.

As shown in Fig. 2.2, at light load condition the three-phase configuration yields the highest efficiency, and as the load increases, the 6-, 9-, 12-, 18- and 24-phase mode is successively the best candidate for improving the converter efficiency. The trajectory shown in dashed magenta corresponds to the SECE. As the torque increases, three-phase winding sets are consecutively activated in the SECE. It can be seen that the SECE tracks in this manner the highest converter efficiency available at each time (torque).

Fig. 2.2 also shows that the SECE enhances the converter efficiency for machines of phase numbers lower than 24, as well. For this reason, the choice of 24 phases for the example proves to be particularly convenient. As aforementioned, although the simulations are initially presented as performed for a 24-phase machine with rated power P=20 kW, in reality the resulting plots illustrate the efficiency results also for n-phase machines with rated power $Pn/24$, where n can be 6, 9, 12 and 18. For instance, it is inferred from Fig. 2.2 that for a 6-phase machine (with rated power and torque of 5 kW and 26.5 Nm, respectively, in this example), efficiency can be improved for light load (below 0.65 p.u.) by selecting between 3 or 6 active phases (two operation modes).

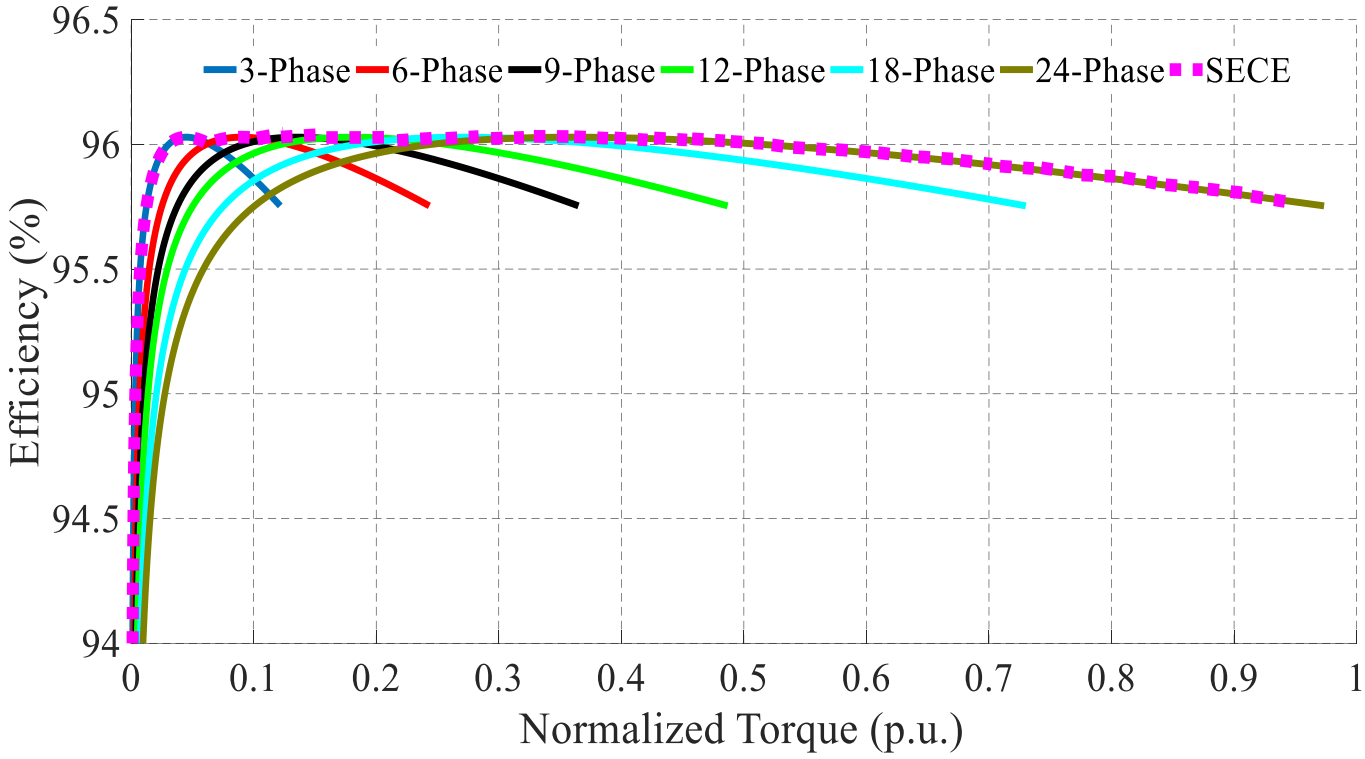

(a)

Fig. 2.2. Efficiency comparison, considering only the converter losses, of utilization of different number of converter legs and the SECE with operation at (a) full range of load, and (b) light load (zoomed).

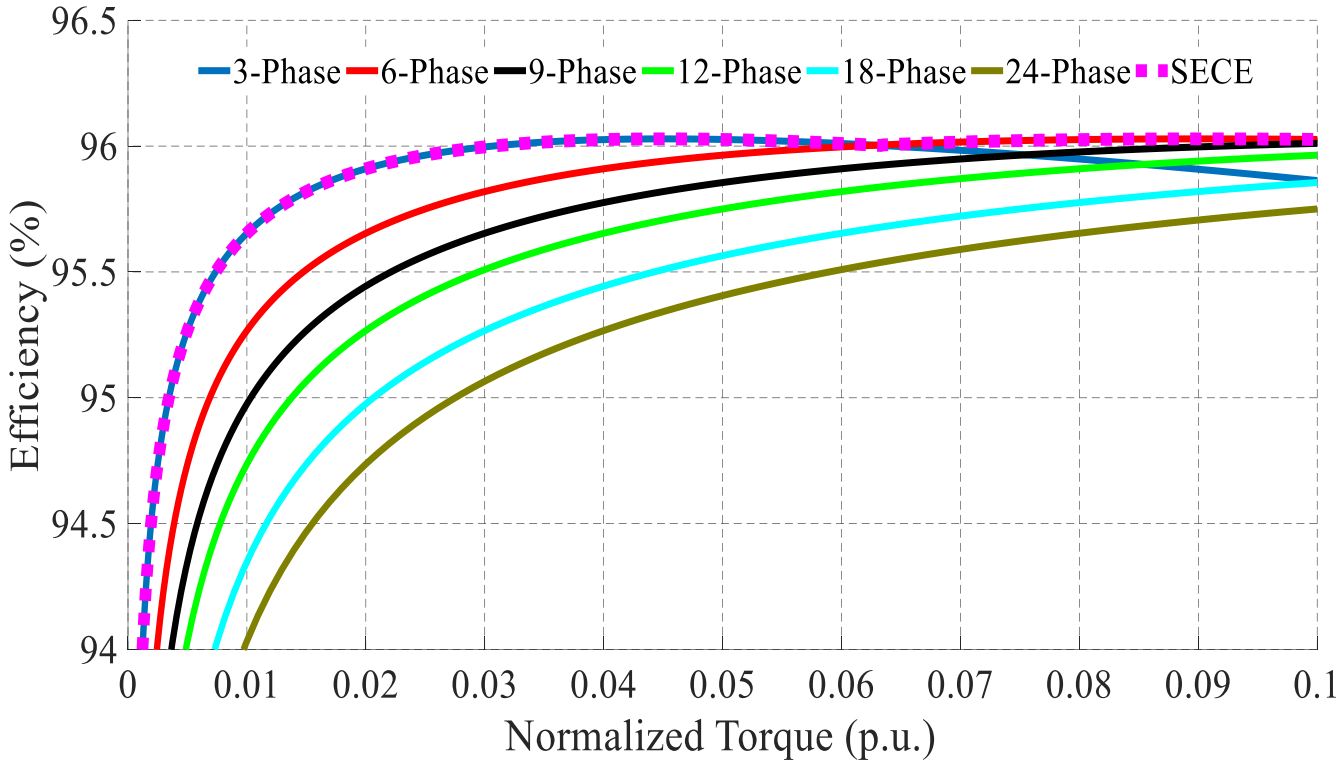

(b)

Fig. 2.2. Continued.

2.3. Proposed Strategy for Enhancement of Overall Efficiency

In the previous section, it was shown that the SECE permits to increase the converter efficiency. However, the stator copper losses were ignored (as in, e.g., [13], [63]), in spite of the fact that they are another major loss component in electric drives, and they vary with the number of active legs and the phase current rms [7]:

$$P_{cL} = nR_s I^2 \tag{2.5}$$

where P_{cL}, n and R_s stand for stator copper losses, number of active converter legs and stator resistance, respectively. In this section, the effect of the stator copper losses on the overall efficiency is studied when applying the SECE, and a strategy for enhancement of the overall efficiency (SEOE) is proposed. Such SEOE optimizes the overall efficiency, by also taking into account the stator copper losses. The effect of the different operation modes of the SECE on the stator copper losses is evaluated in Fig. 2.3. Only the copper losses are taken into account for the efficiency computation in this figure. The machine and converter under study are the same as in Section 2.2. From Fig. 2.3, it can be seen that reducing the number of active converter legs results in lower efficiency in terms of copper losses, for all load values. Nevertheless, although the copper losses are increased if the number of active legs is reduced, the overall efficiency (see Fig. 2.4) is still improved when decreasing the phase number. The reason is that the converter loss reduction dominates over the increase in the copper losses. By taking into account both converter and copper losses, the SEOE is proposed in here. As also depicted in Fig. 2.4, the SEOE selects the number of active phases such that the overall system efficiency is optimized for each load.

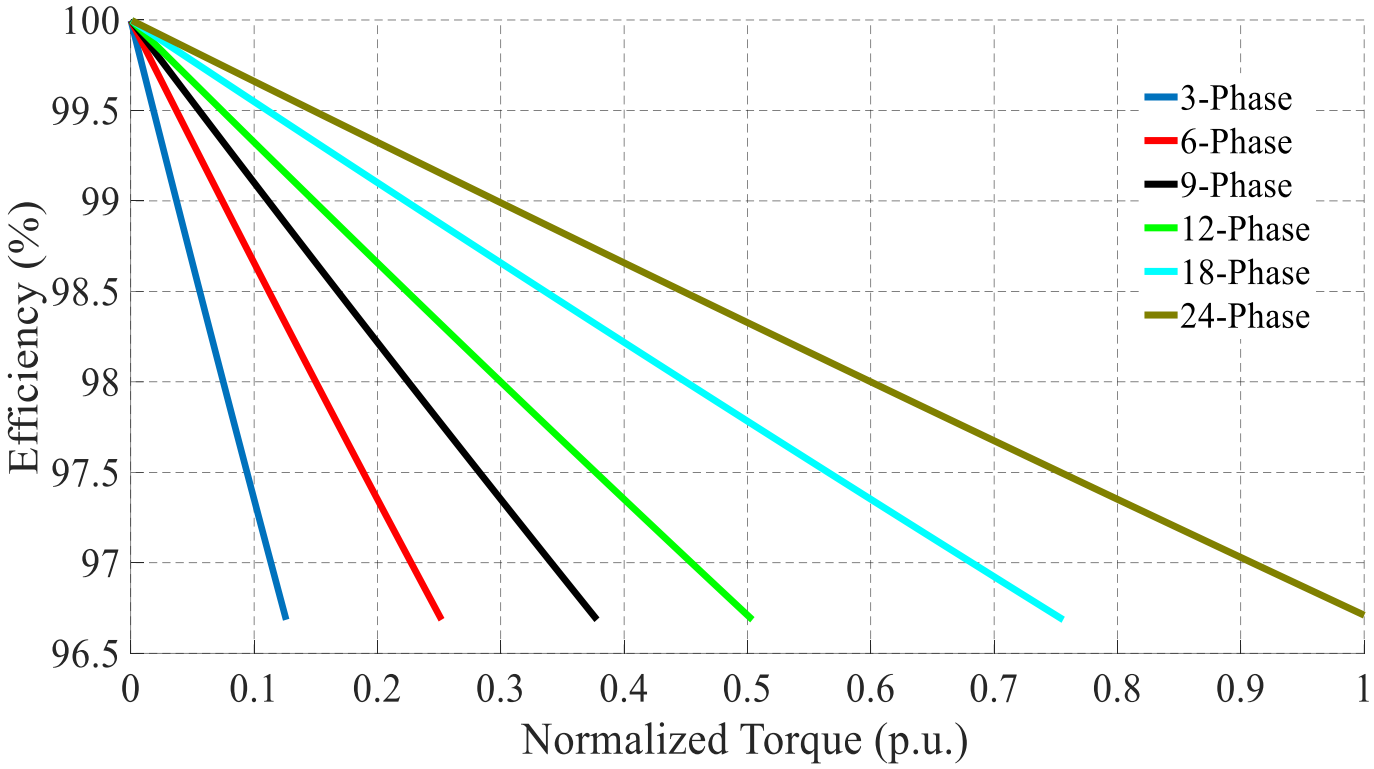

(a)

Fig. 2.3. Efficiency comparison, considering only the stator copper losses, of utilization of different number of converter legs with operation at (a) full range of load, and (b) light load (zoomed).

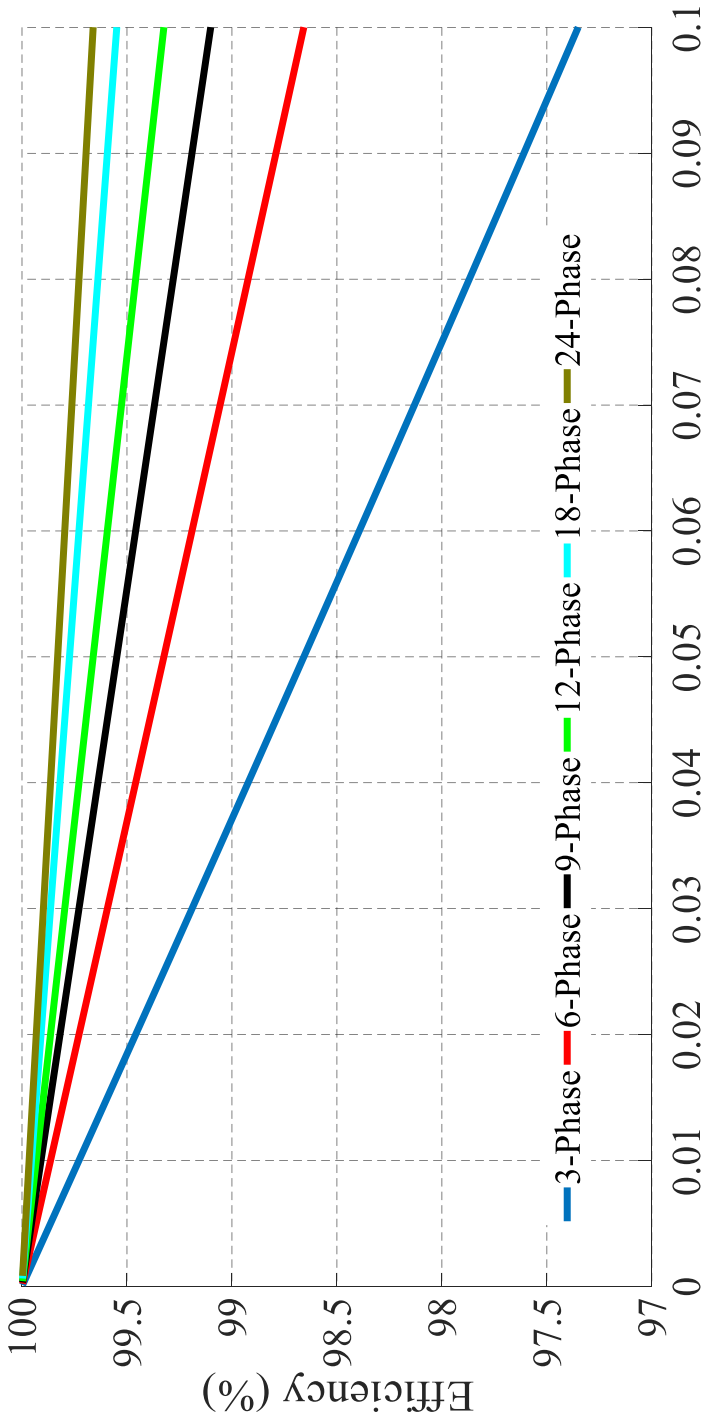

(b)

Fig. 2.3. Continued.

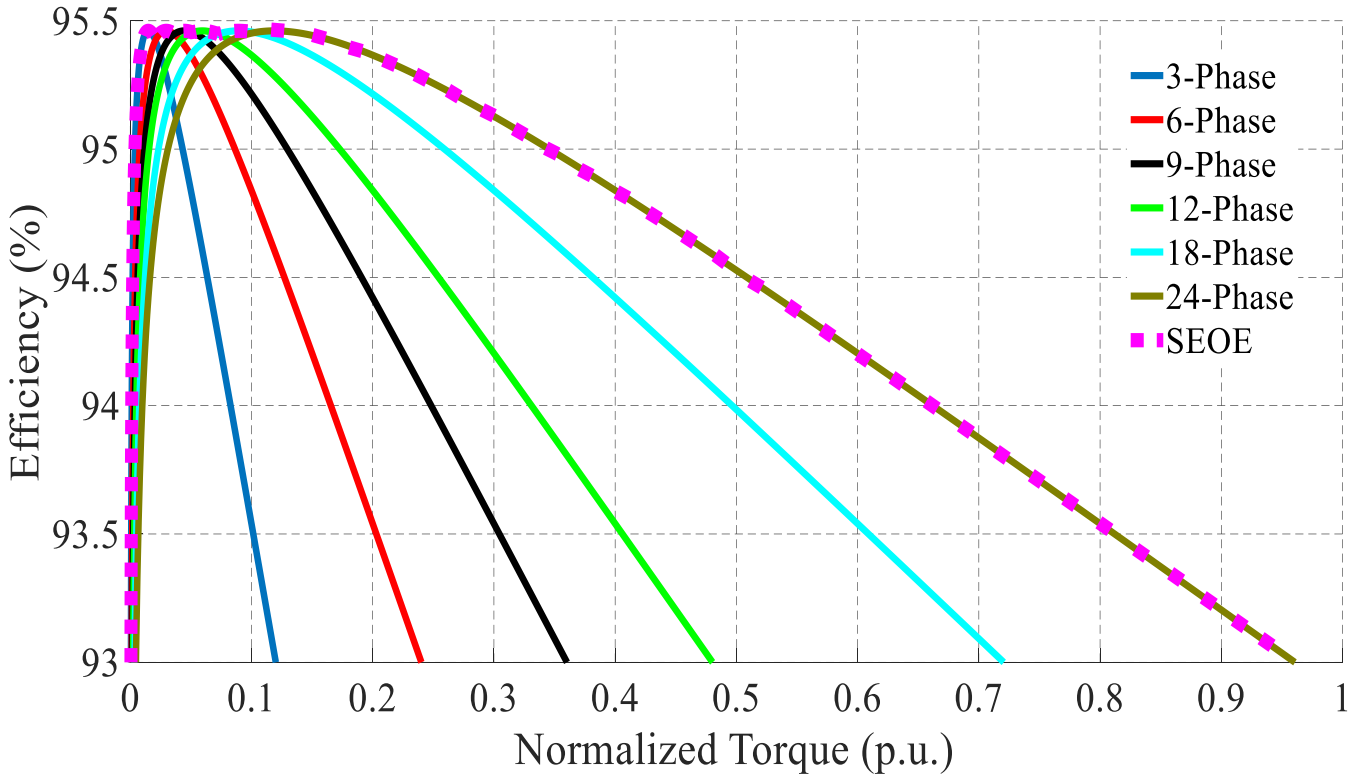

(a)

Fig. 2.4. Efficiency comparison, considering both the converter and copper losses, of utilization of different number of converter legs and the SEOE with operation at (a) full range of load, and (b) light load (zoomed).

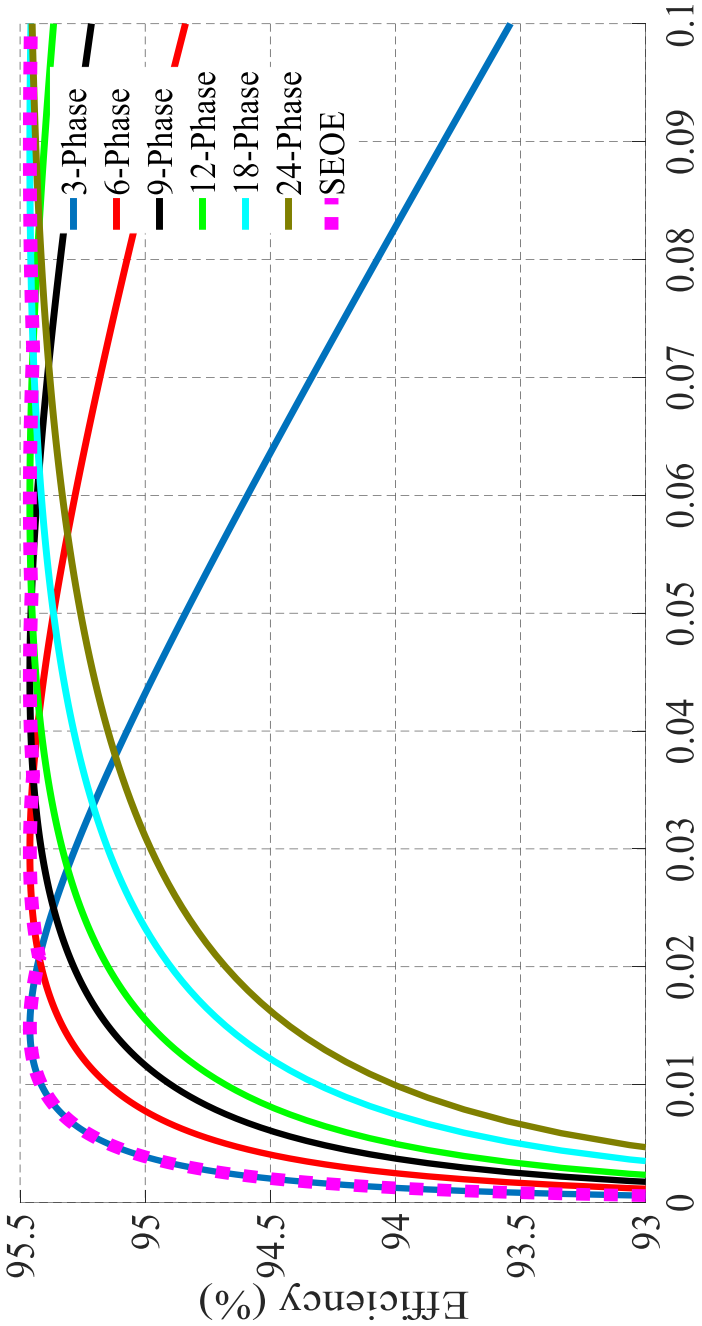

(b)

Fig. 2.4. Continued.

By comparing Figs. 2.2 and 2.4, it can be observed that the load torque at which the phase numbers are changed is different for SECE and SEOE. For example, when only converter losses are considered (Fig. 2.2), the three- and six-phase modes should be swapped for a normalized torque of 0.64 p.u., whereas in the case of total efficiency (Fig. 2.3), this occurs at 0.22 p.u. Similarly, the torque values for the commutation between other modes also differ between the SECE and SEOE. This fact can be noted more clearly in Fig. 2.5, which compares in the same figure the efficiency-versus-torque curves corresponding to the SECE and SEOE. Again, in Fig. 2.5 the transitions involving the modes of 15 and 21 phases are omitted for clarity and simplicity. From Fig. 2.5, if the SECE is implemented instead of the SEOE, the overall efficiency is not optimized and drops significantly as the load rises. For example, it is shown that the maximum difference in overall efficiency between SECE and SEOE occurs at 0.063 p.u. output torque and is almost 1%. By performing SEOE (shown in blue), the overall efficiency is maintained at about 95.5% whereas if SECE is implemented, the overall efficiency drops to roughly 94.5%. Thus, the SEOE is clearly preferable over the SECE.

The torque (current) values that are used as threshold for the SECE or SEOE should be obtained off-line for a given machine and converter, so that the real-time control can swap on-line between modes at the correct condition. Such threshold values can be measured or simply computed by equating the overall efficiencies for each pair of consecutive operation modes, using (2.1)-(2.5).

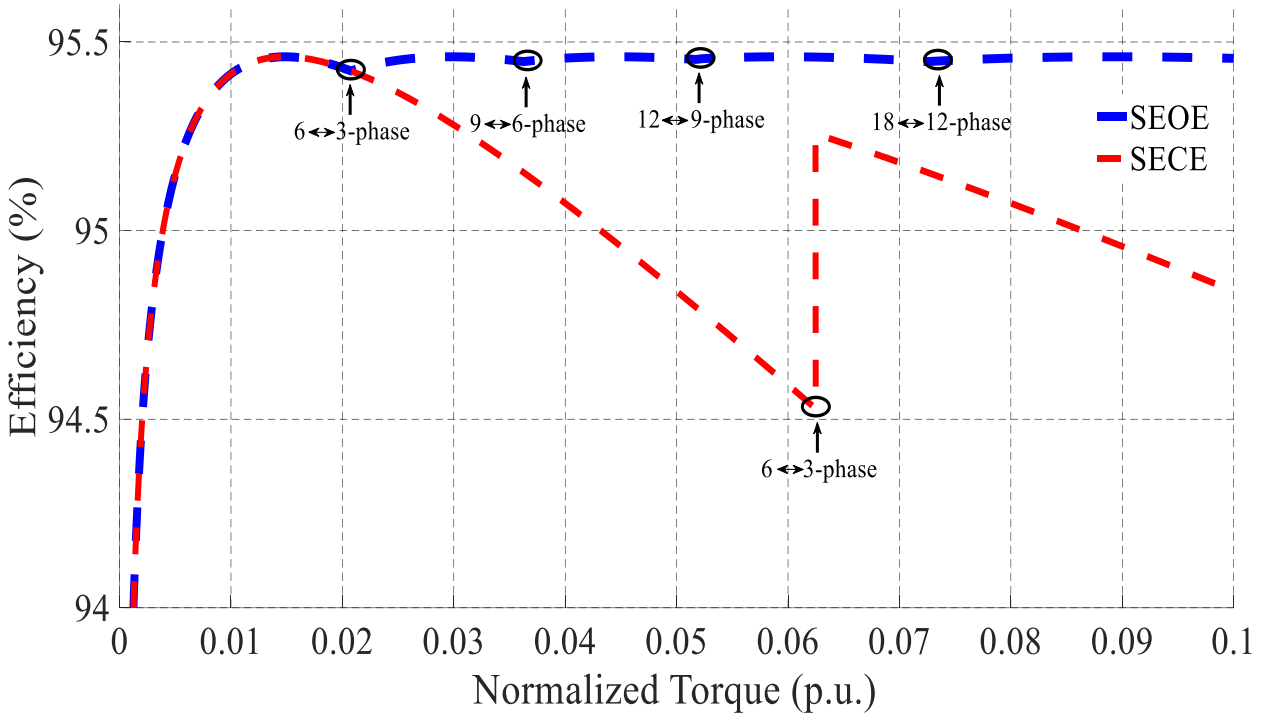

Fig. 2.5. Comparison of the SECE and SEOE in terms of overall efficiency and threshold output-power values.

Amounts of efficiency improvement similar to the ones attained here are often considered to be substantial [27], [30], [66]. Furthermore, even if the efficiency difference may seem relatively small in terms of power, it can result in a significant amount of energy when integrated through a long period of time.

Other existing losses such as those due to other converters, iron core, windage, friction, etc. are not expected to vary substantially for a given torque and speed when the number of active legs is altered. In addition, the choice of symmetrical or asymmetrical winding arrangement for the stator does not affect the efficiency analysis.

Finally, the influence of some parameter variations on the SEOE performance is addressed in the following.

Fig. 2.6 shows the overall efficiency for the same PMSM with three different stator resistances. When the stator resistance increases (R_s=2 Ω), the overall efficiency drops accordingly and the SEOE mode swapping happens at lighter loads. On the other hand, when the stator resistance decreases (R_s=0.02 Ω), the overall efficiency increases and the SEOE mode commutation has to be applied at higher loads, which potentially permits to save more energy. In conclusion, the SEOE offers greater loss reduction for machines with lower stator resistance. This occurs because for smaller R_s the converter efficiency has comparatively (with respect to the copper losses) more weight on the overall efficiency. As shown in Fig. 2.7, the efficiency diminishes over the whole range with the rise in switching frequency, since the switching losses of the converter grow accordingly [(2.3) and (2.4)]. On the other hand, the threshold load values become higher, because of the increased relevance of the switching losses in the overall

efficiency. This fact implies a larger potential saving of energy by using the SEOE with respect to the usual approach of maintaining the phase number. As a consequence, when the switching frequency is chosen for a drive implementing the SEOE, a trade-off should be met, depending on the application, regarding the general decrease in efficiency and the improvement in the SEOE saving that occur when f_{sw} grows.

Concerning the magnitude of the back electromotive force (back-EMF) and the speed, they are not expected to have a noticeable impact on the preceding curves of efficiency, mainly due to the torque normalization. Nonetheless, it should be noted that even with identical efficiency, the power quantities are more important when the speed or BEMF are close to the rated one.

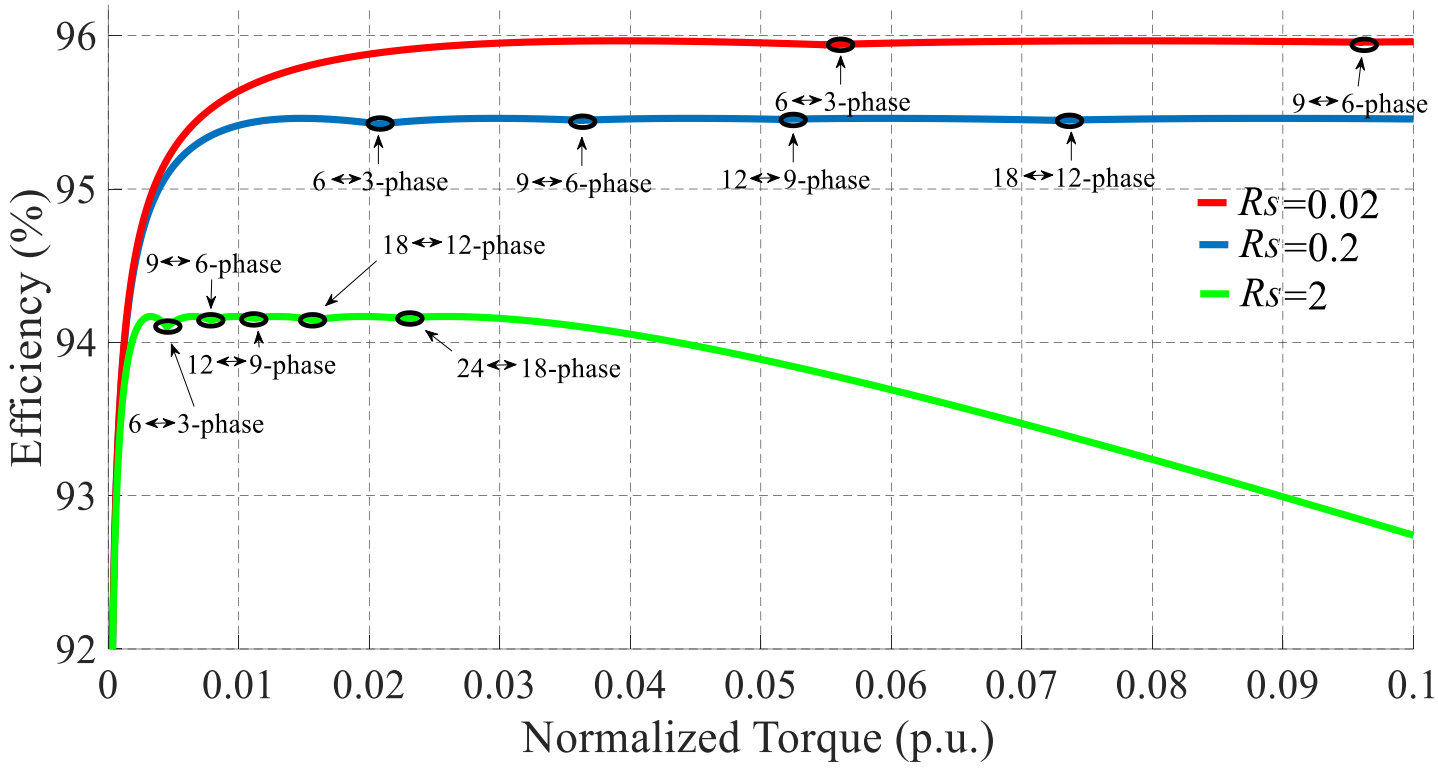

Fig. 2.6. Comparison of the SEOE for machines with different stator resistances.

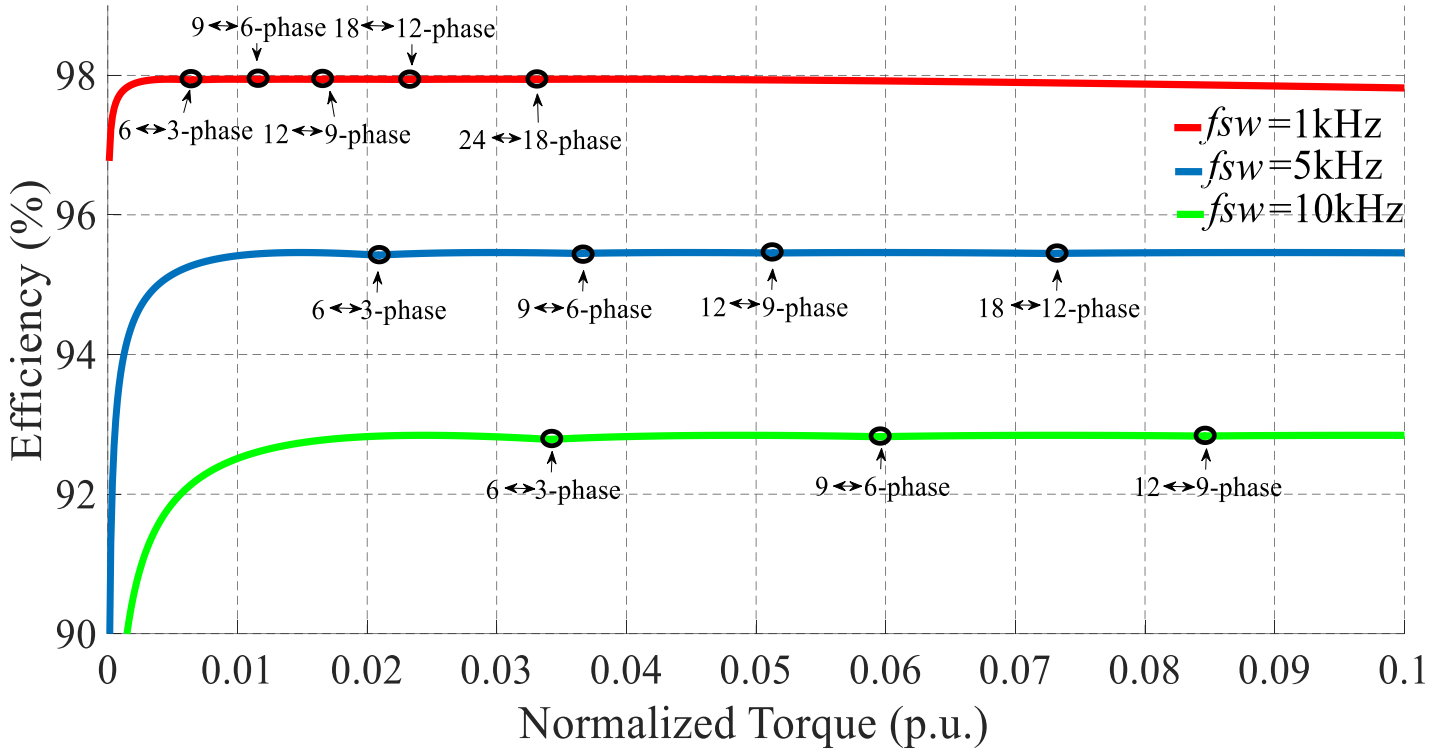

Fig. 2.7. Analytical comparison of SEOE for converters with different switching frequencies.

2.4. Experimental Setup

An experimental prototype (see Fig. 2.8) is built to verify the theoretical outcomes and functionality of the proposed SEOE. A 6-phase wound-field synchronous motor with small saliency and symmetrical winding arrangement is driven by field-oriented control using two three-phase inverter modules. Disregarding saliency, the characteristics of the machine coincide with those in Table 2.1, by simply multiplying by a factor of 0.225 the values of rated power and torque shown in the Table 2.1. A Texas Instruments Delfino TMS320F28377 digital signal processor (DSP) is used for the control implementation. The two dimensional finite element analysis model of the synchronous motor is shown in Fig. 2.9. Some of the parameters of the motor is also described in Table 2.3.

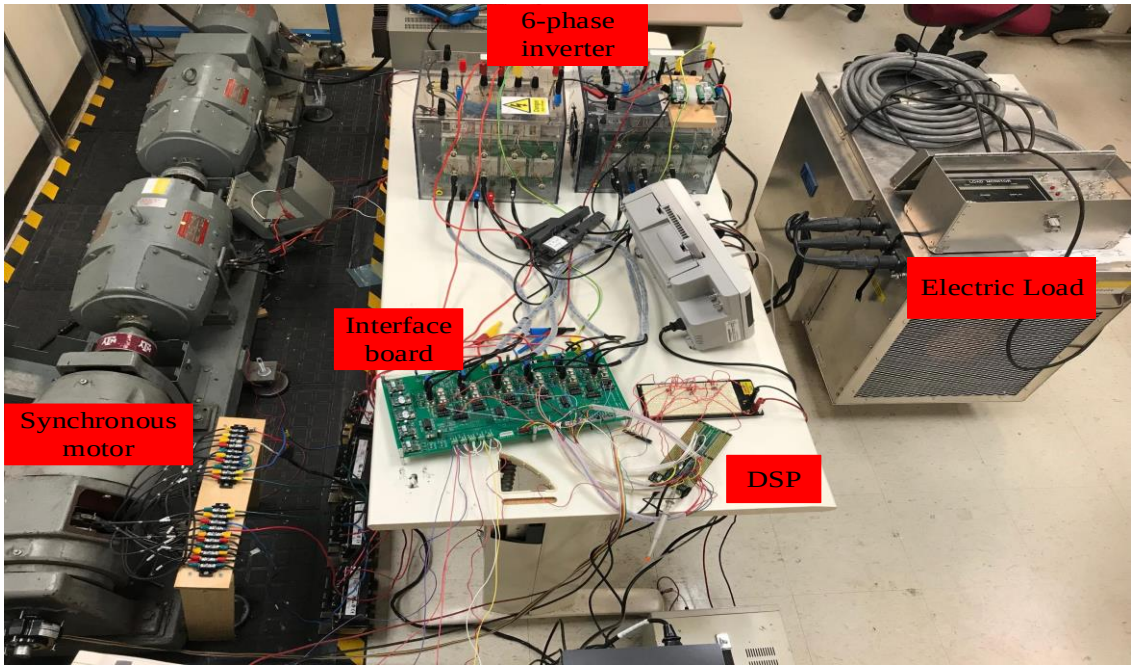

Fig. 2.8. Experimental setup.

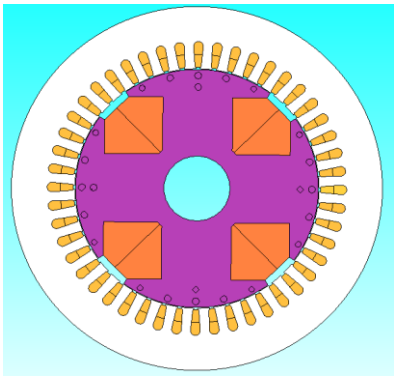

Fig 2.9: FEA model of the synchronous motor stator and rotor showing double layer short pitched windings, adapted.

Table 2.3: Synchronous motor parameters.

Rated power	5 kVA
Number of Poles	4
Rated voltage	240 V
Rated current	12 A
Power factor	0.8
Number of winding layers per stator slot	2
Number of turns per coil	6
Number of coils per phase	4
Number of stator slots	48
Air gap length	0.5 mm
Rotor outer radius	87 mm
Rotor inner radius	23.75 mm
Stator outer radius	133 mm

The original synchronous motor shown above was wound as a three-phase motor with external taps on the stator windings as shown in Fig. 2.10 which enables the configurability of the stator windings.

(a)

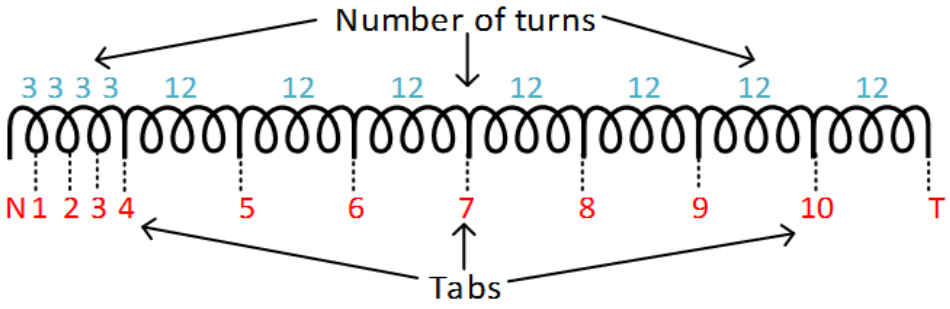

(b)

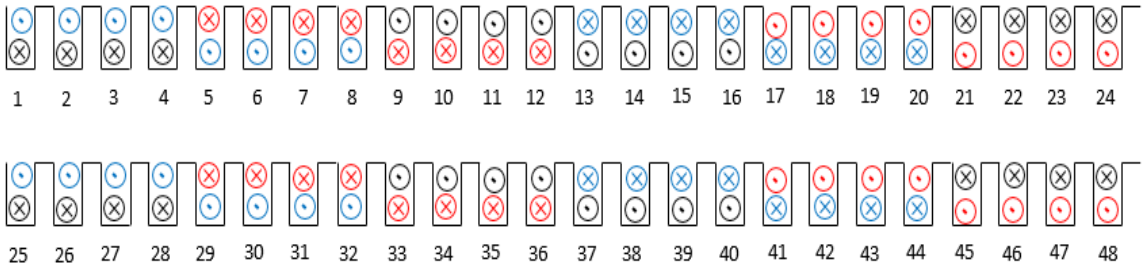

(c)

Fig. 2.10: Original motor winding configuration, a) actual external taps, b) schematic of the taps along the winding, and c) coils end connection.

The connections were updated as shown in Fig. 2.11 to form a symmetrical six-phase synchronous motor.

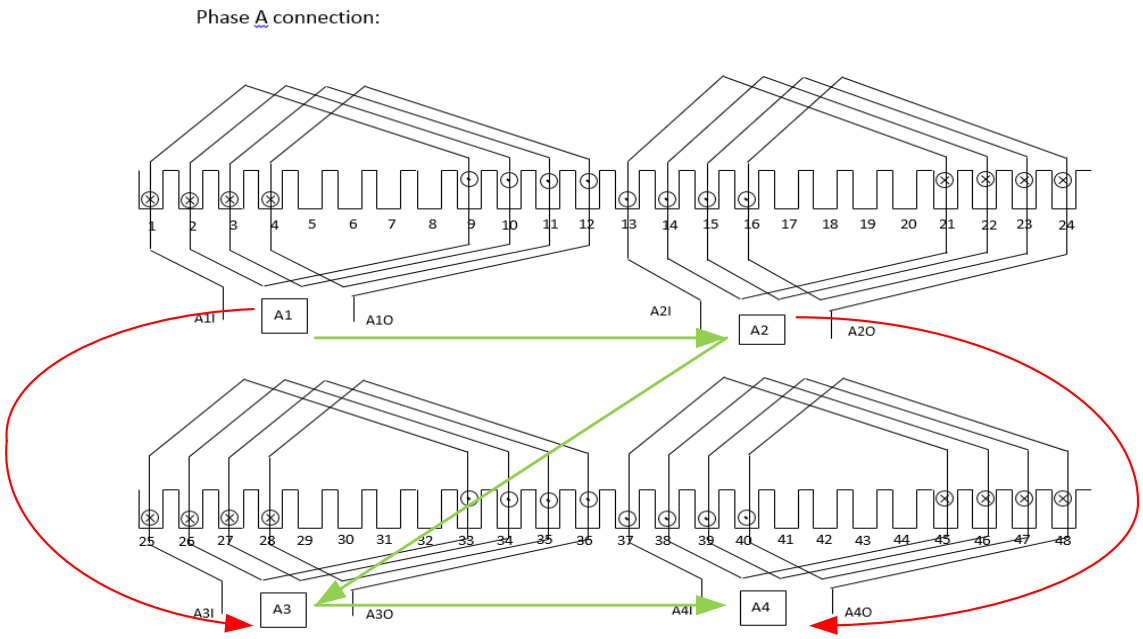

(a)

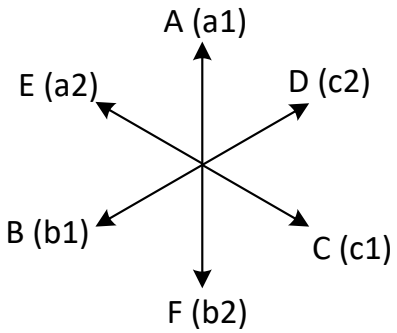

(b)

Fig. 2.11: Three to six-phase reconfiguration. a) distributed layout (green arrows refer to old connections and red arrows refer to new connections.) and b) Spatial representation of the phase vectors.

The new six-phase system acts like two sets of three-phase systems which are shifted for 60 degrees with respect to each other. The phase back-EMFs for all six phases of the new machine are shown below to verify the correct phase shifts:

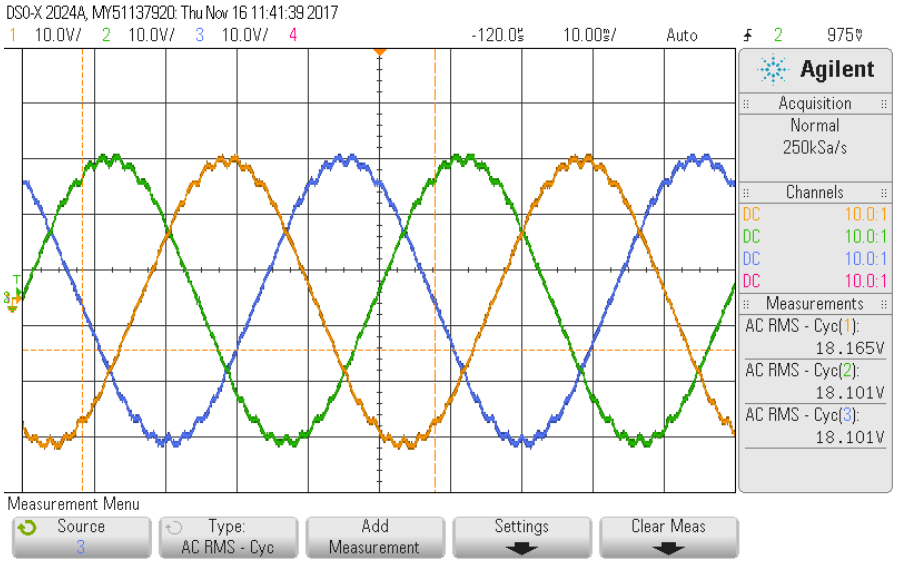

(a)

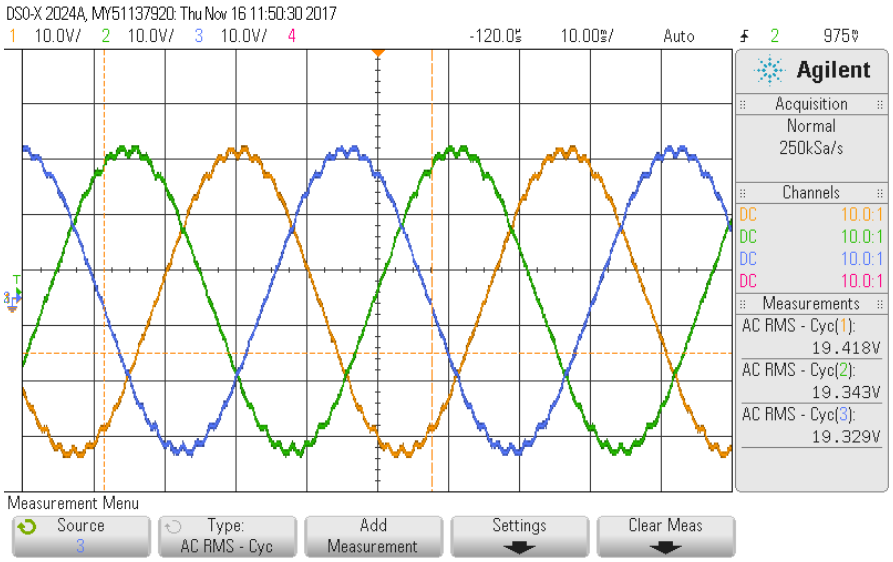

(b)

Fig. 2.12: Phase back EMFs for a) 1st three-phase and b) 2nd three-phase set.

2.5. Drive Schemes

As part of the experimental setup, a digital control platform is provided to implement the required motor drive strategies. This platform consists of the microcontroller, the three phase full bridge inverter sets and the control software. The Texas Instrument Delfino TMS28F379D series of the C2000 families is used for processing. A comprehensive code was also written in code composer studio (CCS). Semikron three phase inverter sets are used as well.

The main drive scheme is equal in both chapters one and two. Two IGBT based voltage source inverters used to drive both wound field synchronous motor and the surface mount permanent magnet synchronous motor. The DSP commands the inverter switches with the generated PWM signals as the output of the control schemes. An interface board is responsible to isolate and amplify the transferred signals between the DSP and the inverter. The main control loop of this system consists of the inner current loop and the outer speed loop.

In order to control the machine in the rotating reference frame, the motor needs to be modelled in the *dq* synchronous reference frame. Equation (2.6) and (2.7) describes the voltage equation in the *d* and *q* axes.

$$v_d = (R_s + j\omega_e L_d)i_d - \omega_e L_q i_q + \omega_e \lambda_r \tag{2.6}$$

$$v_q = \omega_e L_d i_d + (R_s + j\omega_e L_q)i_q \tag{2.7}$$

where v_d, v_q, i_d, i_q, L_d, L_q, R_s, ω_e and λ_r stand for d axis voltage, q axis voltage, d axis current, q axis current, d axis inductance, q axis inductance, stator series resistance, rotor angular speed and back-EMF. In the case of the surface mount permanent magnet

synchronous motor, there is no excitation on the rotor so the back-EMF term in (2.6) will be zero. Also, in the case of the wound field synchronous motor, the rotor field winding is not excited and hence the back-EMF term does not exist.

Assuming the back-EMF is zero, the flux linkages along the *d* and *q* axes are defined by (2.8) and (2.9):

$$\lambda_d = L_d I_d \tag{2.8}$$

$$\lambda_q = L_q I_q \tag{2.9}$$

Consequently, the *dq* axis equivalent circuit of the synchronous motors can be represented by:

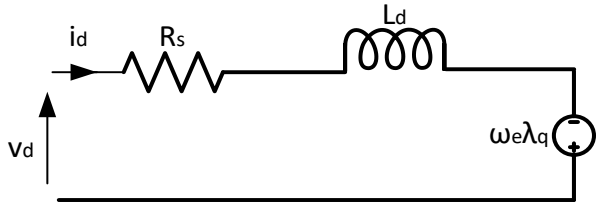

(a)

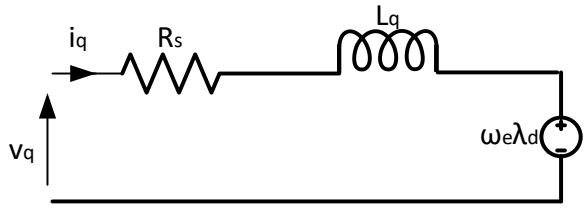

(b)

Fig. 2.13: Equivalent circuit of the synchronous motors in *d* and *q* axes.

When implementing the field oriented control (FOC) for the motor, several techniques are incorporated to improve the operation of the motor.

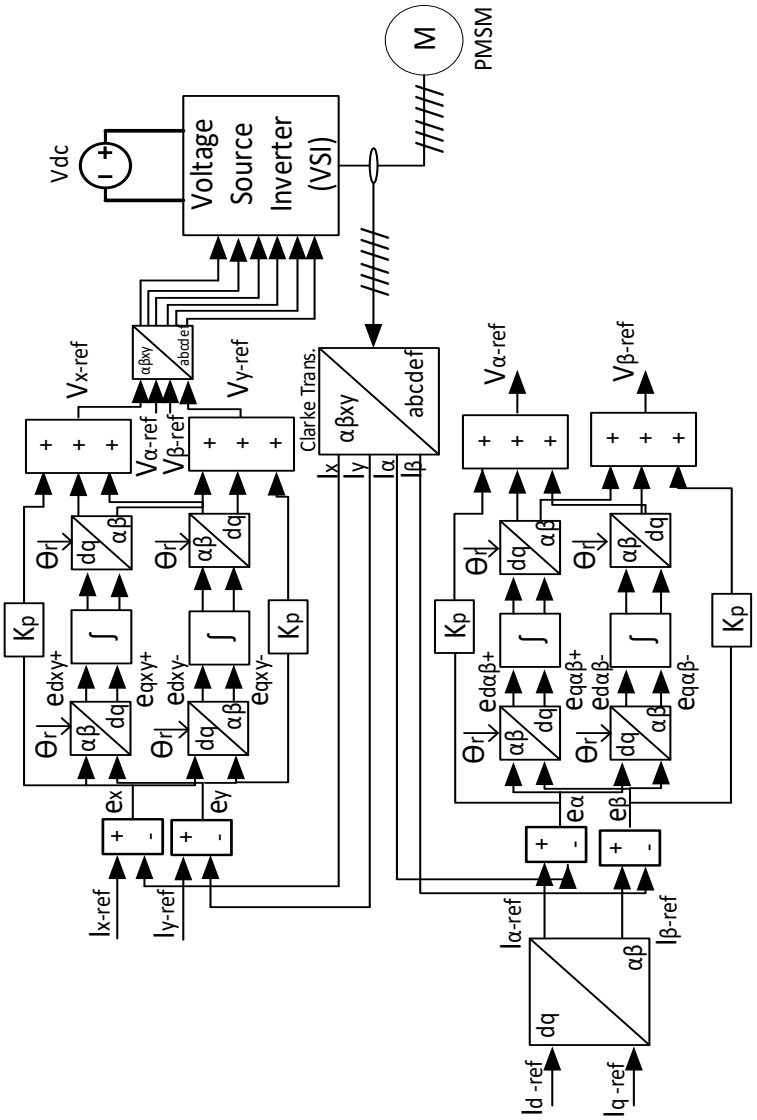

Fig. 2.14: Overall FOC block diagram of the system.

Fig. 2.14 depicts the overall block diagram of the control scheme which tracks the fundamental component of the commanded current reference.

The six phase currents are converted to *αβxy* parameters using the following Clarke transformation for the asymmetrical six phase synchronous machine.

$$\begin{matrix} i_\alpha \\ i_\beta \\ i_x \\ i_y \\ i_{0+} \\ i_{0-} \end{matrix} = \sqrt{\frac{2}{6}} \begin{bmatrix} 1 & \cos(\frac{2\pi}{3}) & \cos(\frac{4\pi}{3}) & \cos(\frac{\pi}{6}) & \cos(\frac{5\pi}{6}) & \cos(\frac{9\pi}{6}) \\ 0 & sin(\frac{2\pi}{3}) & sin(\frac{4\pi}{3}) & sin(\frac{\pi}{6}) & sin(\frac{5\pi}{6}) & sin(\frac{9\pi}{6}) \\ 1 & \cos(\frac{4\pi}{3}) & \cos(\frac{8\pi}{3}) & \cos(\frac{5\pi}{6}) & \cos(\frac{\pi}{6}) & \cos(\frac{9\pi}{6}) \\ 0 & sin(\frac{4\pi}{3}) & sin(\frac{8\pi}{3}) & sin(\frac{5\pi}{6}) & sin(\frac{\pi}{6}) & sin(\frac{9\pi}{6}) \\ 1 & 1 & 1 & 0 & 0 & 0 \\ 0 & 0 & 0 & 1 & 1 & 1 \end{bmatrix} \begin{matrix} i_a \\ i_b \\ i_c \\ i_d \\ i_e \\ i_f \end{matrix} \tag{2.10}$$

For the case of the symmetrical six phase synchronous motor, the Clarke transformation is represented by:

$$\begin{matrix} i_\alpha \\ i_\beta \\ i_x \\ i_y \\ i_{0+} \\ i_{0-} \end{matrix} = \sqrt{\frac{2}{6}} \begin{bmatrix} 1 & \cos(\frac{\pi}{3}) & \cos(\frac{2\pi}{3}) & \cos(\pi) & \cos(\frac{4\pi}{3}) & \cos(\frac{5\pi}{3}) \\ 0 & sin(\frac{\pi}{3}) & sin(\frac{2\pi}{3}) & sin(\pi) & sin(\frac{4\pi}{3}) & sin(\frac{5\pi}{3}) \\ 1 & \cos(\frac{2\pi}{3}) & \cos(\frac{4\pi}{3}) & \cos(2\pi) & \cos(\frac{8\pi}{3}) & \cos(\frac{10\pi}{3}) \\ 0 & sin(\frac{2\pi}{3}) & sin(\frac{4\pi}{3}) & sin(2\pi) & sin(\frac{8\pi}{3}) & sin(\frac{10\pi}{3}) \\ 1 & 1 & 1 & 0 & 0 & 0 \\ 0 & 0 & 0 & 1 & 1 & 1 \end{bmatrix} \begin{matrix} i_a \\ i_b \\ i_c \\ i_d \\ i_e \\ i_f \end{matrix} \tag{2.11}$$

The first three terms in each row of the above matrixes relate to the first three phase winding set and the second three terms correspond to the parameters of the second three phase winding set.

The six phase time varying currents are decoupled into four currents in two isolated planes. The first plane in which the fundamental torque component is developed is called the $\alpha\beta$ plane. The flux interaction between the stator and the rotor is mainly done in this plane. The intermediate planes which only one of them exists in the case of six phase motor do not contribute to fundamental torque production and only create losses. The last plane represented by the last two rows in the Clark transformation matrix corresponds to zero sequence currents flowing between the neutrals.

Park transformation is used to alter these four parameters to the rotating components with the rotor so they do not change as the rotor spins. The Park transformation matrix is represented by:

$$\begin{bmatrix} cos\theta & sin\theta \\ -sin\theta & cos\theta \end{bmatrix} \tag{2.12}$$

where θ is the rotor instantaneous angle. This transformation converts the two phase $\alpha\beta$ components in the stationary reference frame into two phase dq components in the rotating reference frame as explained in (2.13) and (2.14).

$$I_d = I_\alpha cos\theta + I_\beta sin\theta \tag{2.13}$$

$$I_q = -I_\alpha sin\theta + I_\beta cos\theta \tag{2.14}$$

In the main control block diagram shown in Fig. 2.14, the current references are generated in the dq reference frame. The d axis current reference is always set to zero whereas the q axis current reference demonstrates the torque producing component of the current and is the output of the speed control loop.

The actual currents measured by the sensors are converted into $\alpha\beta xy$ subspaces and compared to the reference currents in the $\alpha\beta xy$ plane acquired by inverse Park transformation. In order to better regulate the six phase currents, the stationary reference frame currents are divided into clockwise rotating and counterclockwise rotating elements and separate proportional-integral (PI) controllers are augmented to adjust each of the errors. The outputs of the controllers are converted back into the actual *abcdef* frame as commands for the inverter switches in modulator forms. A sinusoidal PWM method is utilized in this work. It has to be mentioned that the rotor angle is provided by the encoder mounted on the shaft of the motor wherever required.

In addition to the inner current control loop, an outer speed control loop with much less band width and time constant is implemented to achieve the speed controllability, Fig. 2.15. A reference speed is commanded by the software and this loop tracks the reference by adaptively providing the proper current command in the q axis which will produce the required torque to increase or decrease the speed.

The anti-windup loop shown in red prevents the speed to rise tremendously [71]. The established q axis current reference is passed into a limiter. The upper and lower limits are selected such that the achieved speed with the maximum applied torque is within the acceptable range. The actual q axis current reference is compared to the output of the limiter and the generated error is added back to the actual speed error. Therefore, it is assured in this way that the current command is not increased suddenly by the loop.

The feed forward branch in conjunction with the anti-windup loop provides two degrees of freedom in adjusting the speed control loop. While the main loop tracks the fundamental component of torque and speed, the feedforward branch creates a secondary loop which removes one pole of the overall transfer function and hence reducing the speed overshoot during the transient as stated in [71].

Harmonic contents always exist in the system due to non-idealities which needs to be removed so that the output currents are of a low distortion. One method of diminishing harmonics is through harmonic component rejection scheme which is added to the main FOC as shown in Fig. 2.16.

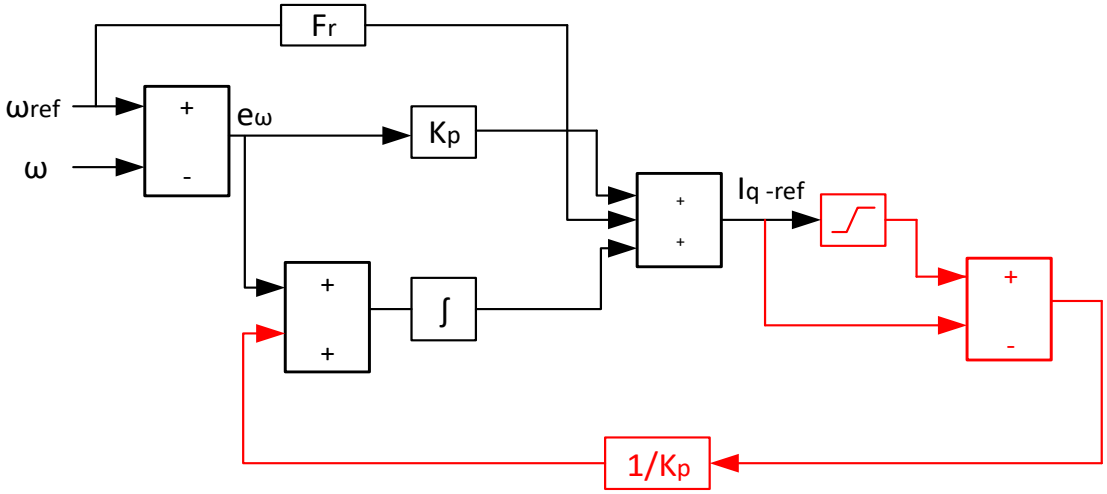

Fig. 2.15: Speed control loop of the FOC.

Harmonics of orders -5, +7, -11, +13 and etc are of the highest magnitude in a symmetrical six-phase system. Therefore, harmonics -5 and +7 is rejected in this system. In the block diagram below, ω, h, Θ_r and T refer to the fundamental frequency, harmonic order, instantaneous rotor angle and sampling period, respectively. The harmonic rejection loop exactly acts like the fundamental current control loop except for the rotating reference frames which are set at the desired harmonic speed and PI controllers tune the dc parameters. Afterwards, the cancelling component of the currents generated by the controller is injected by the inverters. The $2h\omega T$ term added to the angle in the inverse Park transformation takes into account one sampling period for computation time, half a sampling period for modulation delay and another half sampling period for current averaging. This helps the used angle in the transformation being closer to the actual angle.

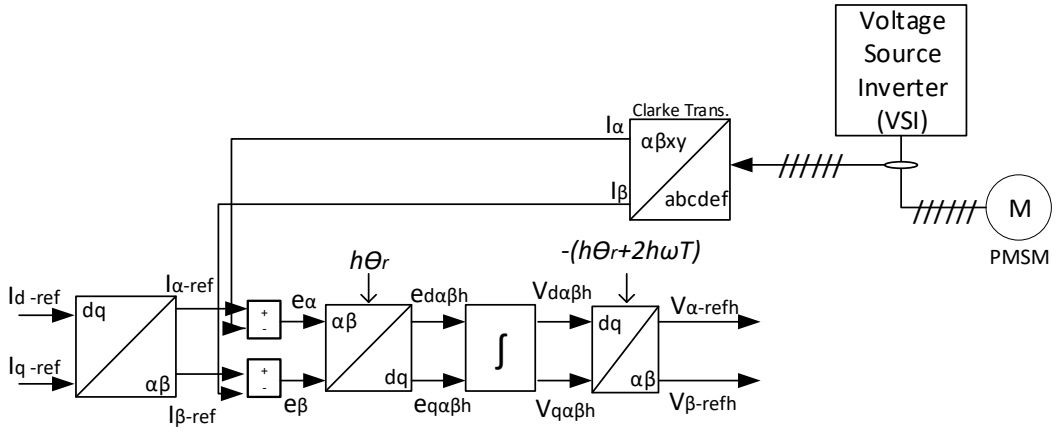

Fig. 2.16: Harmonic rejection scheme block diagram.

Another method of diminishing the harmonic contents is to virtually add an active resistance to change the poles and zeros associated with the aimed harmonics. It is proved in [72] that the active resistance in the first plane is directly proportional to the magnetizing inductance and the active resistance in the second plane is directly proportional to the leakage inductance of the stator windings.

In order to maximize the dc bus utilization, [73] proposes a method to optimally enhance the dc bus usage such that higher output voltages are achieved by the same dc bus level. It removes the zero sequence components as it will not flow in a system with isolated neutrals. Equations (2.15) and (2.16) represent the two key equations for zero sequence injection.

$$Zero_{sequence_{injection}} = -\frac{m_{max}+m_{min}}{2} \tag{2.15}$$

$$m_{new} = m_{old} + Zero_{sequence_{injection}} \tag{2.16}$$

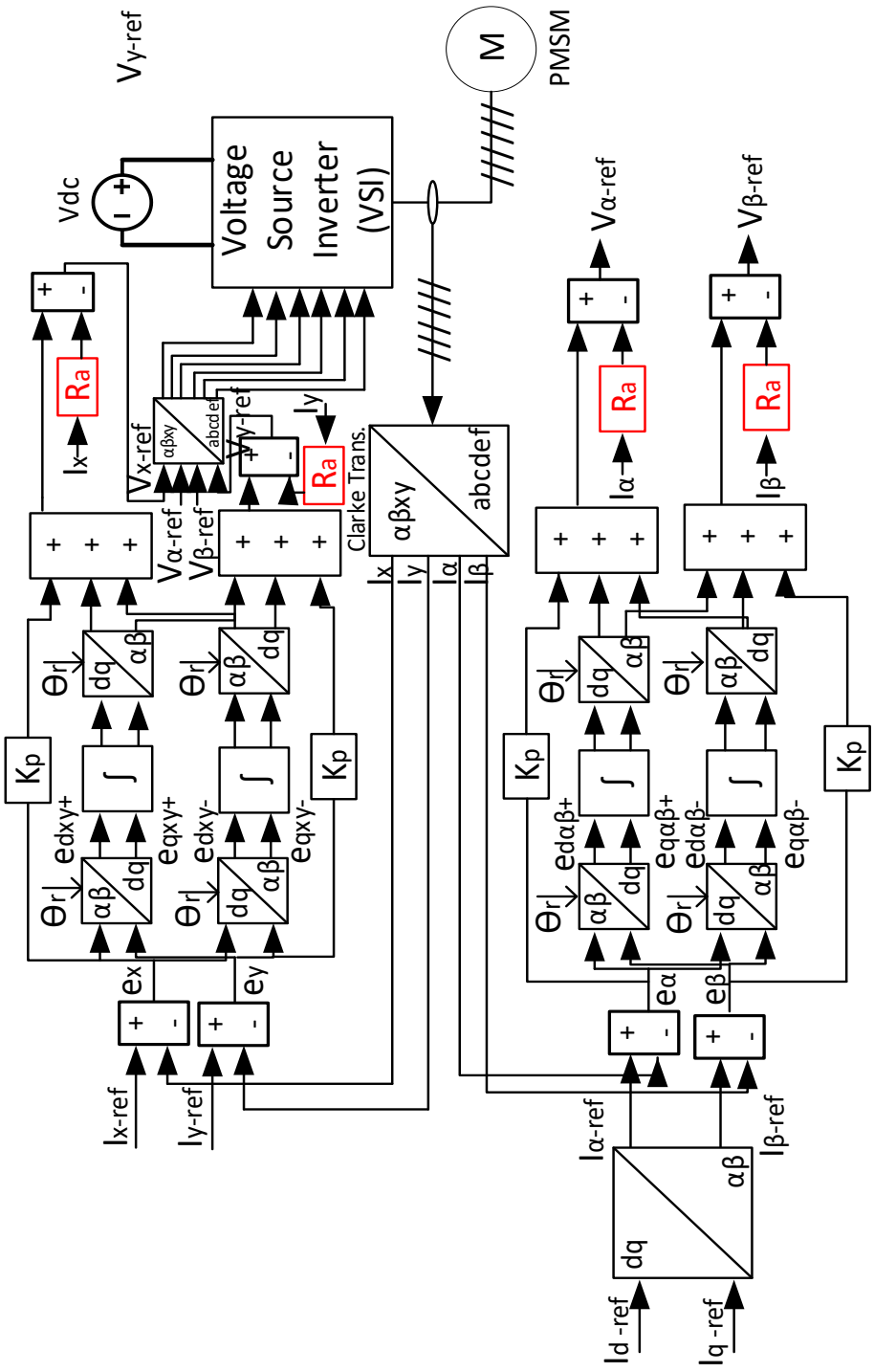

Fig. 2.17: Block diagram of active resistance scheme.

By removing the zero sequence injection parameter of the modulators at each sampling instance, it is guaranteed that the dc bus is not allocated to zero sequence injection.

The deadtimes in the inverters can potentially introduce harmonic voltages in the order of switching frequency in the system. Therefore, a compensating signal is added to the PWM modulators to offset the deadtime effects. The following equation describes the required signal to be added:

$$M^*_s = \widehat{M}_s + sign(i_s).t_d.f_{sw}.v_{dc} \tag{2.17}$$

Where M^*_s, $\widehat{M}_s$, i_s, t_d, f_{sw} and v_{dc} are the adjusted modulator signal, the reference modulator, the phase current, deadtime, switching frequency and the dc bus voltage. Depending on whether the current is flowing to the inverter or back to the dc bus, the corrective signals are added or subtracted from the modulators.

After implementing the above mentioned schemes in the drive, the general performance of the drive system was examined by tracking key parameters.

The inner control loop has to acceptably operate fast. A current command is asserted and the actual current response is captured. A settling time of 2 ms is recorded for the current control loop. The bandwidth of the current loop is set at 300 Hz.

The outer loop which operates relatively slower than the inner current loop is also evaluated. Speed step response is shown in Fig. 2.19 along with the three phase currents. 10% speed overshoot and 4s settling are believed to be acceptable. The bandwidth of the speed loop is set at 50 Hz.

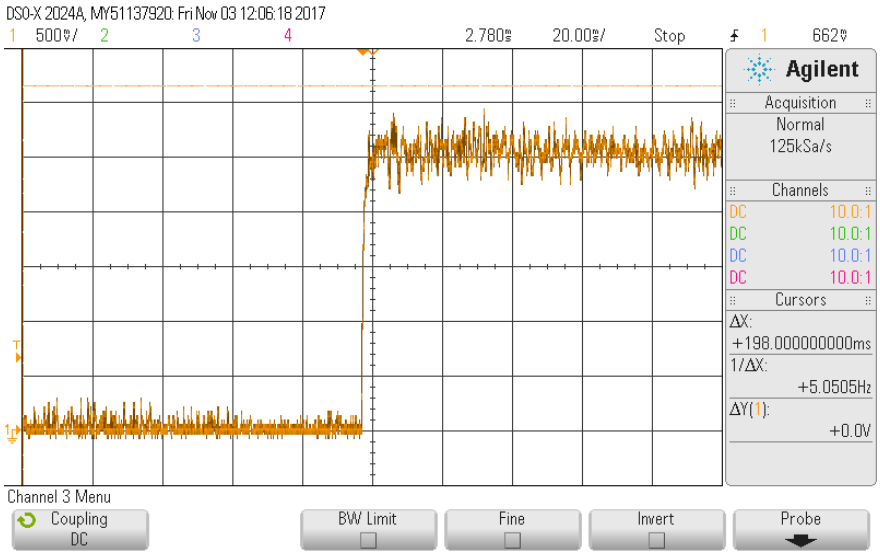

(a)

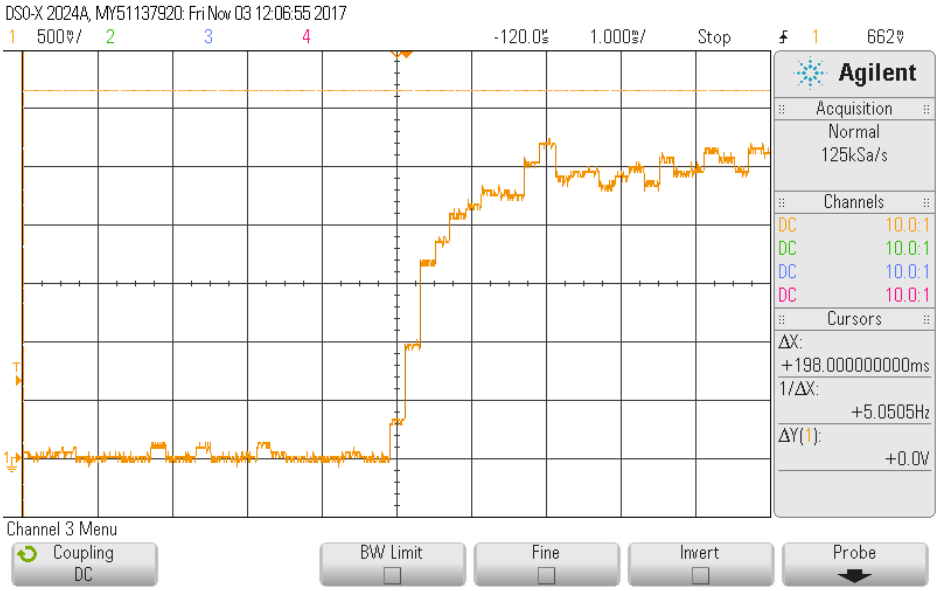

(b)

Fig. 2.18: Current step response, a) broad range and b) zoomed version.

As depicted in Fig. 2.20, operating with three active legs instead of six at light load enhances the converter and the overall efficiency, in spite of being less convenient in terms of copper losses. Namely in Fig. 2.20(c), the efficiency is increased up to 2.6%, which occurs at 0.145 p.u. output torque. The normalized torque values at which the number of active phases should be swapped is shifted to 0.188 p.u. in the SEOE [Fig. 2.20(c)] with respect to the SECE, in which it occurs at 0.33 p.u. [Fig. 2.20(a)]. For example, at 0.24 p.u. output torque, the SEOE offers an overall efficiency of 97.8% [Fig. 2.20(c)], whereas in the case of the SECE, which at 0.24 p.u. still tracks the blue curve (3 phases), the efficiency is 90%.

This shows at least 7.8% improvement in efficiency when comparing SECE and SEOE on the experimental prototype.

Next, an increase in the stator resistance is emulated by adding $0.3\,\Omega$ to each phase. Fig. 2.21(a) shows that, with the greater resistance, both the efficiency curve as a whole and the threshold torque value are reduced. Moreover, Fig. 2.21(b) demonstrates that the threshold torque and the efficiency in general become larger and lower, respectively, at higher switching frequencies.

Even though the numerical quantities are not exactly the same in the simulations (Section 2.2 and 2.3) and experiments (presumably due to parameter deviations from their ideal values), it can be seen that the general conclusions (concerning the fact that SEOE improves the efficiency with respect to SECE and to using all phases, and also the type of variation with R_s and f) match between both types of results.

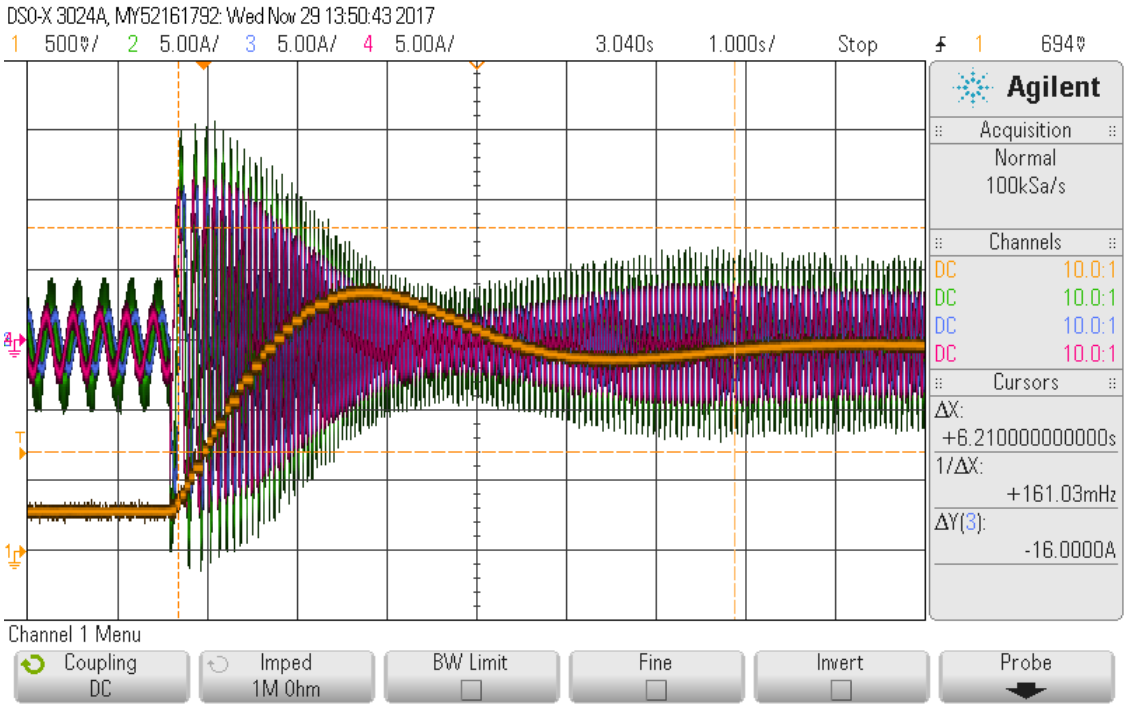

Fig. 2.19: Speed step response (shown in yellow).

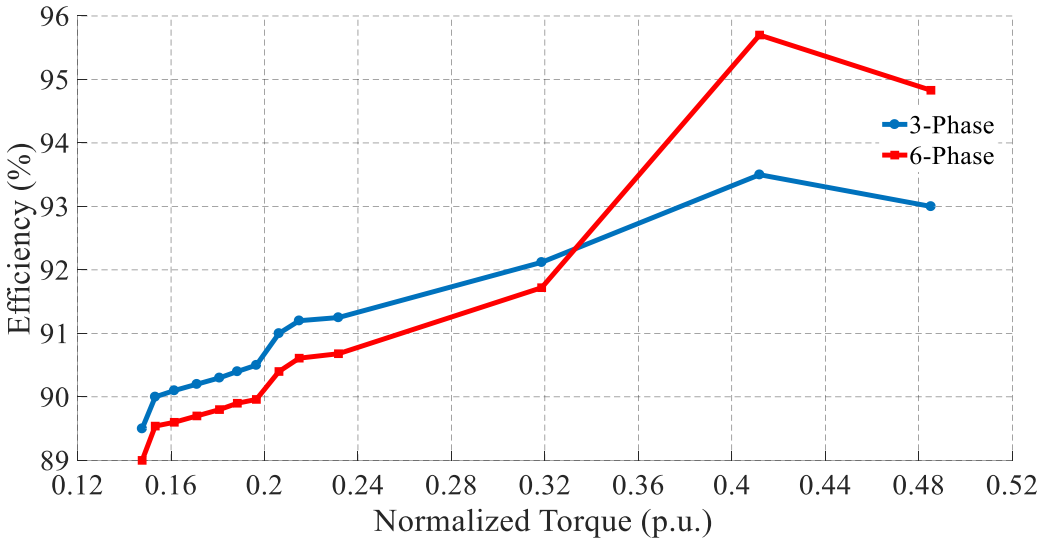

(a)

Fig. 2.20. Efficiency measurement of the actual prototype considering (a) only converter losses, (b) only copper losses, and (c) overall losses.

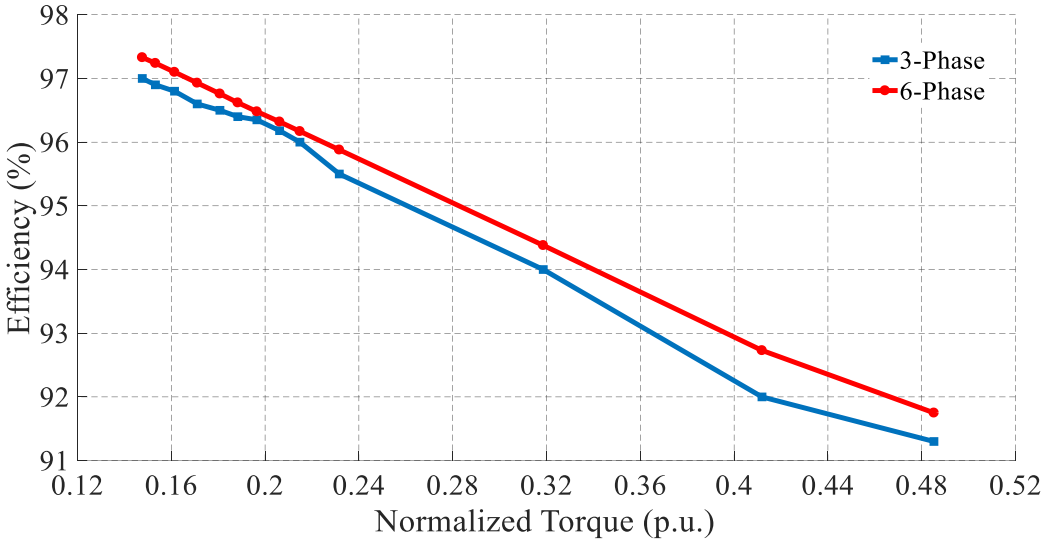

(b)

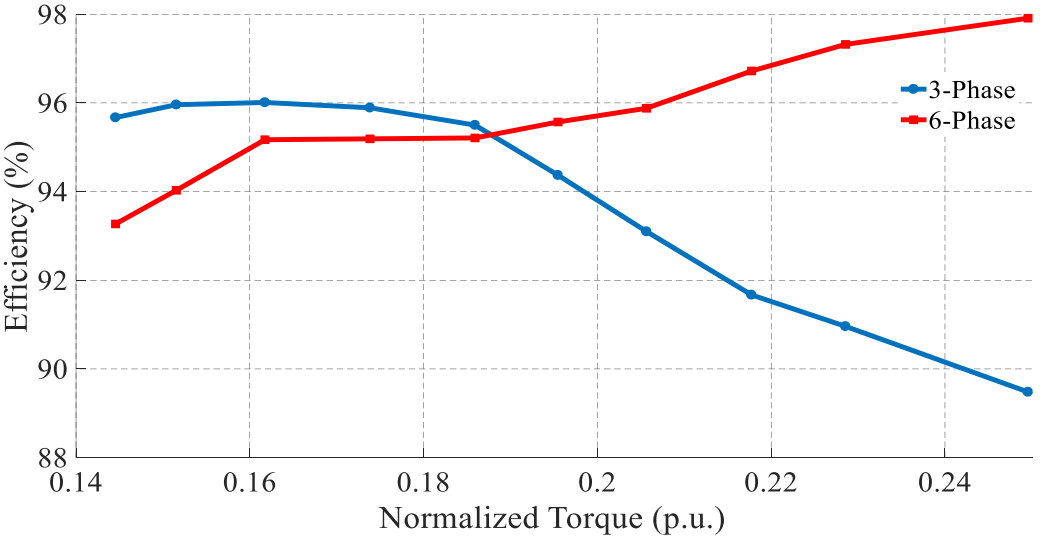

(c)

Fig. 2.20. Continued.

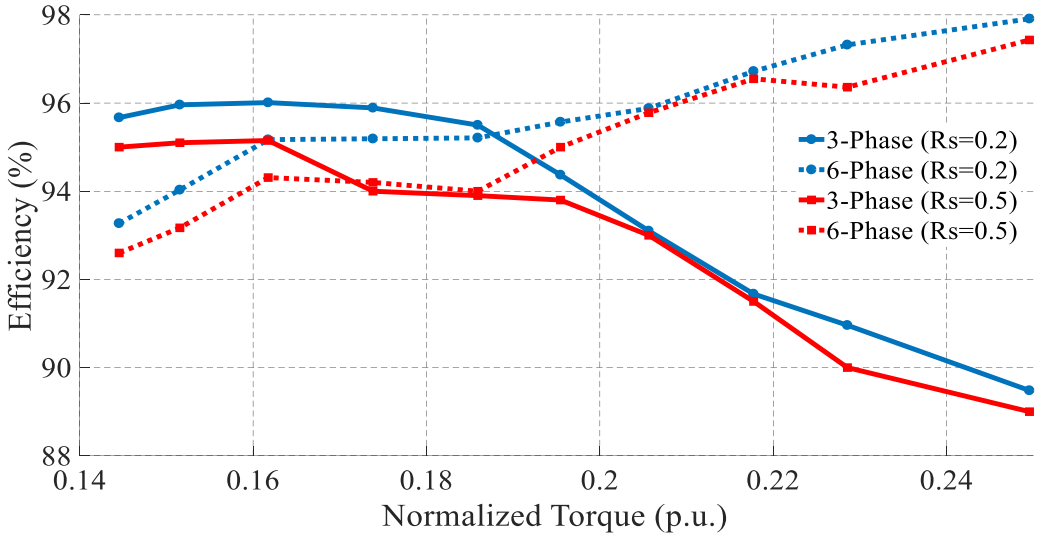

(a)

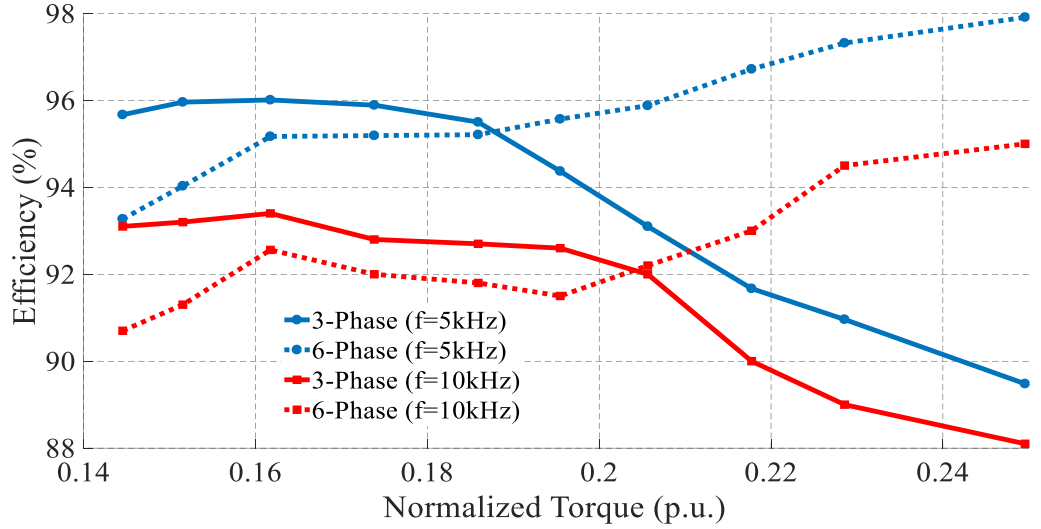

(b)

Fig. 2.21. Experimental comparison of the overall efficiency with the SEOE at (a) different stator resistances, and (b) different switching frequencies.

Lastly, Fig. 2.22 represents the transient behavior during the mode swapping. One phase current of each three-phase winding set (phases a1 and a2, in accordance with Fig. 2.1) is shown, along with the torque and speed waveforms. The magnitude of the

current references is automatically doubled in the DSP when the phase number is halved (Fig. 2.22 (a)), and vice versa (Fig. 2.22 (b)). There is a brief change in the torque when the mode commutation happens, presumably due to nonlinearities and to the differences in the converter and copper losses between modes. In any case, the control rapidly compensates this disturbance, and the speed is kept unaltered. If this short torque variation were inconvenient for a certain sensitive application, it could be reduced by taking into account those effects when recalculating the current references.

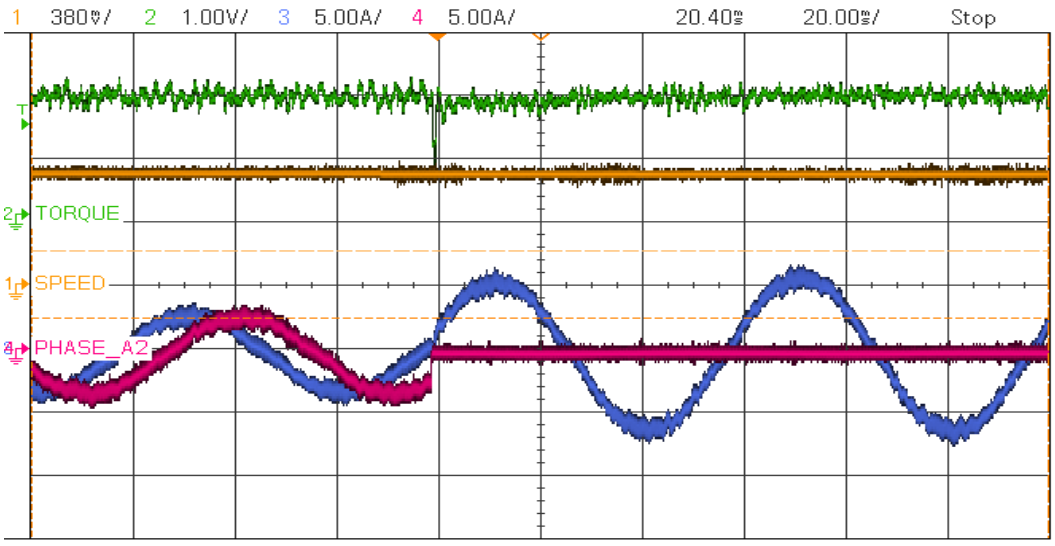

(a)

Fig. 2.22. Phase currents, speed and torque waveforms during the mode transition from (a) 6 to 3 phases, and from (b) 3 to 6 phases. The scale of the speed and torque is 400 rpm/div and 2 Nm/div, respectively.

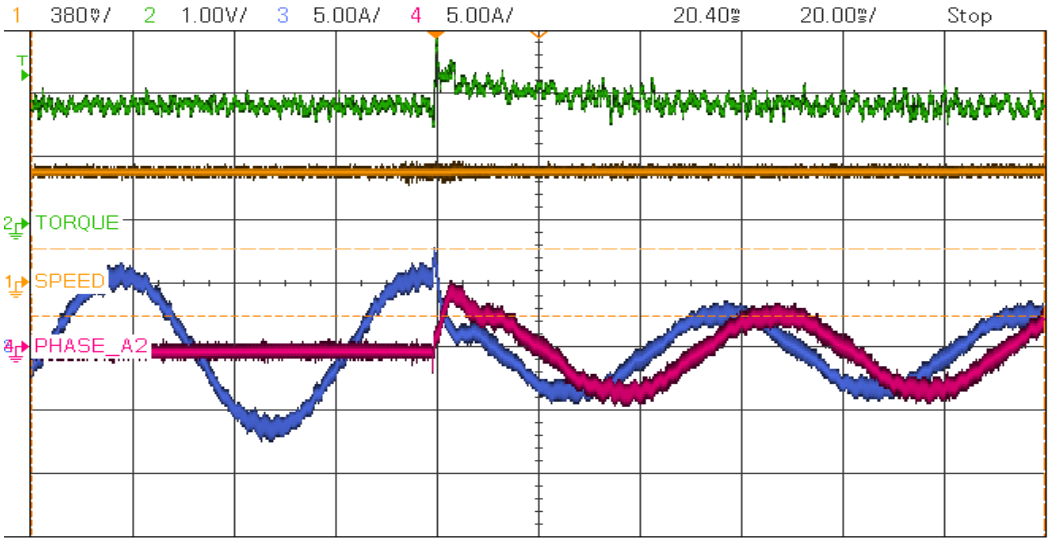

(b)

Fig. 2.22. Continued.

3. IMPROVED SENSORLESS DRIVE FOR SYNCHRONOUS MOTORS BASED ON HIGH-FREQUENCY SINUSOIDAL SIGNAL INJECTION WITH SIMPLIFIED EXTRACTION OF POSITION-ERROR INFORMATION

3.1. High-frequency Impedance Characteristic of the Surface-Mount Permanent Magnet Synchronous Motor (SPMSM)

Generally, a synchronous motor is modelled in the rotating reference frame by:

$$v_d = r_s i_d + L_s \frac{d}{dt} i_d + \omega_r (L_s i_q + K_e) \tag{3.1}$$

$$v_q = r_s i_q + L_s \frac{d}{dt} i_q - \omega_r L_s i_d \tag{3.2}$$

where v_d, v_q, i_d, i_q, r_s, L_s, ω_r and K_e represent *d*-axis rotor voltage, *q*-axis rotor voltage, *d*-axis rotor current, *q*-axis rotor current, stator winding resistance, stator winding magnetizing inductance, rotor angular velocity and back-EMF constant, respectively.

Given a *dq* synchronous reference frame rotating so that *d* is aligned with the rotor flux, the high-frequency equivalent circuit of the SPMSM can be expressed as

$$v_{dh} = r_{dh} i_{dh} + L_{dh} \frac{d}{dt} i_{dh} \tag{3.3}$$

$$v_{qh} = r_{qh} i_{qh} + L_{qh} \frac{d}{dt} i_{qh} \tag{3.4}$$

where v_{dh}, v_{qh}, r_{dh}, r_{qh}, L_{dh}, L_{qh}, i_{dh} and i_{qh} are the *d*-axis high frequency voltage, *q*-axis high frequency voltage, *d*-axis high frequency resistance, *q*-axis high frequency resistance, *d*-axis high frequency inductance, *q*-axis high frequency inductance, d-axis high frequency current and q-axis high frequency current, respectively. The above equations represent the motor considering only the high frequency injected signals.

Now, we assume the steady state condition to further simplify (3.3) and (3.4):

$$v_{dh} = (r_{dh} + j\omega_h L_{dh}) i_{dh} \tag{3.5}$$

$$v_{dh} = (r_{dh} + j\omega_h L_{dh}) i_{dh} \tag{3.6}$$

The equation (3.5) and (3.6) can be further simplified into:

$$v_{dh} = Z_{dh} i_{dh} \tag{3.7}$$

$$v_{qh} = Z_{qh} i_{qh} \tag{3.8}$$

where Z_{dh} and Z_{qh} are *d*-axis high frequency impedance and *q*-axis high frequency impedance.

Let us define the rotor angle estimation error by

$$\tilde{\theta}_r = \theta_r - \hat{\theta}_r \tag{3.9}$$

with $\tilde{\theta}_r$ being the rotor angle estimation error, θ_r the actual rotor angle and $\hat{\theta}_r$ the estimated rotor angle.

A matrix representation is used to express (3.7) and (3.8):

$$\begin{bmatrix} v_{dh} \\ v_{qh} \end{bmatrix} = \begin{bmatrix} Z_{dh} & 0 \\ 0 & Z_{qh} \end{bmatrix} \begin{bmatrix} i_{dh} \\ i_{qh} \end{bmatrix} \tag{3.10}$$

By multiplying both sides of (3.10) by the inverse high frequency impedance matrix, (3.11) is obtained:

$$\begin{bmatrix} i_{dh} \\ i_{qh} \end{bmatrix} = \begin{bmatrix} Z_{dh} & 0 \\ 0 & Z_{qh} \end{bmatrix}^{-1} \begin{bmatrix} v_{dh} \\ v_{qh} \end{bmatrix} = \begin{bmatrix} \frac{1}{Z_{dh}} & 0 \\ 0 & \frac{1}{Z_{qh}} \end{bmatrix} \begin{bmatrix} v_{dh} \\ v_{qh} \end{bmatrix} \tag{3.11}$$

On the other hand, it is shown below that the variables in the actual synchronous reference frame and the estimated synchronous frame are related to each other by:

$$\begin{bmatrix} X_d \\ X_q \end{bmatrix} = \begin{bmatrix} cos\tilde{\theta}_r & sin\tilde{\theta}_r \\ -sin\tilde{\theta}_r & cos\tilde{\theta}_r \end{bmatrix} \begin{bmatrix} \hat{X}_d \\ \hat{X}_q \end{bmatrix} \tag{3.12}$$

$$\begin{bmatrix} \hat{X}_d \\ \hat{X}_q \end{bmatrix} = \begin{bmatrix} cos\tilde{\theta}_r & -sin\tilde{\theta}_r \\ sin\tilde{\theta}_r & cos\tilde{\theta}_r \end{bmatrix} \begin{bmatrix} X_d \\ X_q \end{bmatrix} \tag{3.13}$$

If the high frequency voltages are injected through the estimated reference frames, based on (3.12) and (3.13), induced high frequency currents along the estimated reference frames are calculated by:

$$\begin{bmatrix} \hat{\imath}_{dh} \\ \hat{\imath}_{qh} \end{bmatrix} = \begin{bmatrix} cos\tilde{\theta}_r & -sin\tilde{\theta}_r \\ sin\tilde{\theta}_r & cos\tilde{\theta}_r \end{bmatrix} \begin{bmatrix} i_{dh} \\ i_{qh} \end{bmatrix}$$

$$= \begin{bmatrix} cos\tilde{\theta}_r & -sin\tilde{\theta}_r \\ sin\tilde{\theta}_r & cos\tilde{\theta}_r \end{bmatrix} \begin{bmatrix} \frac{1}{Z_{dh}} & 0 \\ 0 & \frac{1}{Z_{qh}} \end{bmatrix} \begin{bmatrix} v_{dh} \\ v_{qh} \end{bmatrix}$$

$$= \begin{bmatrix} cos\tilde{\theta}_r & -sin\tilde{\theta}_r \\ sin\tilde{\theta}_r & cos\tilde{\theta}_r \end{bmatrix} \begin{bmatrix} \frac{1}{Z_{dh}} & 0 \\ 0 & \frac{1}{Z_{qh}} \end{bmatrix} \begin{bmatrix} cos\tilde{\theta}_r & sin\tilde{\theta}_r \\ -sin\tilde{\theta}_r & cos\tilde{\theta}_r \end{bmatrix} \begin{bmatrix} \hat{v}_{dh} \\ \hat{v}_{qh} \end{bmatrix} \tag{3.14}$$

where $\hat{v}_{dh}$, $\hat{v}_{qh}$, $\hat{\imath}_{dh}$, $\hat{\imath}_{qh}$ are the high frequency voltage along the estimated *d*-axis, high frequency voltage along the estimated *q*-axis, high frequency current along the estimated *d*-axis and the high frequency current along the estimated *q*-axis, respectively.

The induced high frequency currents along the *d* and *q*-axis can be rewritten as:

$$\hat{\imath}_{dh} = \frac{1}{Z_{dh}Z_{qh}} \left[\left(Z_{avg} - \frac{1}{2} Z_{diff} cos2\tilde{\theta}_r \right) \hat{v}_{dh} - \left(\frac{1}{2} Z_{diff} sin2\tilde{\theta}_r \right) \hat{v}_{qh} \right] \tag{3.15}$$

$$\hat{\imath}_{qh} = \frac{1}{Z_{dh}Z_{qh}} \left[\left(-\frac{1}{2} Z_{diff} sin2\tilde{\theta}_r \right) \hat{v}_{dh} + \left(Z_{avg} + \frac{1}{2} Z_{diff} sin2\tilde{\theta}_r \right) \hat{v}_{qh} \right] \tag{3.16}$$

where

$$Z_{avg} = \frac{Z_{dh} + Z_{qh}}{2} \tag{3.17}$$

$$Z_{diff} = Z_{dh} - Z_{qh} \tag{3.18}$$

Z_{avg} and Z_{diff} are the average of *d* and *q*-axis high frequency impedance and difference of *d* and *q*-axis high frequency impedance, respectively.

Based on (3.15) and (3.16), it is decided to which axis of the estimated reference frame the high frequency signal should be injected. In this case, the fluctuating voltage can be injected both in the *d* and *q* axis of the estimated reference frame. For example, if the high frequency voltage is injected along the *d*-axis:

$$\hat{v}_{dh} = V_{inj} cos\omega_h t \tag{3.19}$$

$$\hat{v}_{qh} = 0 \tag{3.20}$$

where V_{inj} and ω_h are the magnitude of the injected voltage and the angular speed of the high frequency voltage.

Equations (3.15) and (3.16) can be rewritten by plugging (3.19) and (3.20) in them:

$$\hat{\imath}_{dh} = \frac{V_{inj} cos\omega_h t}{Z_{dh} Z_{qh}} \left(Z_{avg} - \frac{1}{2} Z_{diff} cos2\tilde{\theta}_r\right) \tag{3.21}$$

$$\hat{\imath}_{qh} = \frac{V_{inj} cos\omega_h t}{Z_{dh} Z_{qh}} \left(-\frac{1}{2} Z_{diff} sin2\tilde{\theta}_r\right) \tag{3.22}$$

It is inferred that the high frequency current induced along the *d*-axis of the estimated reference frame is proportional to a dc value added to the cosine of the rotor angle estimation error whereas the high frequency current induced along the *q*-axis of the estimated reference frame is proportional to the sine of the rotor angle estimation error. Therefore, it is more proper to measure the high frequency current induced along the *q*-axis of the estimated reference frame as it is directly proportional to the rotor angle estimation error. It also has to be mentioned that this current includes the rotor angle

information provided that the difference in the high frequency impedance of the *d* and *q* axes are fairly large.

In order to evaluate the high frequency impedance characteristics of the studied machine, a measurement reference frame is attached to the rotor so as it rotates, various rotor positions are covered as shown in Fig. 3.1. d_{meas}, q_{meas}, *d*, *q* and α are the *d*-axis of the measurement reference frame, *q*-axis of the measurement reference frame, actual *d*-axis, actual *q*-axis and the relative angle between the actual and measurement axes.

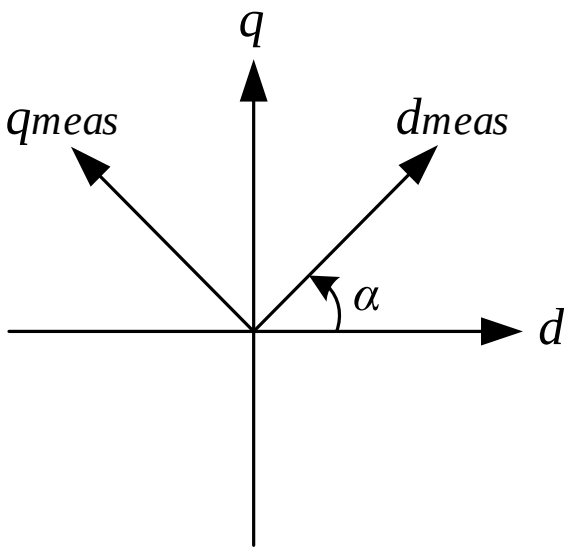

Fig. 3.1: Measurement and the actual reference frame for high frequency impedance measurement.

The following plots demonstrate the high-frequency impedance characteristic of the studied SPMSM at different voltages and frequencies. The relative position of the actual rotor reference frame with respect to the measurement reference frame is swept in steps of 30 degrees and the associated high-frequency impedance is experimentally calculated by 3.23.

$$Z_d = \frac{V_{d,meas}}{I_{d,meas}} \tag{3.23}$$

where Z_d represents the impedance along the d-axis of the measurement reference frame. Now as the measurement frame rotates, Z_d plots a sinusoidal curve. The minimum points of Z_d correspond to *d*-axis high frequency impedance since the injected currents along with the permanent magnet fluxes will saturate the iron along this path. In contrast, the peak points of this curve correspond to *q*-axis impedance. Since the tests have been implemented in discrete angles, the ideal sinusoidal profile of the high frequency impedance cannot be seen.

The lowest impedance corresponds to the actual *d* axis, which is aligned with the magnets. On the other hand, the impedance increases as the frequency is higher. At a certain frequency, the *q* axis high frequency impedance is decreased as the magnitude of the injected voltage is increased but the *d* axis high frequency impedance is not varied. This is due to *d* axis already being saturated and possessing the least impedance. Based on Fig. 3.2(a) and 3.2(b) the 40 V, 500 Hz high-frequency voltage is chosen as the most suitable injected voltage, which results in 5.9 Ω of high-frequency impedance difference along the *d* and *q* axes. This difference makes it possible to obtain information about the rotor position angle through (3.22). The injected frequencies of around ten times of the fundamental frequency is found to be proper. It should be mentioned that the high frequency voltage is injected in the αβ plane.

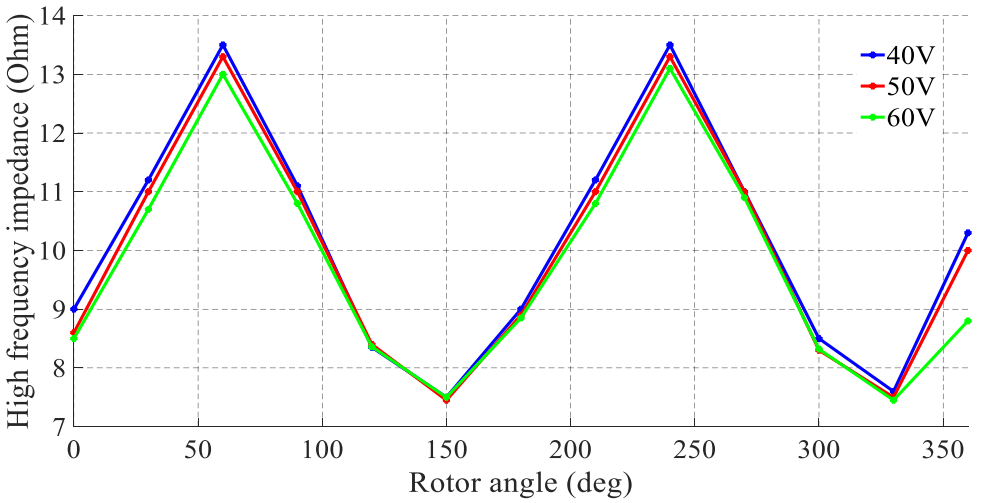

(a)

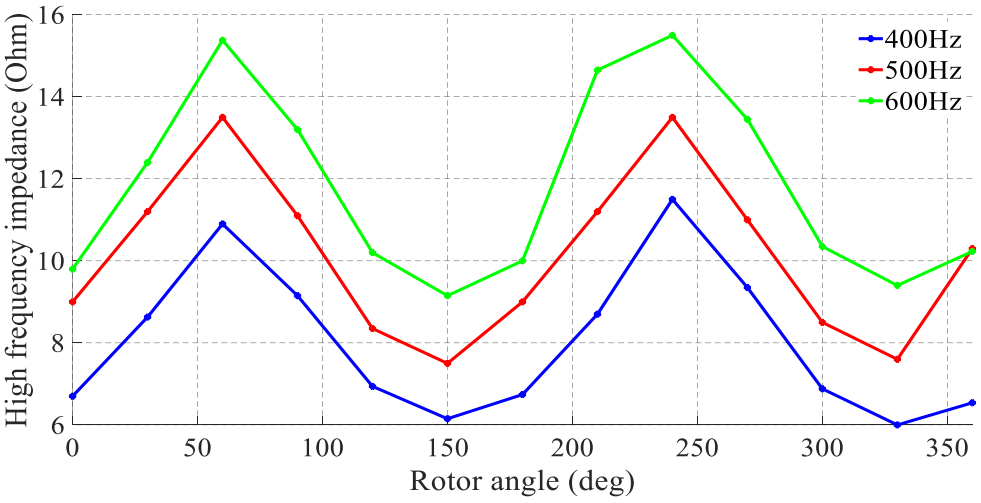

(b)

Fig. 3.2: High-frequency impedance characteristic of the SPMSM versus mechanical rotor angle at a) different magnitude of the injected voltages of 500 Hz frequency, b) different frequency of the injected voltages of 40 V magnitude.

The asymmetrical six phase motor possesses two other control planes which can be used for injection. The zero sequence plane does not carry any current since the neutrals of

the two three phase winding sets are not connected to each other. However, the *xy* plane can be utilized for high frequency voltage injection. The high frequency impedances in the *xy* plane was also measured to investigate the possibility of injecting through this plane. Since the second plane has less impedance compared to the fundamental plane, less voltage is required to build up the required current. In this sense, a 20 V, 500 Hz voltage is injected along the *x* axis of the second plane and the high frequency impedance is measured as depicted in Fig. 3.3. The high frequency impedance difference along the *x* and *y* axis in the second plane is approximated to be 0.25 Ω which is very smaller than the first plane. Therefore, high frequency injection in the *xy* planes for rotor position estimation does not yield acceptable performance.

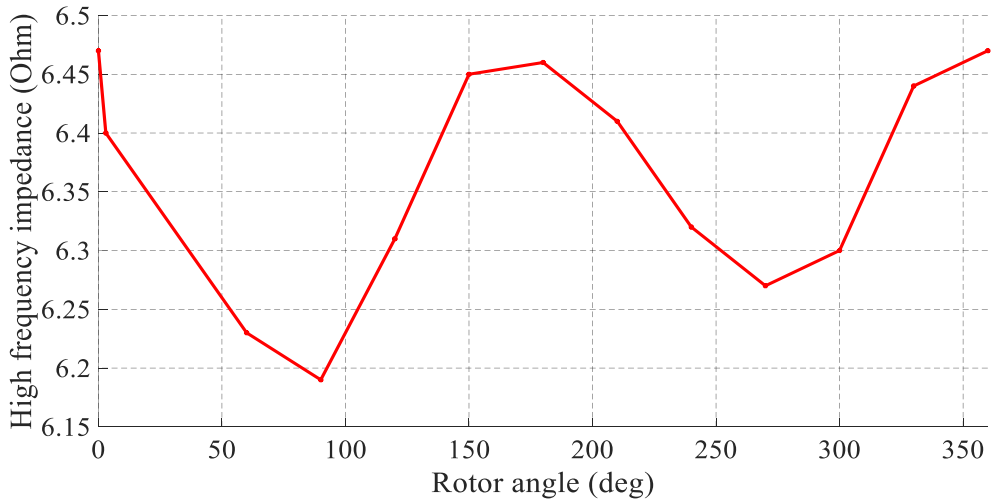

Fig. 3.3: High-frequency impedance characteristic of the SPMSM versus mechanical rotor angle at 20 V, 500 Hz high frequency sinusoidal voltage injection in the *x* axis.

At the ranges of the high frequencies injected, the high frequency impedances are mostly composed of inductive terms rather than resistive. As a result, the following deduction is valid:

$$Z_{dh} = r_{dh} + \mathrm{j}\omega_h L_{dh} \sim \mathrm{j}\omega_h L_{dh} \tag{3.24}$$

$$Z_{qh} = r_{qh} + \mathrm{j}\omega_h L_{qh} \sim \mathrm{j}\omega_h L_{qh} \tag{3.25}$$

With the above assumptions, (3.22) can be further simplified into:

$$\hat{\imath}_{qh} = \frac{V_{inj} sin2\tilde{\theta}_r}{2{\omega_h}^2 L_{dh} L_{qh}} (r_{diff} cos\omega_h t - \omega_h L_{diff} sin\omega_h t) \tag{3.26}$$

where r_{diff} and L_{diff} are the resistance difference between the high frequency *d* and *q* axis and inductance difference between the high frequency *d* and *q* axis, respectively.

In order to extract from (3.26) information about the rotor position error, the following operation is performed:

$$i_{\tilde{\theta}_r} = \mathrm{LPF}\left(\hat{\imath}_{qh} sin\omega_h t\right) = -\frac{V_{inj} L_{diff}}{4\omega_h L_{dh} L_{qh}} \sin 2\tilde{\theta}_r \tag{3.27}$$

where *LPF* stands for low pass filter. If the rotor position estimation error is small enough, (3.27) can be further simplified by

$$i_{\tilde{\theta}_r} = -\frac{V_{inj} L_{diff}}{2\omega_h L_{dh} L_{qh}} \tilde{\theta}_r \tag{3.28}$$

which explicitly illustrates the relation between this variable and the rotor position estimation error. Given such relation, this signal is adopted as the input to the rotor position estimator.

3.2. Proposed Improved Sensorless Scheme

Fig. 3.4 depicts the block-diagram representation of the $i_{\tilde{\theta}_r}$extraction proposed as also expressed in the previously derived equations. The transformation of the measured stator currents to the rotating reference frame is performed by using the estimated rotor position angle. Afterwards, $\hat{\imath}_{qh}$is extracted by applying a band-pass filter (BPF) to the overall q-axis current. Finally, in accordance with (3.27), the error signal $i_{\tilde{\theta}_r}$ is calculated by multiplying $\hat{\imath}_{qh}$by a $sin\omega_h t$ term and passing it through an LPF.

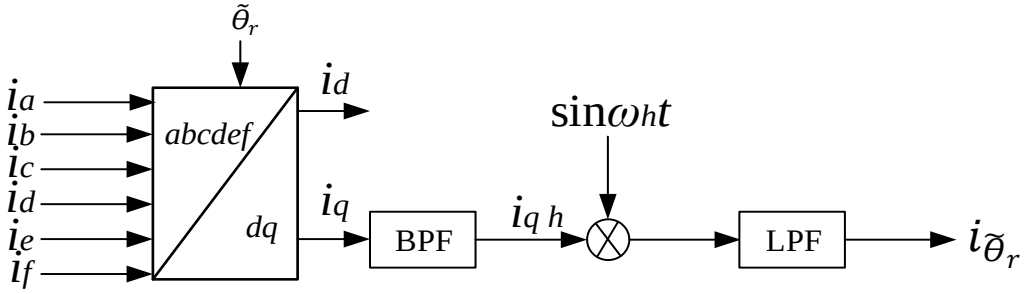

Fig. 3.4: Calculation of the error signal.

The BPF in Fig 3.4 can be digitally implemented as indicated by the red dashed square in Fig. 3.5 [68].

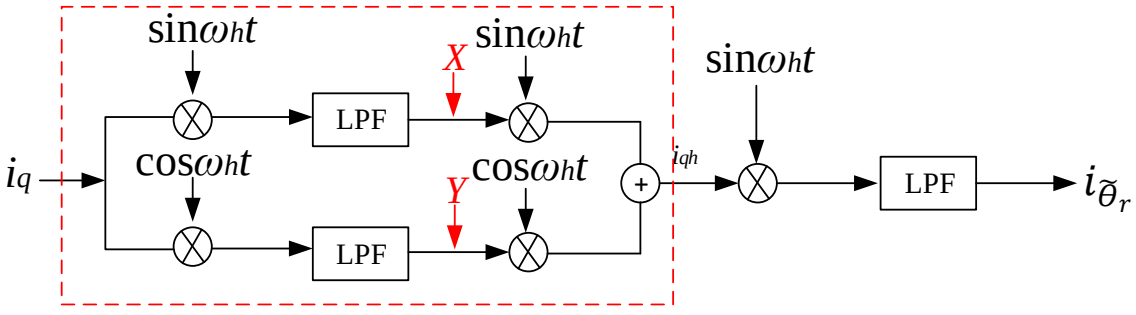

Fig. 3.5: Digital implementation of the BPF (shown in the red box) in conjunction with the error signal calculation.

The intermediate signals *X* and *Y* defined in Fig. 3.5 are obtained by

$$X = \text{LPF}(i_q \sin\omega_h t) \tag{3.29}$$

$$Y = \text{LPF}(i_q \cos\omega_h t) \tag{3.30}$$

And hence,

$$\hat{\imath}_{qh} = X\sin\omega_h t + Y\cos\omega_h t \tag{3.31}$$

$$i_{\tilde{\theta}_r} = \text{LPF}\big((X\sin\omega_h t + Y\cos\omega_h t) * \sin\omega_h t\big) = \text{LPF}(X\sin^2\omega_h t + Y\sin\omega_h t\cos\omega_h t) = \text{LPF}(\tfrac{1}{2}X) \tag{3.32}$$

Therefore, the scheme of Fig. 3.4 can be simplified as shown in Fig. 3.6.

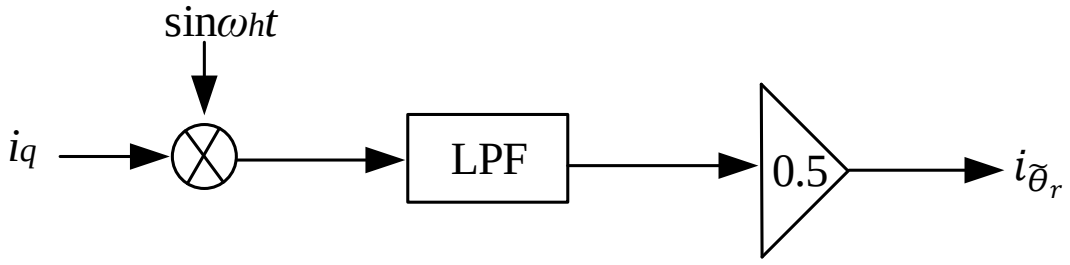

Fig. 3.6: Simplified method of $i_{\tilde{\theta}_r}$calculation.

Consequently, the new approach of $i_{\tilde{\theta}_r}$calculation removes two LPFs of the previous approach (Fig. 3.5), which in practice allows a faster response of the sensorless scheme. Moreover, three multiplications, the calculation of a cosine function, and one addition, are also saved. This further simplifies the implementation and provides extra execution time that the digital signal processor (DSP) can employ for other purposes.

The calculated $i_{\tilde{\theta}_r}$has to be controlled to mitigate the errors in the rotor position estimation. A bang-bang controller is utilized, as shown in Fig. 3.7, to adjust in closed-loop the estimated rotor angle such that the error is minimized [57].

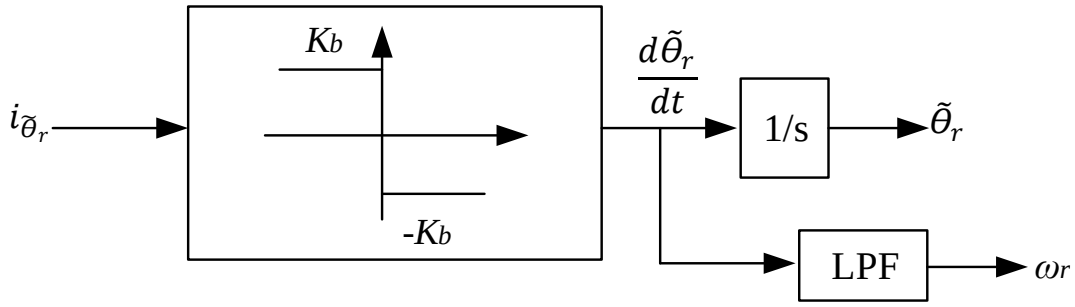

Fig. 3.7: Block diagram for estimating the rotor angle and the speed.

The controller generates the time derivative of the estimated rotor angle. An LPF is used to filter the noise and provide the estimated rotor speed. The bang-bang controller gain and the LPFs bandwidth are selected such that the overall estimation speed is compatible. For instance, if the controller gain is set very high such that the LPFs cannot keep up with the speed corrections of the sensorless algorithm, the estimation will diverge from the actual value. Moreover, if the bandwidth of the LPFs are set very narrow, the estimation scheme's dynamics will be too slow to update the current position of the rotor.

3.3. Experimental Results

The proposed sensorless scheme was tested in the experimental setup shown in Fig. 3.8. An originally 24 phase synchronous motor with external access to coil terminals as shown in Fig. 3.9 was rewound to obtain an asymmetrical six-phase synchronous motor. The back-EMF waveform of the 24 phase motor was used to determine the proper configuration to yield the asymmetrical six-phase winding as depicted in Fig. 3.10. The six-phase SPMSM is driven by field-oriented control using Semikron inverters. Note that, since only the flux/torque producing plane [69] is

employed in the tests, no substantial differences could be expected for other phase numbers. A Texas Instruments Delfino TMS320F28379 DSP is used for the control implementation. Table 3.1 illustrates some parameters of the setup. The bandwidth of the speed LPF has to be relatively low to achieve an accurate speed estimation. A bandwidth of 2 rad/s was chosen in this work. For the rightmost LPF in Fig. 3.4, a bandwidth of 200 rad/s was found to be convenient, and for those contained in the BPF in Fig. 3.4, a bandwidth of 2000 rad/s was set.

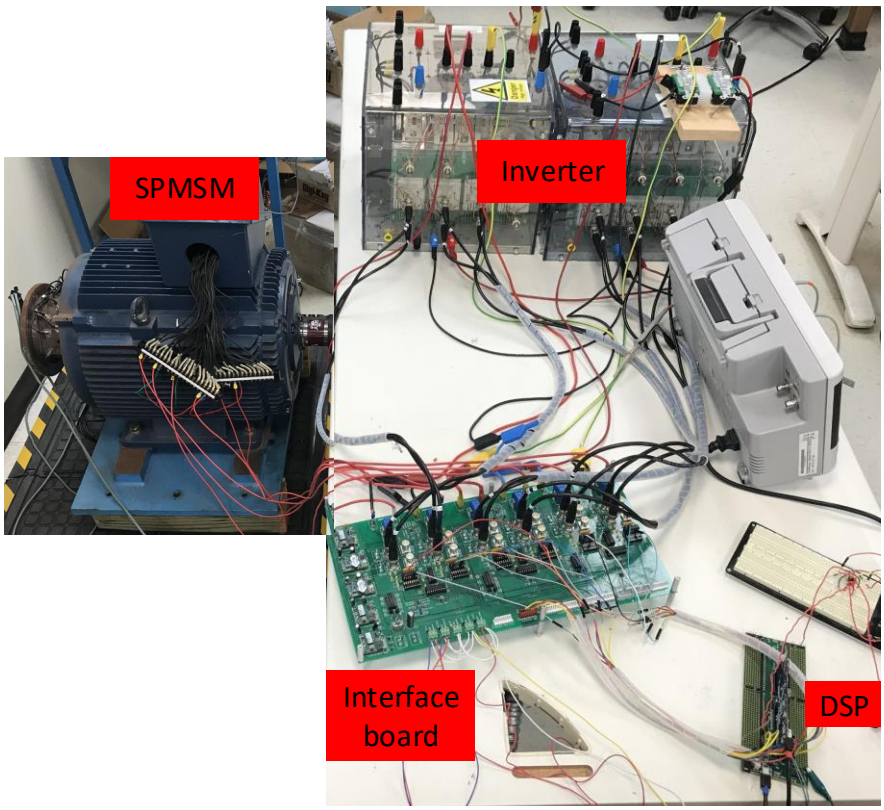

Fig. 3.8: Experimental prototype.

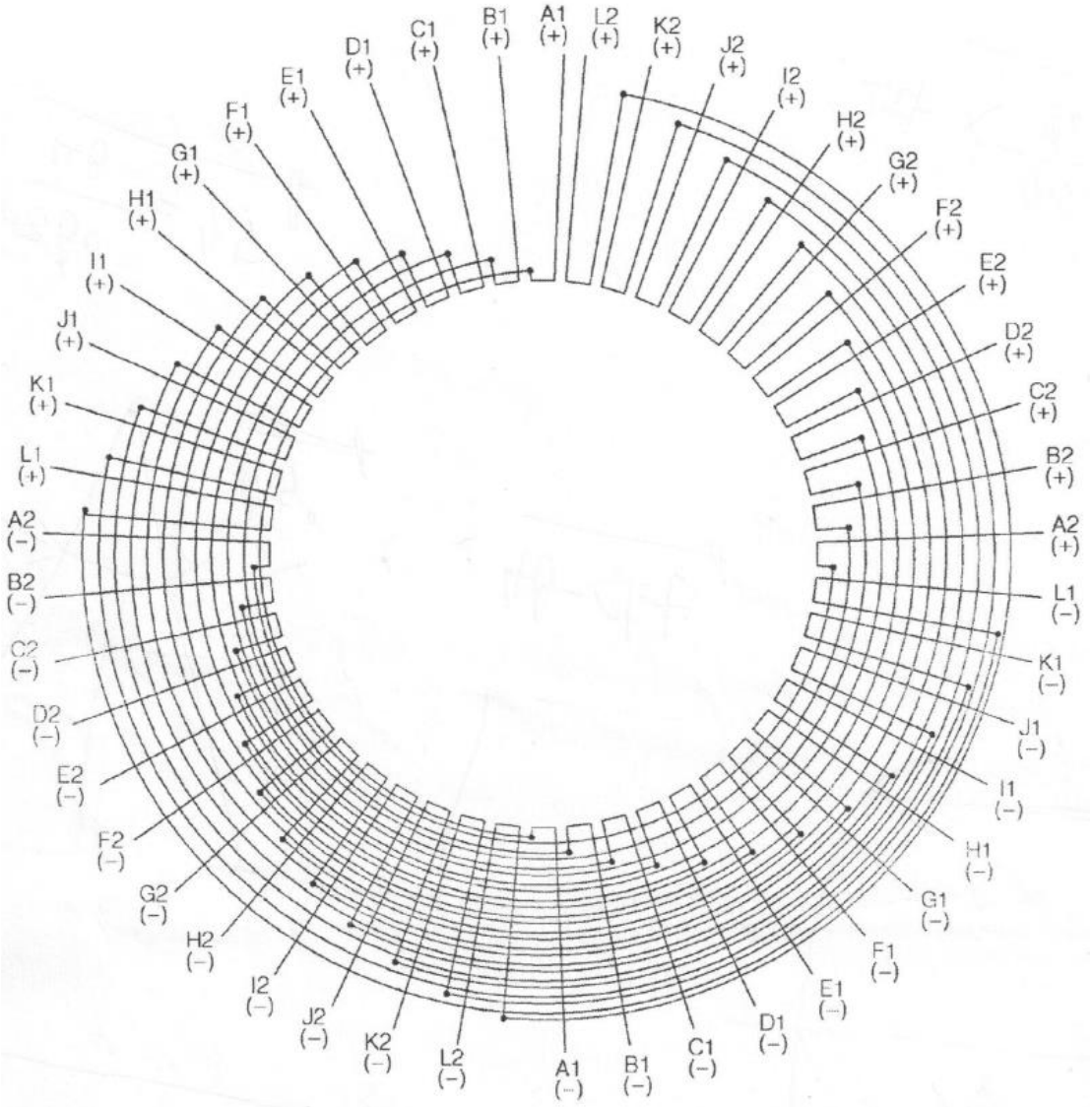

Fig. 3.9: Winding connections of the original 24-phase SPMSM.

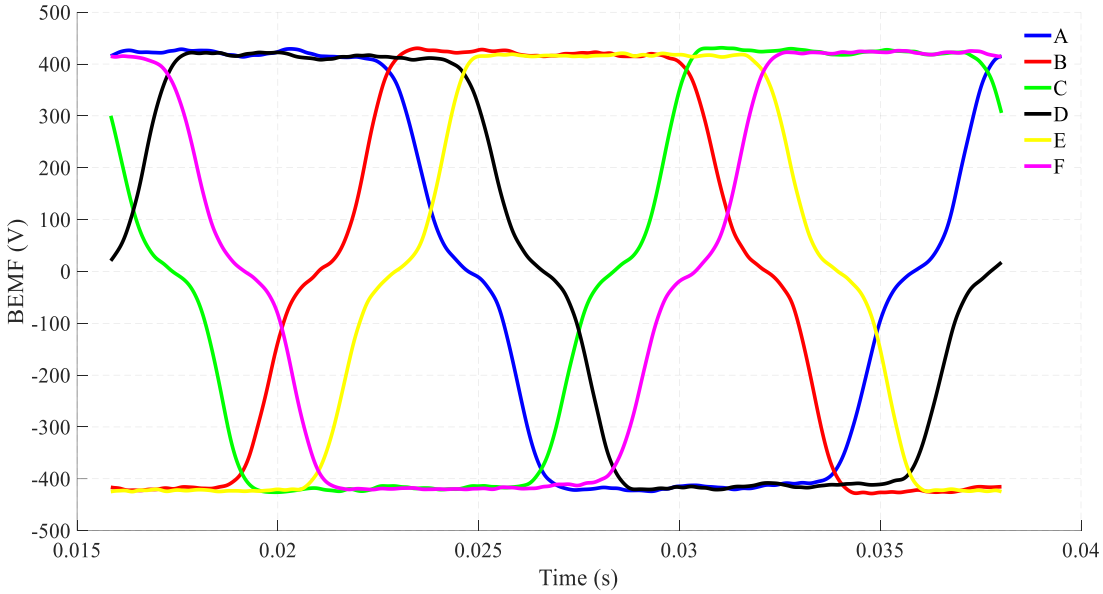

Fig. 3.10: Six-phase back-EMF waveforms of the motor shown in one full period.

Table 3.1

Experimental Setup Characteristics

Parameter	**Value**
Rated power	60 kW
Rated speed	1800 rpm
Number of poles	4
Stator winding resistance	0.47 Ω
Stator self-inductance	3 mH
Switching frequency	5 kHz
Sampling frequency	200 kHz

The motor is driven at 75 and 100 rpm by the proposed improved scheme and the estimated rotor electrical angle is compared in Fig. 3.11 (a) and (b) to the actual angle captured by an Allen Bradley encoder mounted on the shaft. Both angles match each other, which emphasizes the accuracy of the proposed scheme. An error of 0.9 % was detected in rotor angle estimation.

In the following, the transient behavior of the improved sensorless scheme is shown in Fig. 3.12 when altering the speed from 75 to 0 rpm. To study the effect on the current closed-loop without other uncertainties, the drive is set in torque (current) control mode and the speed changes are caused by step torque commands. To facilitate the inspection of the speed settling time, a virtual step speed command is shown in the captures along with the actual speed. Such signal rises at the instant when the torque command is applied, and its value matches the steady-state speed.

The input error signal $i_{\tilde{\theta}_r}$ gets affected in steady state by the scheme as well. For instance, the smaller amount of operations in the proposed scheme leads to a less oscillatory error signal as shown in Fig. 3.13. More stable input to the rotor angle estimator itself results in faster dynamic response.

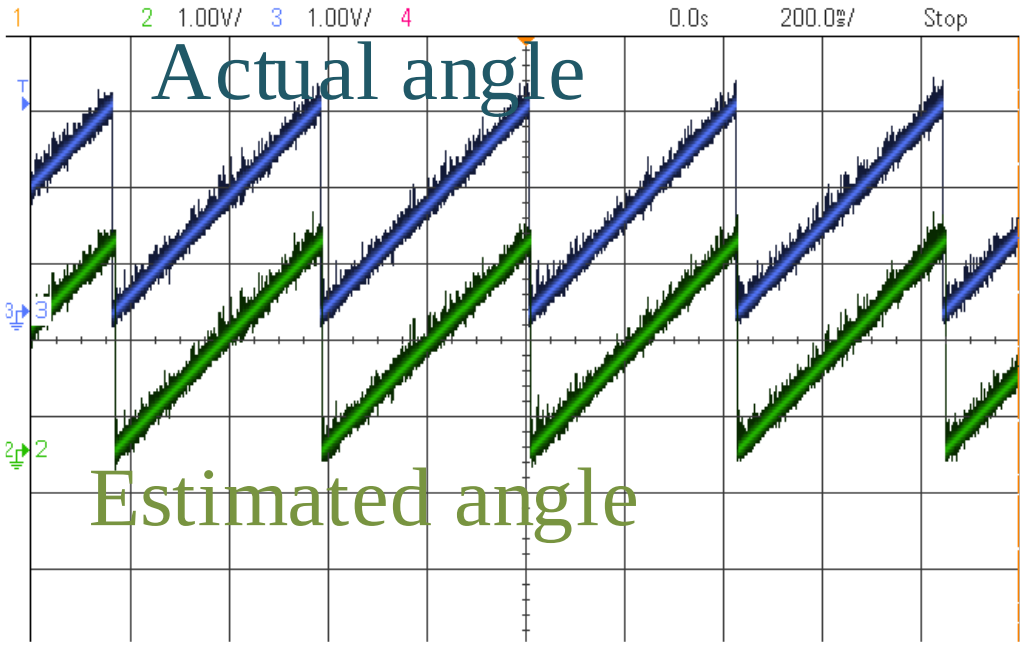

(a)

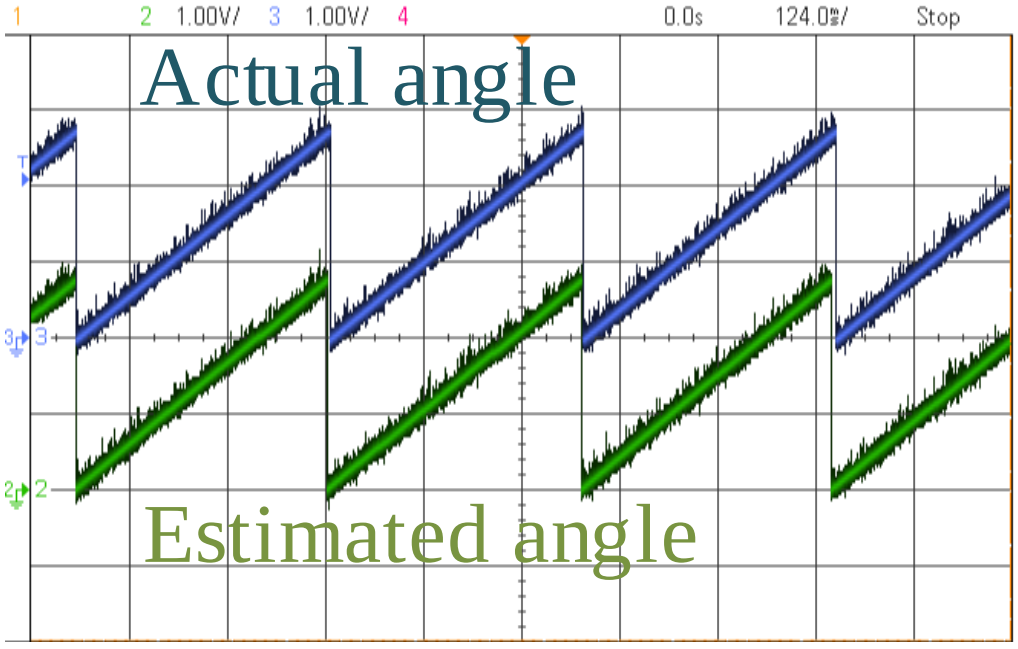

(b)

Fig. 3.11: Estimated and measured electrical rotor angle versus time at a) 75 rpm, and b) 100 rpm. The scale is 4.2 rad/div.

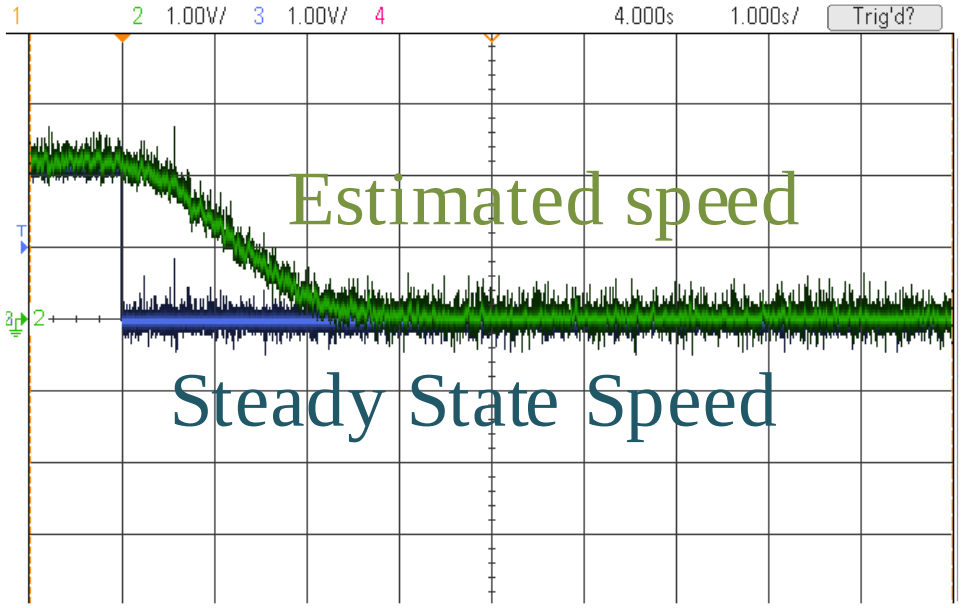

Fig. 3.12: Speed transient behavior when dropping the speed from 75 to 0 rpm.

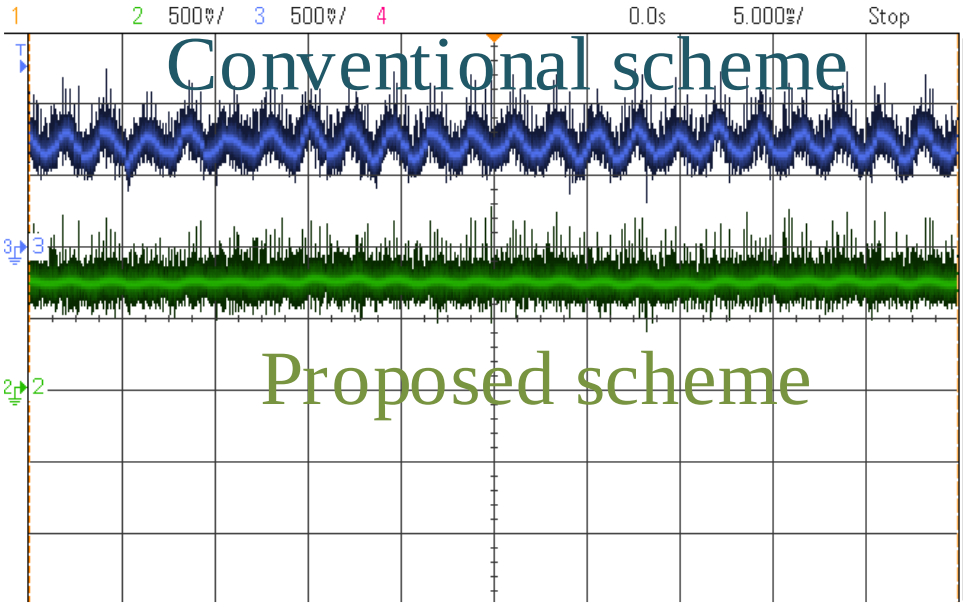

Fig. 3.13: $i_{\tilde{\theta}_r}$ in steady-state for conventional and proposed scheme. The scale is 0.25 A/div.

The angle estimated by the sensorless scheme is provided to the closed-loop control as the transformation angle. Therefore, any ripple in the angle estimation can give

rise to ripple in the current or speed. The harmonic spectrum of the sine of the estimated angle, which is used in the stationary-to-synchronous transformation matrix, is plotted and compared for both schemes in Fig. 3.14. The conventional scheme produces higher harmonic content, which means more oscillation in the rotor angle estimation, whereas the proposed scheme contains less distortion. The total harmonic distortion is 11.2% in Fig. 3.14(a) and 4.8% in Fig. 3.14(b). Odd harmonic orders up to 11 are dominant in the analysis.

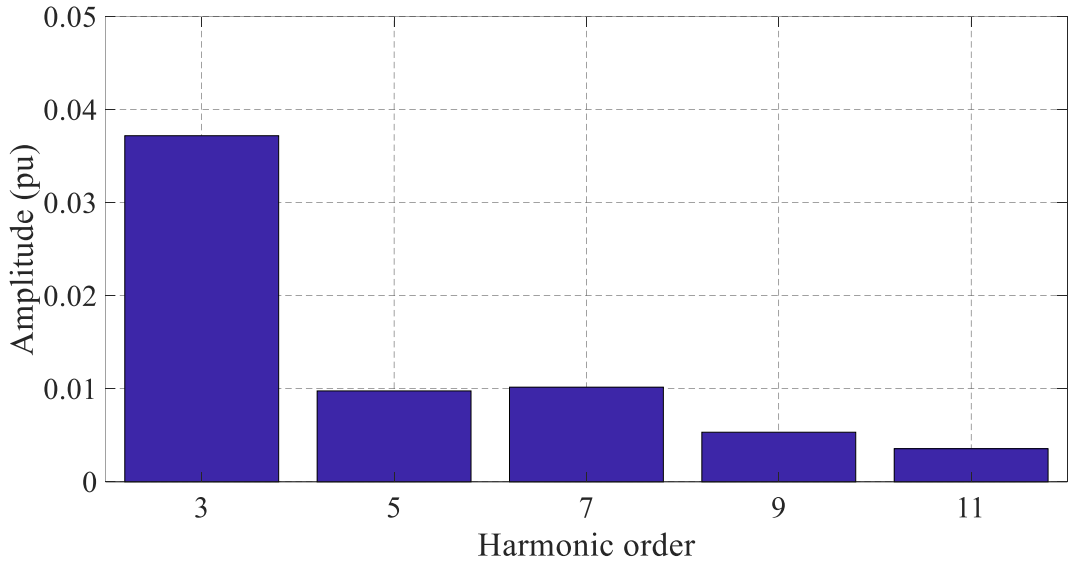

(a)

Fig. 3.14: Harmonic spectrum of $\sin\tilde{\theta}_r$, normalized with respect to the fundamental, for a) conventional scheme and b) proposed scheme.

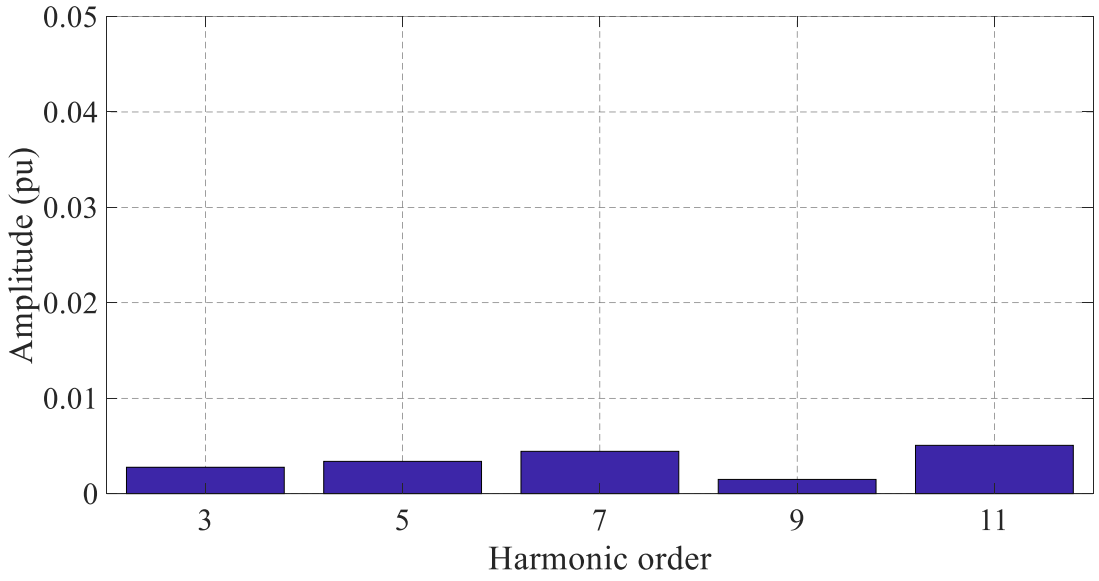

(b)

Fig. 3.14: Continued.

4. SUMMARY AND FUTURE WORK

In the first part of this dissertation, a method, called SEOE, has been proposed for enhancement of the efficiency in multiphase electric drives by taking into account both the converter and stator copper losses. It improves the efficiency at light load operation of the machine (either motor or generator) by adequately selecting the number of active converter legs as a function of the current magnitude. Given that the efficiency enhancement mainly occurs at light load, the proposal is especially suitable for applications in which this type of operation is frequent, such as electric vehicles and wind turbines. It is shown that the loss reduction is also significant in comparison with the approach, called SECE, in which only the converter losses are considered. The amount of energy saved by the SEOE, with respect to the conventional use of all phases, becomes more significant as the machine possesses a lower stator winding resistance and as the switching frequency increases. A 6-phase experimental prototype was built and the functionality of the proposed SEOE was verified, as well as the outcomes of the theoretical study. The maximum increase in efficiency by using the SEOE, compared to using all phases, is about 2.6%, which can result in a substantial energy saving in the long term. Nearly seamless transitions are ensured when swapping the number of phases in real time, by automatically adjusting the current references.

In the second part, an improved position sensorless scheme based on high-frequency sinusoidal voltage injection was proposed in this dissertation. The proposed scheme offers better performance characteristics compared to the existing conventional

scheme. This is mainly achieved by removing some of the LPFs of the latter, which are proved to be unnecessary. Both methods were implemented on an experimental setup with an SPMSM. It was concluded that the improved technique provides faster speed transient response compared to the conventional one, for identical parameters. The rotor angle estimation was also observed to be smoother in the proposed improved scheme, which can further enhance the closed-loop control of the SPMSM.

Generally, the position sensorless schemes based on high frequency injections cause extra torque ripple in the system due to the induced high frequency currents. Since the high frequency voltages are injected in the fundamental plane of the surface mount permanent magnet synchronous motors, it adds up to the torque ripples created by the major harmonics which are present in the system. On the other hand, multiphase motor drives and specifically six phase in this case provides other control planes (*xy* planes). Injection of extra high frequency currents through the secondary plane such that it cancels out the torque ripple created by the high frequency current injected for position estimation can be investigated to remove the additional torque ripples in the system.

The back-EMF and current vectors in the first and second planes of the sample SPMSM is shown in Fig. 4.1 (a) and (b). A parametrized analysis of the developed torque in both planes is performed below with the parameters defined in (4.1)-(4.5). It is assumed that the main high frequency current for position sensorless estimation is injected in the first plane. Therefore, two type of torque will be developed in the first plane. The first type is the fundamental torque which is desired and is the result of the interaction of fundamental current and back-EMF, (4.6).

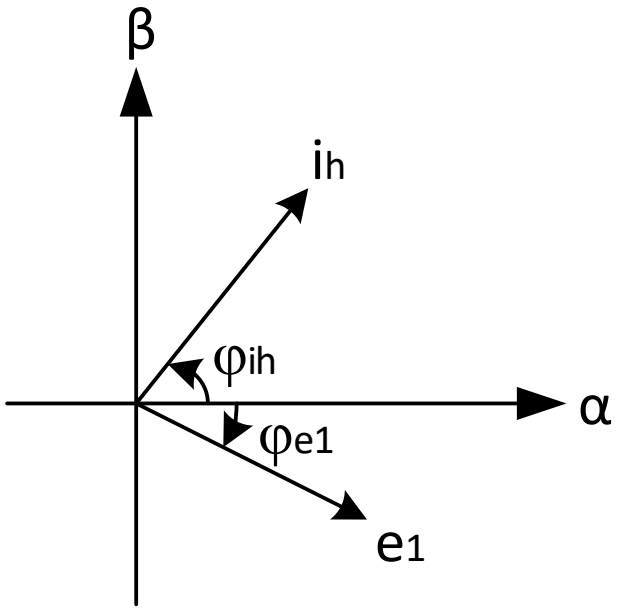

(a)

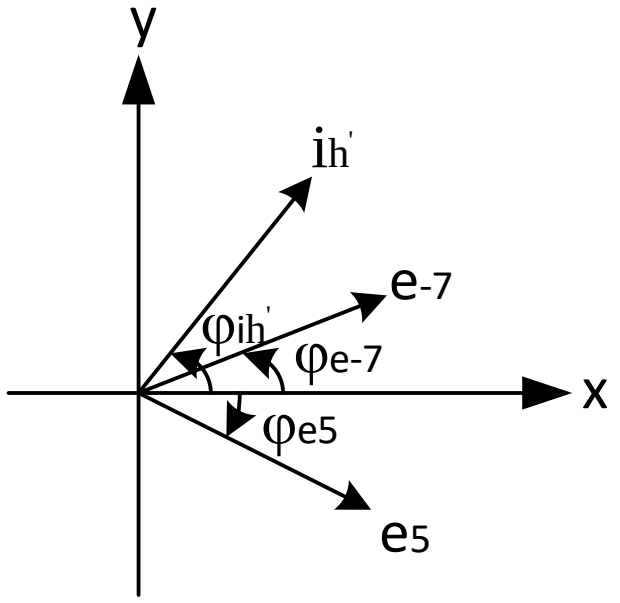

(b)

Fig. 4.1: Back-EMF and current vectors in first and second planes of the six phase SMPMSM.

$$e_1 = E_1\cos(\omega_1 t - \varphi_{e1}) \tag{4.1}$$

$$i_h = I_h\cos(\omega_h t + \varphi_{ih}) \tag{4.2}$$

$$e_5 = E_5\cos(\omega_5 t - \varphi_{e5}) \tag{4.3}$$

$$e_{-7} = E_{-7}\cos(\omega_{-7} t + \varphi_{e-7}) \tag{4.4}$$

$$i_{h'} = I_{h'}\cos(\omega_{h'} t + \varphi_{ih'}) \tag{4.5}$$

where e_1, i_h, e_5, e_{-7}, i_h', E_1, I_h, E_5, E_{-7}, I_h', ω_1, ω_h, ω_5, ω_{-7}, ω_h', t, φ_{e1}, φ_{ih}, φ_{e5}, φ_{e-7}, φ_{ih}' stand for fundamental frequency back-EMF, injected high frequency current in the first plane, forward fifth harmonic back-EMF, backward seventh harmonic back-EMF, injected high frequency current in the second plane, magnitude of the fundamental back-EMF, magnitude of the injected high frequency current in the first plane, magnitude of the forward fifth harmonic back-EMF, magnitude of the backward seventh harmonic back-EMF, magnitude of the injected high frequency current in the second plane, fundamental rotational speed, rotational speed of the injected high frequency current in the first plane, forward fifth harmonic rotational speed, backward seventh harmonic rotational speed, rotational speed of the injected high frequency current in the second plane, time, phase angle of the fundamental back-EMF, phase angle of the injected high frequency current in the first plane, phase angle of the forward fifth harmonic back-EMF, phase angle of the backward seventh harmonic back-EMF and the phase angle of the injected high frequency current in the second plane, respectively.

$$T_1 = e_1 i_1 = E_1 I_1\cos(\varphi_{e1} - \varphi_{i1}) \tag{4.6}$$

where T_1, i_1, I_1, φ_{i1} stand for fundamental torque, fundamental current in the first plane, magnitude of the fundamental current and the phase angle of the fundamental current, respectively.

The fundamental back-EMF is assumed as the reference for angle measurement and fundamental current being in phase with it for simplification. A high frequency torque is also developed in the first plane due to the interaction of the fundamental and high frequency components as described by (4.7).

$$T_{h1} = e_1 i_h = E_1 I_h \cos((\omega_1 - \omega_h)t + \varphi_{e1} - \varphi_{ih}) \tag{4.7}$$

where T_{h1} stands for the high frequency torque in the first plane.

On the other hand, the injected high frequency current in the second plane also interacts with the +5th and -7th harmonics as the dominant harmonics in this system which creates another high frequency component of the torque in the second plane:

$$T_{h2} = e_5 i_{h'} + e_7 i_{h'} = E_5 I_{h'} \cos((\omega_5 - \omega_{h'})t + \varphi_{e5} - \varphi_{ih'}) + E_7 I_{h'} \cos((\omega_{-7} - \omega_{h'})t + \varphi_{e-7} - \varphi_{ih'}) \tag{4.8}$$

Now, i_h' as a degree of freedom should be injected such that extra torque ripples cancel each other. For example, if:

$$-7\omega_1 - \omega_{h'} = \omega_1 - \omega_h \Rightarrow \omega_{h'} = -8\omega_1 + \omega_h \tag{4.9}$$

the required frequency of the injected signal in the second plane is obtained by (4.9). However, the first torque ripple term in (4.8) will create a new ripple as described below:

$$5\omega_1 - \omega_{h'} = 13\omega_1 - \omega_h \tag{4.10}$$

So another high frequency component should be injected to remove the created ripple in the second plane by (4.10).

The amplitude and phase angle values of the injected high frequency signals are also calculated accordingly as:

$$E_1 I_h = E_7 I_{h'} => I_{h'} = \frac{E_1 I_h}{E_7} \tag{4.11}$$

$$\varphi_{e1} - \varphi_{ih} = \varphi_{e-7} - \varphi_{ih'} + \pi => \varphi_{ih'} = \varphi_{e-7} - \varphi_{e1} + \varphi_{ih} + \pi \tag{4.12}$$

Obviously, accurate control schemes for the injected high frequency signals are required to properly adjust their amplitude and phase angles at the desired values.

REFERENCES

[1] F. Barrero and M. J. Duran, "Recent advances in the design, modeling, and control of multiphase machines—Part I," *IEEE Trans. Ind. Electron.*, vol. 63, no. 1, pp. 449-458, Jan. 2016.

[2] M. J. Duran and F. Barrero, "Recent advances in the design, modeling, and control of multiphase machines—Part II," *IEEE Trans. Ind. Electron.*, vol. 63, no. 1, pp. 459-468, Jan. 2016.

[3] E. Levi, R. Bojoi, F. Profumo, H. A. Toliyat and S. Williamson, "Multiphase induction motor drives - a technology status review," in *IET Electric Power Applications*, vol. 1, no. 4, pp. 489-516, July 2007.

[4] I. Subotic, N. Bodo, E. Levi and M. Jones, "Onboard integrated battery charger for EVs using an asymmetrical nine-phase machine," *IEEE Trans. Ind. Electron.*, vol. 62, no. 5, pp. 3285-3295, May 2015.

[5] N. Bodo, E. Levi, I. Subotic, J. Espina, L. Empringham and C. M. Johnson, "Efficiency evaluation of fully integrated on-board EV battery chargers with nine-phase machines," *IEEE Trans. Energy Convers*., vol. 32, no. 1, pp. 257266, Mar. 2017.

[6] I. Subotic, N. Bodo and E. Levi, "Integration of six-phase EV drivetrains into battery charging process with direct grid connection," *IEEE Trans. Energy Convers.*, vol. 32, no. 3, pp. 1012-1022, Sep. 2017.

[7] X. Chen, J. Wang, V. I. Patel and P. Lazari, "A nine-phase 18-slot 14-pole interior permanent magnet machine with low space harmonics for electric vehicle applications," *IEEE Trans. Energy Convers.*, vol. 31, no. 3, pp. 860-871, Sep. 2016.

[8] V. I. Patel, J. Wang, D. T. Nugraha, R. Vuletic and J. Tousen"Enhanced availability of drivetrain through novel multiphase permanent-magnet machine drive," *IEEE Trans. Ind. Electron.*, vol. 63, no. 1, pp. 469-480, Jan. 2016.

[9] B. P. Reddy, M. R. A, M. Sahoo and S. Keerthipati, "A fault tolerant multilevel inverter for improving the performance of pole-phase modulated nine-phase induction motor drive," *IEEE Trans. Ind. Electron.*, vol. 65, no. 2, pp. 1107-1116, Feb. 2017.

[10] B. S. Umesh and K. Sivakumar, "Pole-phase modulated multiphase induction motor drive with reduced torque ripple and improved DC link utilization," *IEEE Trans. Power Electron.*, vol. 32, no. 10, pp. 7862-7869, Oct. 2017.

[11] E. Levi, "Advances in converter control and innovative exploitation of additional degrees of freedom for multiphase machines," *IEEE Trans. Ind. Electron.*, vol. 63, no. 1, pp. 433-448, Jan. 2016.

[12] http://www.danskelbilkomite.dk/pml_mini.pdf

[13] J. Birk and B. Andresen, "Parallel-connected converters for optimizing efficiency, reliability and grid harmonics in a wind turbine," in Proc. EPE, 2007, pp. 1-8.

[14] J. Wang, R. Qu and Y. Liu, "Comparison study of superconducting generators with multiphase armature windings for large-scale direct-drive wind turbines," *IEEE Trans. Applied Supercond.*, vol. 23, no. 3, pp. 5201005-5201005, Jun. 2013.

[15] M. J. Duran, I. Gonzalez-Prieto, A. Gonzalez-Prieto and F. Barrero, "Multiphase energy conversion systems connected to microgrids with unequal power sharing capability," *IEEE Trans. Energy Convers.*, vol. 32, no. 4, pp. 1386-1395, Dec. 2017.

[16] V. Yaramasu, B. Wu, P. C. Sen, S. Kouro and M. Narimani, "High-power wind energy conversion systems: State-of-the-art and emerging technologies," *Proc. IEEE*, vol. 103, no. 5, pp. 740-788, May 2015.

[17] H. S. Che, E. Levi, M. Jones, M. J. Duran, W. P. Hew and N. A. Rahim, "Operation of a six-phase induction machine using series-connected machine-side converters," *IEEE Trans. Ind. Electron.*, vol. 61, no. 1, pp. 164-176, Jan. 2014.

[18] E. Prieto-Araujo, A. Junyent-Ferré, D. Lavènia-Ferrer and O. Gomis-Bellmunt, "Decentralized control of a nine-phase permanent magnet generator for offshore wind turbines," *IEEE Trans. Energy Convers.*, vol. 30, no. 3, pp. 1103-1112, Sep. 2015.

[19] Yongbing, Z. Hongtao, L. Ying, F. Luguang and Y. Xu, "Modelling and control of a multi-phase permanent magnet synchronous generator and efficient hybrid 3L-converters for large direct-drive wind turbines," in *IET Electric Power Applications*, vol. 6, no. 6, pp. 322-331, July 2012.

[20] A. S. Nanoty and A. R. Chudasama, "Design of multiphase induction motor for electric ship propulsion," *2011 IEEE Electric Ship Technologies Symposium*, Alexandria, VA, 2011, pp. 283-287.

[21] R. Bojoi, A. Cavagnino, A. Tenconi and S. Vaschetto, "Multiphase PM machine for More Electric Aircraft applications: Prototype for design validation," *IECON 2012 - 38th Annual Conference on IEEE Industrial Electronics Society*, Montreal, QC, 2012, pp. 3628-3634.

[22] I. Zoric, M. Jones and E. Levi, "Arbitrary power sharing among three-phase winding sets of multiphase machines," *IEEE Trans. Ind. Electron.*, vol. 65, no. 2, pp. 1128-1139, Feb. 2018.

[23] I. González-Prieto, M. J. Duran and F. J. Barrero, "Fault-tolerant control of six-phase induction motor drives with variable current injection," *IEEE Trans. Power Electron.*, vol. 32, no. 10, pp. 7894-7903, Oct. 2017.

[24] A. G. Yepes *et al*., "Selection Criteria of Multiphase Induction Machines for Speed-Sensorless Drives Based on Rotor Slot Harmonics," in *IEEE Transactions on Industrial Electronics*, vol. 63, no. 8, pp. 4663-4673, Aug. 2016.

[25] F. Baneira, J. Doval-Gandoy, A. G. Yepes, Ó. López and D. Pérez- Estévez, "Control strategy for multiphase drives with minimum losses in the full torque operation range under single open-phase fault," *IEEE Trans. Power Electron.* vol. 32, no. 8, pp. 6275-6285, Aug. 2017.

[26] Y. Wu, M. A. Shafi, A. M. Knight and R. A. McMahon, "Comparison of the effects of continuous and discontinuous PWM schemes on power losses of voltage-sourced inverters for induction motor drives," *IEEE Trans. Power Electron.*, vol. 26, no. 1, pp. 182-191, Jan. 2011.

[27] M. Quraan, P. Tricoli, S. D'Arco and L. Piegari, "Efficiency assessment of modular multilevel converters for battery electric vehicles," *IEEE Trans. Power Electron.*, vol. 32, no. 3, pp. 2041-2051, Mar. 2017.

[28] F. L. Mapelli, D. Tarsitano and M. Mauri, "Plug-in hybrid electric vehicle: modeling, prototype realization, and inverter losses reduction analysis," *IEEE Trans. Ind. Electron*., vol. 57, no. 2, pp. 598-607, Feb. 2010.

[29] J. S. Lai, W. Yu, P. Sun, S. Leslie, B. Arnet, C. Smith, A. Cogan, "A hybrid-switch-based soft-switching inverter for ultrahigh-efficiency traction motor drives," *IEEE Trans. Ind. Appl.*, vol. 50, no. 3, pp. 1966-1973, May-June 2014.

[30] A. Merkert, T. Krone and A. Mertens, "Characterization and scalable modeling of power semiconductors for optimized design of traction inverters with SiC-devices," *IEEE Trans. Power Electron*., vol. 29, no. 5, pp. 2238-2245, May 2014.

[31] A. Wintrich, U. Nicolai, W. Tursky, and T. Reimann, "Application manual power semiconductors. Semikron international GmbH," 2015.

[32] E. Jung, H. Yoo, S. K. Sul, H. S. Choi and Y. Y. Choi, "A nine-phase permanent-magnet motor drive system for an ultrahigh-speed elevator," *IEEE Trans. Ind. Appl*., vol. 48, no. 3, pp. 987-995, May./Jun. 2012.

[33] A. Tessarolo and C. Bassi, "Stator harmonic currents in VSI-fed synchronous motors with multiple three-phase armature windings," *IEEE Trans. Energy Convers*., vol. 25, no. 4, pp. 974-982, Dec. 2010.

[34] M. Barcaro, M. Morandin, T. Pradella, N. Bianchi and I. Furlan, "Iron Saturation Impact on High-Frequency Sensorless Control of Synchronous Permanent-Magnet Motor," *IEEE Trans. Ind. Appl.*, vol. 53, no. 6, pp. 5470-5478, Nov.-Dec. 2017.

[35] F. Mendoza-Mondragón, V. M. Hernández-Guzmán and J. Rodríguez-Reséndiz, "Robust Speed Control of Permanent Magnet Synchronous Motors Using Two-Degrees-of-Freedom Control," *IEEE Trans. Ind. Electron.*, vol. 65, no. 8, pp. 6099-6108, Aug. 2018.

[36] L. Zhou, W. Gruber and D. L. Trumper, "Position Control for Hysteresis Motors: Transient-time Model and Field-oriented Control," *IEEE Trans. on Ind. Appl.*.

[37] M. Roetzer, U. Vollmer and R. M. Kennel, "Demodulation Approach for Slowly Sampled Sensorless Field-Oriented Control Systems Enabling Multiple-Frequency Injections," *IEEE Trans. on Ind. Appl.*, vol. 54, no. 1, pp. 732-744, Jan.-Feb. 2018.

[38] P. Pieters and J. Riikonen, "Reliability of Adjustable Speed Drives," *IEEE Ind. Appl. Mag.*, vol. 16, no. 6, pp. 47-55, Nov.-Dec. 2010.

[39] S. C. Yang and G. R. Chen, "High-Speed Position-Sensorless Drive of Permanent-Magnet Machine Using Discrete-Time EMF Estimation," *IEEE Trans. on Ind. Electron.*, vol. 64, no. 6, pp. 4444-4453, Jun. 2017.

[40] X. Song, J. Fang, B. Han and S. Zheng, "Adaptive Compensation Method for High-Speed Surface PMSM Sensorless Drives of EMF-Based Position Estimation Error," *IEEE Trans. on Power Electron.*, vol. 31, no. 2, pp. 1438-1449, Feb. 2016.

[41] G. Wang, H. Zhan, G. Zhang, X. Gui and D. Xu, "Adaptive Compensation Method of Position Estimation Harmonic Error for EMF-Based Observer in Sensorless IPMSM Drives," *IEEE Trans. on Power Electron.*, vol. 29, no. 6, pp. 3055-3064, Jun. 2014.

[42] X. Song, B. Han, S. Zheng and J. Fang, "High-Precision Sensorless Drive for High-Speed BLDC Motors Based on the Virtual Third Harmonic Back-EMF," *IEEE Trans. on Power Electron.*, vol. 33, no. 2, pp. 1528-1540, Feb. 2018.

[43] H. Zhan, Z. Q. Zhu and M. Odavic, "Nonparametric Sensorless Drive Method for Open-Winding PMSM Based on Zero-Sequence Back EMF With Circulating Current Suppression," *IEEE Trans. on Power Electron.*, vol. 32, no. 5, pp. 3808-3817, May. 2017.

[44] G. Zhang, G. Wang and D. Xu, "Saliency-based position sensorless control methods for PMSM drives - A review," *Chinese Journal of Electrical Engineering*, vol. 3, no. 2, pp. 14-23, Sep. 2017.

[45] Y. Kano and N. Matsui, "Rotor Geometry Design of Saliency-Based Sensorless Controlled Distributed-Winding IPMSM for Hybrid Electric Vehicles," *IEEE Trans. on Ind. Appl.*, accepted for publication.

[46] J. H. Im and R. Y. Kim, "Improved Saliency-Based Position Sensorless Control of Interior Permanent-Magnet Synchronous Machines With Single DC-Link Current Sensor Using Current Prediction Method," *IEEE Trans. Ind. Electron.*, vol. 65, no. 7, pp. 5335-5343, Jul. 2018.

[47] Y. Zhou, D. Zhang, X. Chen and Q. Lin, "Sensorless Direct Torque Control for Saliency Permanent Magnet Brushless DC Motors," *IEEE Trans. Energy Convers.*, vol. 31, no. 2, pp. 446-454, Jun. 2016.

[48] Z. Chen, F. Wang, G. Luo, Z. Zhang and R. Kennel, "Secondary Saliency Tracking-Based Sensorless Control for Concentrated Winding SPMSM," *IEEE Trans. Ind. Informat.*, vol. 12, no. 1, pp. 201-210, Feb. 2016.

[49] M. S. Lim, S. H. Chai and J. P. Hong, "Design of Saliency-Based Sensorless-Controlled IPMSM With Concentrated Winding for EV Traction," *IEEE Trans. Magn.*, vol. 52, no. 3, pp. 1-4, Mar. 2016.

[50] A. Srivorakul and S. Suwankawin, "A Synchro-Perspective-Based High-Frequency Voltage Injection Method for Position-Sensorless Vector Control of Doubly-Fed Induction Machines," *IEEE Trans. Ind. Appl.*, accepted for publication.

[51] H. Zhang, W. Liu, Z. Chen, G. Luo, J. Liu and D. Zhao, "Asymmetric Space Vector Modulation for PMSM Sensorless Drives Based on Square-Wave Voltage-Injection Method," *IEEE Trans. Ind. Appl.*, vol. 54, no. 2, pp. 1425-1436, Mar.-Apr. 2018.

[52] G. Wang, J. Kuang, N. Zhao, G. Zhang and D. Xu, "Rotor Position Estimation of PMSM in Low Speed Region and Standstill Using Zero Voltage Vector Injection," *IEEE Trans. Power Electron.*, accepted for publication.

[53] G. Wang, D. Xiao, N. Zhao, X. Zhang, W. Wang and D. Xu, "Low-Frequency Pulse Voltage Injection Scheme-Based Sensorless Control of IPMSM Drives for Audible Noise Reduction," *IEEE Trans. Ind. Electron.*, vol. 64, no. 11, pp. 8415-8426, Nov. 2017.

[54] S. C. Yang, S. M. Yang and J. Hui Hu, "Design Consideration on the Square-Wave Voltage Injection for Sensorless Drive of Interior Permanent-Magnet Machines," *IEEE Trans. Ind. Electron.*, vol. 64, no. 1, pp. 159-168, Jan. 2017.

[55] A. Yousefi-Talouki, P. Pescetto, G. Pellegrino and I. Boldea, "Combined Active Flux and High-Frequency Injection Methods for Sensorless Direct-Flux Vector Control of Synchronous Reluctance Machines," *IEEE Trans. Power Electron.*, vol. 33, no. 3, pp. 2447-2457, Mar. 2018.

[56] S. C. Yang and Y. L. Hsu, "Full Speed Region Sensorless Drive of Permanent-Magnet Machine Combining Saliency-Based and Back-EMF-Based Drive," *IEEE Trans. Ind. Electron.*, vol. 64, no. 2, pp. 1092-1101, Feb. 2017.

[57] J. H. Jang, S. K. Sul, J. I. Ha, K. Ide and M. Sawamura, "Sensorless drive of surface-mounted permanent-magnet motor by high-frequency signal injection based on magnetic saliency," *IEEE Trans. Ind. Appl.*, vol. 39, no. 4, pp. 1031-1039, Jul.-Aug. 2003.

[58] D. Kim, Y. C. Kwon, S. K. Sul, J. H. Kim and R. S. Yu, "Suppression of Injection Voltage Disturbance for High-Frequency Square-Wave Injection Sensorless Drive With Regulation of Induced High-Frequency Current Ripple," *IEEE Trans. Ind. Appl.*, vol. 52, no. 1, pp. 302-312, Jan.-Feb. 2016.

[59] Y. D. Yoon, S. K. Sul, S. Morimoto and K. Ide, "High-Bandwidth Sensorless Algorithm for AC Machines Based on Square-Wave-Type Voltage Injection," *IEEE Trans. on Ind. Appl.*, vol. 47, no. 3, pp. 1361-1370, May.-Jun. 2011.

[60] A. Mahmoudi, S. Kahourzade, N. A. Rahim, H. W. Ping and M. N. Uddin, "Design and prototyping of an optimised axial-flux permanent-magnet synchronous machine," *IET Electr. Power Appl.*, vol. 7, no. 5, pp. 338-349, May. 2013.

[61] F. B. Grigoletto and H. Pinheiro, "Flexible arrangement of static converters for grid-connected wind energy conversion systems," *IEEE Trans. Ind. Electron*., vol. 61, no. 9, pp. 4707-4721, Sep. 2014.

[62] B. Andresen and J. Birk, "A high power density converter system for the Gamesa G10x 4,5 MW wind turbine," in Proc. EPE, 2007, pp. 1-8.

[63] F. Baneira, J. Doval-Gandoy, A. G. Yepes, Ó. López and D. Pérez-Estévez, "Comparison of postfault strategies for current reference generation for dual three-phase machines in terms of converter losses," *IEEE Trans. Power Electron.*, vol. 32, no. 11, pp. 8243-8246, Nov. 2017.

[64] F. C. de Andrade, F. Bradaschia, L. R. Limongi and M. C. Cavalcanti, "A reduced switching loss technique based on generalized scalar PWM for nine-switch inverters," *IEEE Trans. Ind. Electron.*, vol. 65, no. 1, pp. 38-48, Jan. 2018.

[65] H. S. Che, M. J. Duran, E. Levi, M. Jones, W. P. Hew and N. A. Rahim, "Postfault operation of an asymmetrical six-phase induction machine with single and two isolated neutral points," *IEEE Trans. Power Electron.*, vol. 29, no. 10, pp. 5406-5416, Oct. 2014.

[66] G. Pellegrino, A. Vagati, B. Boazzo and P. Guglielmi, "Comparison of induction and PM synchronous motor drives for EV application including design examples," *IEEE Trans. on Ind. Appl.*, vol. 48, no. 6, pp. 2322-2332, Nov.-Dec. 2012.

[67] R. E. Araújo, R. de Castro, C. Pinto, P. Melo and D. Freitas, "Combined sizing and energy management in EVs with batteries and supercapacitors," *IEEE Trans. Veh. Technol.*, vol. 63, no. 7, pp. 3062-3076, Sep. 2014.

[68] D. N. Zmood and D. G. Holmes, "Stationary frame current regulation of PWM inverters with zero steady-state error," *IEEE Trans. Power Electron.*, vol. 18, no. 3, pp. 814-822, May 2003.

[69] E. Levi, "Multiphase electric machines for variable-speed applications," *IEEE Trans. Ind. Electron.*, vol. 55, no. 5, pp. 1893-1909, May 2008.

[70] A. Negahdari, A. G. Yepes, J. Doval-Gandoy and H. Toliyat, "Efficiency Enhancement of Multiphase Electric Drives at Light-Load Operation Considering Both Converter and Stator Copper Losses," in *IEEE Transactions on Power Electronics*.

[71] L. Harnefors, S. E. Saarakkala and M. Hinkkanen, "Speed Control of Electrical Drives Using Classical Control Methods," in *IEEE Transactions on Industry Applications*, vol. 49, no. 2, pp. 889-898, March-April 2013.

[72] A. G. Yepes, A. Vidal, J. Malvar, O. López and J. Doval-Gandoy, "Tuning Method Aimed at Optimized Settling Time and Overshoot for Synchronous Proportional-Integral Current Control in Electric Machines," in *IEEE Transactions on Power Electronics*, vol. 29, no. 6, pp. 3041-3054, June 2014.

[73] E. Levi, D. Dujic, M. Jones and G. Grandi, "Analytical Determination of DC-Bus Utilization Limits in Multiphase VSI Supplied AC Drives," in *IEEE Transactions on Energy Conversion*, vol. 23, no. 2, pp. 433-443, June 2008.

[74] https://www.google.com/search?q=electric+vehicle&source=Inms&tbm=isch&sa==X&ved=0ahUKEwiqkTmpPzdAhUMEqwKHQO2C2cQ_AUIECgD&biw=1920&bih=969.

[75] https://www.google.com/search?biw=1920&bih=969&tbm=isch&sa=1&ei=Dyu-W9SrCcfesAWNvoPoCg&q=wind+farm&oq=wind+farm&gs_l=img.3..0l10.78164.80705..81498...0.0..0.63.396.9.....1....1..gws-wiz-img.....0i67.2mRo07f18hw.

[76] https://www.google.com/search?biw=1920&bih=969&tbm=isch&sa=1&ei=YSu-WiMJ8bAtQW2xLAo&q=all+electric+ships&oq=all+electric+ships&gs_l=img.3..0i24.18374.22658..22930...0.0..0.59.727.18.....1....1..gws-wiz-img..... 0j0i67j0i8i30.85xZru0FB8Y.

[77] https://www.google.com/search?biw=1920&bih=969&tbm=isch&sa=1&ei=eSu-W-bHFImAtgXpr6fABQ&q=more+electric+aircraft&oq=more+electric+&gs_l=img.3.0.0j0i24l9.165246.167650..169579...0.0..0.60.604.14.....1....1..gws-wiz- img.....0i67j0i8i30j0i30.ii1aMhk_e84.